2015년 8월

박사학위 논문

Quantitative Analysis of Three-dimensional Morphology and Biophysical Cell Parameters of Live Cells using Digital Holographic Imaging

조선대학교 대학원

컴 퓨 터 공 학 과

역 발 류

Quantitative Analysis of Three-dimensional Morphology and Biophysical Cell Parameters of Live Cells using Digital Holographic Imaging

디지털 홀로그래픽 영상 기반 생물세포 3차원 모폴러지 및 생물리학적 셀파라미터의 정량적 분석방법에 관한 연구

2015년 8월 25일

조선대학교 대학원

컴 퓨 터 공 학 과

역 발 류

Quantitative Analysis of Three-dimensional Morphology and Biophysical Cell Parameters of Live Cells using Digital Holographic Imaging

지도교수 문 인 규

이 논문을 공학 박사학위신청 논문으로 제출함

2015년 4월

조선대학교 대학원

컴 퓨 터 공 학 과

역 발 류

역발류의 박사학위논문을 인준함

위 원 장	조선대학교	교 수	정 일 용(인)
위 원	조선대학교	교 수	이 상 웅(인)
위 원	조선대학교	교 수	권 구 락(인)
위 원	한경대학교	교 수	조 명 진(인)
위 원	조선대학교	교 수	문 인 규(인)

2015년 6월

조선대학교 대학원

CONTENTS

LIST OF FIGURES

LIST OF TABLES

ABSTRACT

Quantitative Analysis of Three-dimensional Morphology and Biophysical Cell Parameters of Live Cells using Digital Holographic Imaging

Faliu Yi
Advisor : Prof. Inkyu Moon, Ph.D.
Department of Computer Engineering
Graduate School of Chosun University

For semitransparent or transparent biological cells, the intensity based two-dimensional (2D) imaging system suffers from losses of a large amount of quantitative detailed information about cell structure and content. 2D imaging method also results in low-contrast image. On the contrary, three-dimensional imaging (3D) technique such as digital holography comes to the forefront as promising tools for 3D biological cells visualization, pattern recognition and study of their dynamics as it can provide rich 3D information, such as the surface morphological and optical thickness data of these microscopic objects. Among a large number of developed 3D imaging platforms, digital holographic microscopy (DHM) as a promising 3D imaging system has widely viewed in life sciences, medical diagnoses, and medicine due to its advantages in terms of easy configuration and fast imaging, low-cost and non-destruction to microorganisms.

In this dissertation, The automated analysis of 3D cells that are obtained by DHM is focused. Totally, two different kinds of transparent cells, which are

red blood cells (RBCs) and cardiomyocytes, are three-dimensionally imaged and quantitatively analyzed. Both RBCs and cardiomyocytes phase images are numerically reconstructed from holograms recorded by DHM. RBCs has been extensively studied in bio-medical fields due to its important functionality in delivering oxygen from lungs to body tissues and transporting carbon dioxide from the tissues to the lungs. The resulted characteristic properties of 3D RBCs from DHM are beneficial to characterize cell storage lesions, recognize unnormal RBCs, and evaluate drug testing. On the other hand, cardiomyocytes or myocardial cells, which are the main contractile elements of the heart muscle, generate human heart beating and control blood flow through the blood vessels of the circulatory system. The automated analysis of 3D cardiomyocytes are crucial to improve the predictability of compound toxicity through safety profiling assays during the lengthy drug discovery process in order that potentially toxic compounds are detected early in the process before significant time and important financial investments are made. Experimental results are presented that demonstrate the feasibility of the automated analysis procedure for both 3D RBCs and cardiomyocytes.

초 록

디지털 홀로그래픽 영상 기반 생물세포 3차원 모폴러지 및 생물리학적 셀파라미터의 정량적 분석방법에 관한 연구

Faliu Yi
Advisor : Prof. Inkyu Moon, Ph.D.
Department of Computer Engineering
Graduate School of Chosun University

2D 이미징 시스템 기반에 집중된 반투명 또는 투명 생물학적 세포는 세포 구조와 내용에 대한 상세한 정량적 정보가 대량 손실된다.2D 이미징 기술은 저채도 이미지에서 동일한 결과를 보인다. 반대로, 디지털 홀로그램과 같은 3차원 이미징 기술은 3D 생물학적 세포 시각화, 표면 형태와 세포의 광학적 두께와 같은 풍부한 3D정보를 제공함으로써 패턴 인식과 그 동적 연구 분야를 위한 선두 기술로써 각광을 받고 있다.개발된 3D 이미징 기술 중, 촉망되는 3D 이미징 시스템으로써 DHM에 기반한 3D 이미징 플랫폼은 쉬운 구조와 빠른 이미징 처리, 저비용 그리고 미생물 비파괴 측면의 이점으로 인하여 생명과학, 의료진단 그리고 의학에서 광범위하게 보여진다.

본 논문에서는 DHM에 의해 획득한 3D 셀의 자동 분석에 중점을 둔다. 전적으로, 적혈구와 심장근육세포와 같은 두 가지 다른 종류의 투명 세포는 3차원적 영상화와 정량 분석을 하였다. 적혈구와 심장근육세포 위상 이미지는 DHM에 의해 기록된 홀로그램으로부터 절대적으로 재구성된다.적혈구는 폐에서 신체 조직으로 산소를 전달 및 조직에서 폐로 이산화탄소를 보내는 것에서 중요한 기능을 하기 때문에 바이오 메디컬 분야에서 광범위하게 연구되어지고 있다. DHM에서 생성된 3D 적혈구의 특유 성질은 세포 병변 특성, 비정상 적혈구 인식 그리고 약물 테스트에 유

익하다. 한편, 심장근육 수축의 주요소인 심장근육세포나 심근세포는 일반적인 사람의 심장 박동과 순환계의 혈관을 통해 혈액 흐름을 제어할 수 있다. 자동 분석된 3D 심장근육세포는 잠재적인 독성 화합물이 긴 시간과 투자비용으로 만들어지기 전에 프로세서 초기에 감지되어지는 순서로 오랜 신약 개발 과정동안 안전적인 프로파일 링 분석을 통하여 화합물 독성의 예측을 향상시키기 위해 매우 중요하다. 본 실험 결과는 3D 적혈구와 심장근육세포 모두에 자동화된 분석 과정의 실행성을 증명하여 보여준다.

1. Introduction

For semitransparent or transparent biological targets, the intensity based two-dimensional (2D) imaging system suffers from losses of a large amount of quantitative detailed information about cell structure and content. 2D imaging method also results in low-contrast image [1-4]. Even though some advanced 2D imaging systems, such as quantitative phase contrast and differential interference contrast microscopes [3-6], have the feature to quantitatively investigate the biological microorganisms to some extent, they cannot provide optical thickness information about the imaging biological cells, which in turn make the analysis of microscopic object limited. 2D imaging microscopic system has fundamental limitations on quantifying information about 3D morphology, dry mass production, and density of the biological cells. Moreover, it is difficult to dynamically visualize the character of variations in morphology of semitransparent or transparent microorganisms because they seen to be the same under 2D imaging microscopic systems [7].

The three-dimensional (3D) holographic imaging system has been studied for visualization, identification, and tracking of biological micro/nano- organisms [8-20]. In the areas of biomedical imaging, defense, medical diagnosis, medical therapeutics, and security, the 3-D holographic imaging system has a lot of potential [8-26]. Consequently, 3D digital image processing, which can directly affect future research on the microscopic objects under study, becomes more and more important because it becomes easier and more convenient to obtain the computational 3D image of the microorganisms with the development of the 3D optical holographic imaging system. Without limitations existed in 2D image system, the holographic images reconstructed numerically from a hologram obtained by 3D digital holography-based imaging systems can provide rich 3D information, such as the surface morphological and optical thickness data of the microorganism targets, which make it possible for the 3D measurement of

microscopic objects. Among varied number of 3D imaging techniques, digital holographic microscopy (DHM) as one of the promising 3D imaging methods has been widely researched for observation, metrology, and tracking of biological micro/nano-organism as it is a low-cost and non-invasive, fast imaging and easy configured approach [27-32]. Compared with classical optical microscopy, DHM provides a major advantage in overcoming the classical depth of field limitation. DHM is also a quantitative phase imaging technique which directly and non-invasively provides the optical thickness of biological cells in live and dynamic conditions which other 3D imaging techniques such as the electron microscopy are destructive to the imaging cells. Since DHM is not destructive for specimens, they can be investigated once more by any other optical imaging systems.

In this dissertation, the automated analysis of 3D cells that are obtained by DHM is focused. Totally, two different kinds of transparent cells, which are red blood cells (RBCs) and cardiomyocytes, are three-dimensionally imaged and quantitatively analyzed. Both RBCs and cardiomyocytes quantitative phase images are numerically reconstructed from holograms recorded by DHM. As essential ingredients of human being, the automated analysis of both 3D RBCs and cardiomyocytes are helpful to the investigation of RBC-related and cardiomyocyte-related diseases [7]. Moreover, the characteristic properties of these 3D cells can be used to screen the compounds during drug testing.

RBCs are essential ingredients of bloodstream in human being. They cannot only deliver oxygen to body tissues via the blood flowing through the circulatory system in vertebrate organisms, but also absorb oxygen in the lungs and release it when squeezing through the body's capillaries [33-34]. Normally, a relatively stable number of RBCs is maintained in the circulatory system and it is necessary to stimulate RBCs production with medications for patients suffering from anemia. Recent studies show that there are numerous biochemical, structural, inflammatory, and physiologic changes in stored red cells, referred to as red cell storage lesion, which to some extent impacts the

clinical outcome in transfused patients [35]. Therefore, the analysis of some quantitative cell parameters provided by DHM, including 3D morphology, mean corpuscular volume, and hemoglobin content at different storage periods will be helpful to characterize red cell storage lesions [36]. Moreover, it is estimated that the composition of RBCs types in human blood would be different for varied RBC-related diseases. The disordered change of 3D RBC in morphology shape can affect other body tissues indirectly. As a result, it is extremely important to have a classificaton algorithm that can categorize different types of RBCs effectively and efficiently in order to overcome the shortage of the traditional method that is time-consuming and labor-intensive [4]. In addition, counting cell types in the blood is an important task for evaluating clinical status. However, the RBCs extraction which refers to as RBCs segmentation has to be conducted first in order to measure the characteristic properties of each RBC. RBCs segmentation also benefit to the further RBCs analysis such as RBC recognition and tracking. In this dissertation, three directions are done in terms of automated 3D RBCs analysis after the RBCs phase images are numerically reconstructed from holograms that are recorded with DHM system. The fundamental and the most important one is the RBCs segmentation [37]. The results of RBCs segmentation can directly affect the following study of RBCs. A good RBCs extraction method should at least results in low over-segmentation and under-segmentation. The second research direction about 3D RBCs is the quantitative analysis of RBCs stored in different periods. These results would reveal the relationship between the RBC characteristic properties and their aging. This analysis will also be beneficial to the understanding of the features of RBCs with different storage periods and evaluation of any modifications in the 3D cell morphology and hemoglobin content induced by the length of storage time. The third research direction about 3D RBCs is the automated counting of morphologically normal RBCs. This will be helpful to measure the percentage of typical normal shapes of RBCs in a reconstructed RBC phase image that consists of multiple RBCs for disease diagnosis and drug

testing.

Cardiomyocytes or myocardial cells [38], which are the main contractile elements of the heart muscle, generate human heart beating and control blood flow through the blood vessels of the circulatory system. Like many other types of biological cells, cardiomyocytes are mostly transparent.The optical imaging systems used to capture cardiomyocytes images previously reproted include fluorescence microscopy, atomic force microscopy, phase contrast and differential interference contrast microscopy [39-42]. For fluorescence microscopy, biological molecules can be fluorescently stained and the location of a protein can be traced. However, the fluorescence is not permanent and easily fades. In addition, fluorescence labeling can induce adverse effect on the measured molecule or interfere with the parameter assessed. Similarly atomic force microscopy provides a 3D surface profile of the samples. However, this technique is limited by its scanning speed. On the contrary, DHM as described previously is a label-free quantitative imaging technique, able to non-invasively capture the entire complex field distribution including the amplitude and phase information of cardiomyocytes. Consequently, much richer information on the cardiomyocyte structure can be obtained by using DHM. During the lengthy drug discovery process it is crucial to improve the predictability of compound toxicity through safety profiling assays in order that potentially toxic compounds are detected early in the process before significant time and important financial investments are made. Between 1994 and 2006 from the new drugs approved by the US Food and Drug Administration (FDA), 38 were later withdrawn from the market because of safety concerns, the majority being cardiotoxic or hepatotoxic. Safety assements are therefore performed in preclinical drug development for revealing the possible drug side effects in particular those that may affect the electrical conduction and beating of the heart [43-47]. Therefore, researchers and pharmaceutical companies have to ensure that the effect to lead candidate compounds on cardiac function strictly satisfy criteria. Consequently, it is critical to establish more informative in vitro cardiotoxicity screens and data

analysis algorithms at the early phases of drug development for preventing late stage failure [48-50]. In the present work, the dynamic phase profile of beating cardiomyocytes, which are proportional to the optical path delay profile of the cell, are reconstructed from holograms that are captured through DHM. The beating activities of cardiomyocytes, and contraction and relaxation profiles are derived from the reconstructed phase image. In addition, other characteristic parameters used to categorize phenotypes such as rising time, falling time, peak width, and frequency are analyzed. These parameters are valuable for the analysis of drug candidates' effects on cardiomyocytes. More precisely, the dynamic beating profile of cardiomyocytes are obtained with two proposed methods, either by monitoring the average or the variance information of imaged cardiomyocytes. On the other hand, the contraction and relaxation movement of cardiomyocytes are quantified by analysis the difference between two successively acquired DHM phase images. The automated procedure for multiple parameters recording on cardiomyocytes dynamics for application in drug toxicity screens is proposed.

This dissertation is organized as follows. In section 2, the digital holographic microscopy is described. In section 3, the automated analysis of RBCs phase images obtained by DHM with experimental results is given. In section 4, the automated analysis about multiple parameters of dynamic cardiomyocytes images resulted from DHM is presented along with experimental results. Then, this dissertation is concluded in section 5.

2. Digital holographic microscopy

Digital holographic microscopy (DHM) has been studied for application in the field of cell biology, including automated cell counts, recognition, classification, three-dimensional tracking, and discrimination between physiological and pathophysiological states [27-32, 51-55]. Briefly, DHM is a label-free interferometric microscopy technique which provides a quantitative measurement of the optical path length. It is a two-step process where a hologram consisting of an interference pattern is first recorded on a digital CCD camera and the quantitative phase images are reconstructed numerically using a specific algorithm [56-57]. With current computer power, the reconstruction process can be achieved on-the-fly at a speed of 100Hz. The quantitative phase images are related to the optical path difference (OPD),expressed in terms of physical properties as:

$$OPD(x,y) = d(x,y) \times [n_c(x,y) - n_m], \quad (1)$$

where d(x,y) is the cell thickness, $n_c(x,y)$ is the mean intracellular refractive index integrated along the optical axis at the (x,y) position and $n_m$is the refractive index of the surrounding culture medium. Simply, Equation 1 means that the OPD signal is proportional to both the cell thickness and the intracellular refractive index, a property linked to the protein and water content of the cells [54-55]. DHM systems generally use a low intensity laser as a light source for specimen illumination and a digital camera to record the hologram. Here, the 684 nm laser source delivers roughly 200 $\mu w/cm^2$ at the specimen plane - that is some six orders of magnitude less than intensities typically associated with confocal fluorescence microscopy. With that amount of light, the exposure time is only 400 μs. An extensive quality control of DHM can be found in [55]. The schematic of the off-axis digital holographic microscopy is shown in Figure 1.The experimental setup in Figure 1 is a modified MachZehnder configuration with a laser diode source (λ= 684 nm). The

laser beam is divided into a reference wave and an object wave. The object wave is diffracted by the biological samples, magnified by a 40×/0.75NA microscope objective and interferes, in the off-axis geometry, with the reference wave to produce the hologram recorded by the CCD camera. The reconstruction and aberration compensation of the microorganism wavefront is obtained by using the numerical algorithm described in [56-57].

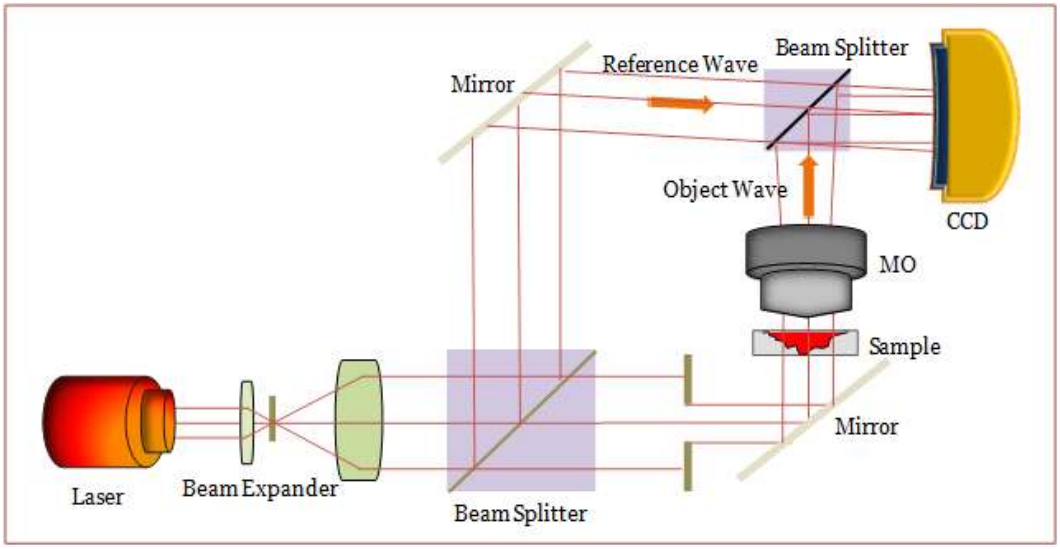

Fig. 1 Schematic of the off-axis digital holographic microscopy.

3. Automated Analysis of Three-dimensional Red Blood Cells

The holograms of RBCs are recorded on CCD camera with DHM technique. Then, the RBCs phase images are numerically reconstructed from these RBC holograms. In this section, the RBC phase images have to be firstly segmented and then the segmented RBCs are used to do following analysis such as quantitative analysis of RBCs stored in different periods and automated counting of morphological normal RBCs.

3.1 Segmentation of Red Blood Cell Phase Images

Image segmentation is defined as partitioning an image into different regions which have similar texture, intensity values, or color. Image segmentation as a preprocessing step is imperative for the analysis of object in a higher level such as image classification, recognition, and tracking [58]. Because of the unnecessary background noise in the computational holographic RBC image, it is also necessary to perform holographic image segmentation algorithm to extract the RBC target which would be used for assessing hematological functions and the presence of disease of RBC. A brief review of segmentation approach is viewed and the segmentation results of RBCs phase images are presented.

3.1.1 Review of Image Segmentation Algorithms

Image segmentation algorithms are useful in the area of medical image analysis, computer vision, object recognition, tracking, and motion analysis [59-60]. Till now, a lot of image segmentation approaches have been proposed

but no one of them can satisfy with the segmentation requirement for all kinds of images. Here, the image segmentation methods are classified into five groups. They are region-based, edge-based, clustering-based, deformable contour model-based, and graph-based segmentation schemes. The most typical and used segmentation algorithms for each category are introduced.

3.1.1.1 Region-based Segmentation

The conventional region-based segmentation methods consists of thresholding, region growing, region splitting and merging.

Thresholding is the simplest and fast algorithm in image segmentation. The grouping of each pixel point belonging to object or background is based on the comparison between pixel intensity value and the given threshold. For instance, f(x,y) is the pixel point value at location of (x,y) in image. It is classified as object if f(x,y)>T while it is viewed as background if f(x,y)≤T where T is the threshold value. This process can be described as following equation:

$$g(x,y) = \begin{cases} 1 & \text{if } f(x,y) > T \\ 0 & \text{if } f(x,y) \leq T \end{cases} \tag{2}$$

where g(x,y) is the segmented image, f(x,y) is the intensity value at (x,y) in the original image, and T is a given threshold. If more threshold values are used, Equation (2) can be extended into multiple thresholding segmentation. For threshold-based method, the choice of threshold is very important. The threshold value can be manually selected or automatically acquired from the analysis of histogram or intensity values of image, such as Otsu's method that can automatically find a threshold maximizing the variance of inter-regions [59].

For region growing segmentation method [59], some seeds representing extracted targets should be selected in advance. Starting from these seed points, neighboring pixel points can be recruited if they are similar with them (similar means similar intensity value). Otherwise, the neighboring pixel is viewed as new seed and used to recruit it's around pixel points. Consequently, the region

connected to the seed points can be grown. The segmentation results of this method are sensitive to the definition of similarity between seed points and their neighboring ones. Also, this method will make the segmentation boundary unsmooth.

For region splitting and merging [59], the original image is first subdivided into some arbitrary, disjointed areas. Then, these small areas are merged or splitted so as to satisfy with the prerequisite conditions. That is, the pixel points belonging to the same region should have similar properties. The traditional region splitting and merging method is described as following steps:

step 1: split the image into four disjoint parts.

step 2: merge any adjacent regions that reach the requirement to be one region.

step 3: iteratively split the sub-region and merge neighboring regions until no further merging or splitting is possible.

The region splitting and merging segmentation approach is sensitive to the splitting and merging condition, and the segmented edge of target will be also unsmooth as region growing segmentation algorithm.

3.1.1.2 Edge-based Segmentation

Edge detection method can find discontinuities in image with first or second-order derivative and the discontinuities always correspond to object edge. Edge detection methods include Sobel, Prewitt, Roberts, Laplacian of a Gaussian, and Canny [59]. Since image usually includes many fault edges, direct edge detection method cannot get good segmentation results. Usually, segmentation method based on edge detection is combined with other methods such as morphology operation [61]. Here, one of the most famous edge detection methods-Canny edge detector and one segmentation method-watershed transform algorithm which can be classified as edge-based segmentation approach are introduced.

Canny edge detection is known as optimal edge detector. This method can reduce the error rate, localize the edge well and response only to single edge. The process of Canny edge detection can be described as following steps:

step 1: smooth the original image with Gaussian filter so as to reduce noise in the image.

step 2: obtain the edge strength with any one of the gradient operators such as Sobel, Roberts, and Rprewitt.

step 3: suppress non-maxima pixels. It is implemented by checking whether the point gradient is greater than its two neighbors along the gradient direction. If so, it means this point may be the edge point and thus the corresponding value is kept. Otherwise, the value is set to be zero.

step 4: using two thresholds ($T_1 < T_2$) to threshold the previous result. The bigger threshold value can reserve apparent edges while the smaller one can keep the week edges.

step 5: connect edge segments in thresholded image obtained with threshold value of T_2 with edge segments that result from segmented image by using threshold value of T_1. When the edge segments result from threshold value T_1 can link the edge segments obtained from threshold value T_2, then these edge segments from T_1 are used to form the final edge by combining with the edge segments from threshold value of T_2.

Watershed transform segmentation is from the flooding simulation [59]. The gray scale image is regarded as topological surface and the regional minimal values are taken as valleys while regional maximal values are viewed as peaks. When water emits from the valleys, dams are built so as to prevent water in valleys from merging together. That is, the watershed transform can find peak value between two neighboring valleys. The flooding simulation of watershed transform algorithm is illustrated in Figure 2 with one dimension. Usually, watershed transform is applied to gradient image since the edge having high gradient corresponds to the peaks. The implementation of watershed transform

can be found in [62]. Since there are many regional minimum and maximum values in original image, it is easy to produce over-segmentation problem when the watershed transform is applied to image directly. In order to solve this problem, marker-controlled watershed transform algorithm is proposed. In this algorithm, the regional minimum values only happen at the locations that are marked. These makers consist of internal and external makers. Internal makers usually denote the extracted targets while the external markers represent the connected background.

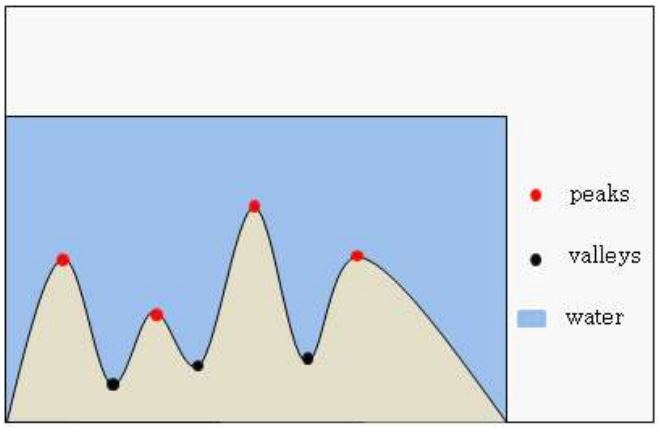

Fig. 2 Illustration of watershed transform algorithm

3.1.1.3 Clustering-based Segmentation

Clustering-based segmentation algorithms assume that the same object would have similar intensity values. Supervised and unsupervised clustering methods [63] which include hierarchical clustering, partitional clustering, k-means clustering, and fuzzy clustering methods can be used for image segmentation. Here, the k-means clustering and mean shift segmentation method which is also regarded as partitional clustering approach are briefly introduced.

For k-means clustering method, the number of cluster has to be defined before applying it to image. K-means method tries to minimize a within-cluster

sum of squares. Namely, attempt to minimize the following term [64]:

$$\arg\min_{s} \sum_{i=1}^{k} \sum_{x_j \in S_i} D^2(x_j, \mu_i) \tag{3}$$

where k is the cluster number, S_i is the set of the ith cluster and μ_i is the mean value of the ith cluster, $D^2(x_j, \mu_i)$ is the distance between a pixel point value and the mean value μ_i of the ith cluster. The procedure for minimizing formula 3 is described as following procedures:

step 1: define the number of cluster k.

step 2: randomly choose k points from the observations/pixel points as centroid points.

step 3: group each point to one of the k clusters by comparing the similarity between the point and the k centroid points. The comparing point is classified into the group with the most similarity. This step will be conducted to all of the observation points.

step 4: update the centroid points with the previous result and then do step 3. The last two steps will be repeated until the centroid points are converged.

When the k-means clustering method is applied to image segmentation, the number of object should be known and the values of pixel point within each object should be similar.

Mean shift [65-67] is a kind of gradient ascent segmentation method. Firstly, the image data should be transformed into probability density by using kernel density estimation [66-67].The density obtained by kernel estimation is much smoother than that from histogram. Then, mean shift algorithm is applied to each point on the density where the mean shift vector will point to the gradient. Consequently, each point will converge to the closest mode where the mode is considered as a cluster center. Thus, the points that share the same mode are regards as the same cluster belonging to the same object. The segmentation procedure of mean shift algorithm is given as following steps.

step 1: estimate density of image with kernel density estimator as following equation:

$$\tilde{f}(x) = \frac{1}{nh^d} \sum_{i=1}^{n} K\left(\frac{x - x_i}{h}\right) \tag{4}$$

when the spatial (image lattice) and range (graph level or color of spectral information) domains are considered, K(x) can be expressed as follows.

$$K(x) = ([x^s \ y^r]) = \frac{c}{h_s^d \, h_r^p} k\left(\left\| \frac{x^s}{h_s} \right\|^s \right) k\left(\left\| \frac{y^r}{h_r} \right\|^2 \right) \tag{5}$$

where k(x) is epanechnikov kernel function, h is the size of moving window, d and p are dimension number while c is used to normalize the function of K(x).

step 2: for each image pixel x_i , initialize $y_{i,1} = x_i$ and then apply mean shift algorithm to it until convergence. The new point resulting from x_i by using mean shift algorithm is derived as following iteration equation.

$$y_{i,j+1} = \sum_{i=1}^{n} x_i g\left(\left\| \frac{y_{i,j} - x_i}{h} \right\|^2 \right) / \sum_{i=1}^{n} g\left(\left\| \frac{y_{i,j} - x_i}{h} \right\|^2 \right) \tag{6}$$

where g(x)=k′(x), n is the number of samples (pixel points) within the moving window.

step 3: update the pixel value of x_i as $z_i = (x_i^s, y_{i_{con}}^y)$. That is, the value of pixel point at location x_i^s is assigned with the converged feature point $y_{i_{con}}^y$ which is the mode in the probability density. As a result, pixel points with the same mode are viewed as the same cluster and belong to the same object.

The above three steps are the fundamental procedures for image segmentation with mean shift algorithm. However, it is also easy produce over-segmentation problem. For better segmentation performance, more procedures such as merging smaller regions should be included.

3.1.1.4 Deformable Contour Model-based Segmentation

There are two kinds of deformable contour model-based segmentation method [68-69]. They are parametric model and geometric deformable mode. The former is usually referred to as snake and the latter one as level set. The contour in a

parametric model is propagated directly on the image which means the points on the curve is parameterized and evolved explicitly while the evolution of contour on the level set is independent to any parameterization and the curve is propagated implicitly by evolving a surface in a high dimension. The basic concept about snake and level set are described as follows.

The curve in snake model is defined as $v(s)=[x(s),y(s)]$ where x(s) and y(s) are x and y coordinates in image and $s\in[0,1]$ are points on the snake. The segmentation is achieved by minimizing an energy function on the snake which is expressed as follows [69-70]:

$$E_{snake}=\int_0^1 E_{snake}(v(s))ds \tag{7}$$

$$=\int_0^1 (E_{cur}(v(s))+E_{img}(v(s))+E_{con}(v(s)))$$

where E_{cur} is the internal energy due to bending of curve, E_{img} is energy from image force and E_{con} is energy from external constraint forces defined by user. The internal and image energy can be simpled expressed as following equations for image segmentation.

$$E_{cur}=\alpha(s)\left|\frac{dv}{ds}\right|^2+\beta(s)\left|\frac{d^2v}{ds^2}\right|^2 \tag{8}$$

$$E_{img}=-|\nabla f(x,y)| \tag{9}$$

where $\alpha(s)$ and $\beta(s)$ specify the elasticity and stiffness of the snake, $\nabla f(x,y)$ is the image gradient. When calculus of variation [] is applied to the functional in equation 7, the Euler-Lagrange condition can be derived as follows.

$$\nabla E_{ext}(v)-\frac{d}{ds}\alpha\frac{dv}{ds}+\frac{d^2}{ds^2}\beta\frac{d^2v}{ds^2}=0 \tag{10}$$

where $E_{ext}=E_{img}+E_{con}$. Then, the evolution equation can be formed as equation 11.

$$v(s,t+1)= \left(\frac{d}{ds}\alpha\frac{dv(s,t)}{ds}-\frac{d^2}{ds^2}\beta\frac{d^2v(s,t)}{ds^2}-\nabla E_{ext}(v(s,t))\right)\times\Delta t+v(s,t) \tag{11}$$

However, the implementation is easy to suffer from numerical instability and

numerous parameters have to be designed. Many kinds of varied snakes can be found in [71-73].

The snakes cannot properly deal with split and merge problem during image segmentation while level set can solve those disadvantages. As level set [74-75], the curve X(s,t) is embedded into a level set function $\Phi(x,y,t)$ and the curve is obtained by determining zero level set in the level set function. Consequently, the curve can be obtained by evolving the level set function and be chosen as the zero level set instead of evolving the curve explicitly. The embedded curve in level set can be described as following equation [68].

$$\Phi(X(s,t),t)=0 \tag{12}$$

use chain rule and do differential to Equation 12 with respect to t, the following equation can be achieved:

$$\frac{\partial \Phi}{\partial t}+\nabla \Phi \frac{\partial X}{\partial t}=0 \tag{13}$$

when the speed of the curve $\partial X/\partial t = V(c)N$ and the inward unit normal of level set curve $N=-\nabla\Phi/|\nabla\Phi|$ is inserted into Equation 13, the curve evolution using the level set method can be described as follows:

$$\frac{\partial \Phi}{\partial t}= V(c)|\nabla \Phi| \tag{14}$$

where V(c) is the speed function. The basic speed function from image can be written as $1/(1+|\nabla(G_\sigma * I)|)$ where $\nabla(G_\sigma * I)$ denotes the gradient of smoothed image with Gaussian filter. As implementation, an initial level set function that the curve has zero level set should be defined. Since Equation 14 is defined only for zero-level set, other level sets also need to be defined for implementation. A large number of varied level set methods can be found in [76-81].

3.1.1.5 Graph-based Segmentation

The snake and level set segmentation method can be also classified as

energy-based segmentation algorithm. These methods cannot reach global minimum energy during function minimization. Here, only the graph cut segmentation approach [82-85] which try to minimize an energy function with graph cut and can achieve global minimum value is focused.

A graph denoted as G=<V,E> includes node and weight. The cut is the total weight of edges that have been removed between two groups resulted from a cut in the graph. Image segmentation based on graph cut is to find the minimum cut which can reach minimum energy. The energy for graph cut segmentation is defined as following equation [82-83].

$$E(A) = \lambda R(A) + B(A) \tag{15}$$

where R(A) and B(A) are defined as:

$$R(A) = \sum_{p \in P} R_p(A_p) \tag{16}$$

$$B(A) = \sum_{p \in P} \sum_{p,q \in N} B_{p,q} \delta(A_p, A_q) \tag{17}$$

$$where \;\; \delta(A_p, A_q) = \begin{matrix} 1 & A_p \neq A_q \\ 0 & A_p = A_q \end{matrix}$$

where R(A) is called as regional term and defines the penalties for assigning A_p (pixel point p on image) to object or background which can be denoted as $R_p('obj')$ and $R_p('bkg')$, B(A) is the boundary term which describes the boundary properties of the segmentation, λ is the relative importance factor between regional and boundary term. The energy function in Equation 15 can be minimized by the graph cut theory while the cut is the segmentation boundary. To get segmentation result, the graph should be established first by using the original image. Then, the minimum cut of the graph can be obtained by max-flow algorithm [59] which can achieve the minimum cut. When the result is not good, the refinement/interactive process can be used. For graph construction, two extra terminal nodes (other nodes that are not from image pixel points) which represent object and background are applied and this kind of graph is called as s-t graph. After the nodes are defined, next step is to give weight to the corresponding edges. The weight can be given as criterion

shown in Table.1 [82-83].

Table. 1 Graph Construction

Edge	Weight	Condition
n-link {p,q}	$B_{\{p,q\}}$	$p,q \in N$
t-link {p,s}	$\lambda R_p('bkg')$	$p \in P,\ p \in O \cup B$
	K	$p \in O$
	0	$p \in B$
t-link {p,t}	$\lambda R_p('obj')$	$p \in P,\ p \in O \cup B$
	0	$p \in O$
		$p \in B$

where n-link is the edge between nodes in image, t-link is the edge between nodes in image and two terminal nodes (s and t nodes), $B_{\{p,q\}}, R_p('bkg')$, K, and $R_p('obj')$ are defined as follows:

$$B_{\{p,q\}} \propto \exp\left(-\frac{(I_p - I_q)^2}{2\sigma^2}\right) \tag{18}$$

$$K = 1 + \max_{p \in P}\left(\sum_{q:\ \{p,q\} \in N} B_{(p,q)}\right) \tag{19}$$

$$R_p('obj') = -\ln \Pr(I_p|O) \tag{20}$$

$$R_p('bkg') = -\ln \Pr(I_p|B) \tag{21}$$

where {p,q} denotes two neighboring nodes in image, $\Pr(I_p|O)$ and $\Pr(I_p|B)$ denote the intensity distribution of object and background which are usually estimated from the seed points that are manually selected or automatically detected. When the weight in graph is assigned as the method showed in Table.1, the min-cut can be achieved by max-flow method and the minimum energy in Equation 15 is achieved while the cut edge is corresponding to the segmentation results. The graph cut segmentation is widely used in interactive segmentation approach.

3.1.2 Segmentation Results of Red Blood Cell Phase Images

Red blood cells of healthy laboratory personnel were obtained from the Laboratoire Suisse d'Analyse Du Dopage, CHUV. The RBCs were stored at $4^{\circ}C$ and DHM measurements were conducted on several days after the blood were drawn from the laboratory personel. 100-150μl of RBC stock solution were suspended in HEPA buffer at 0.2% hematocrit. 4μl of the erythrocyte suspension were diluted to 150μl of HEPA buffer and introduced into the experimental chamber, consisting of two cover slips separated by spacers 1.2 mm thick. Cells were incubated for 30 min at a temperature of $37^{\circ}C$ before mounting the chamber on the DHM stage. All experiments were conducted at room temperature ($22^{\circ}C$).

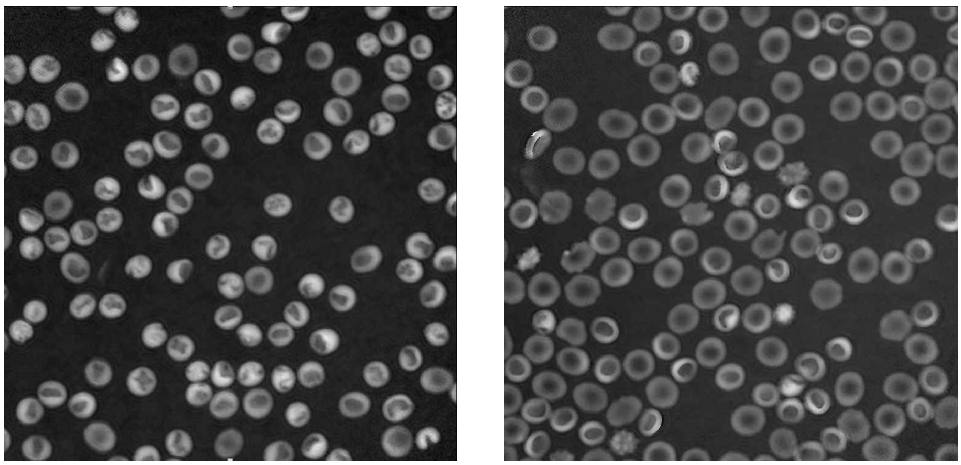

(a) (b)

Fig. 3 Reconstructed RBCs phase images. (a) The RBCs with predominantly stomatocyte shape. (b) The RBCs with predominantly discocyte shape

The RBC phase images are numerically reconstructed from the RBC holograms that are recorded with DHM. Two of the reconstructed RBC phase

images are shown in Figure 3. The Figure 3(a) are reconstructed RBCs phase image with RBCs of predominantly stomatocyte shape and Figure 3(b) are reconstructed RBCs phase image with RBCs of predominantly discocyte shape. By analyzing a series of segmentation methods, the marker-controlled watershed transform segmentation method combined with morphological operation is applied to remove the unnecessary background existed in RBCs phase image due to its advantage in terms of getting isolated target. The detail procedures for segmenting RBCs phase images with marker-controlled watershed transform can be found in [37]. Consequently, each RBC can be separately extracted and the corresponding features can be measured for the further analysis. Two of the segmented RBCs phase images are given in Figure 4.

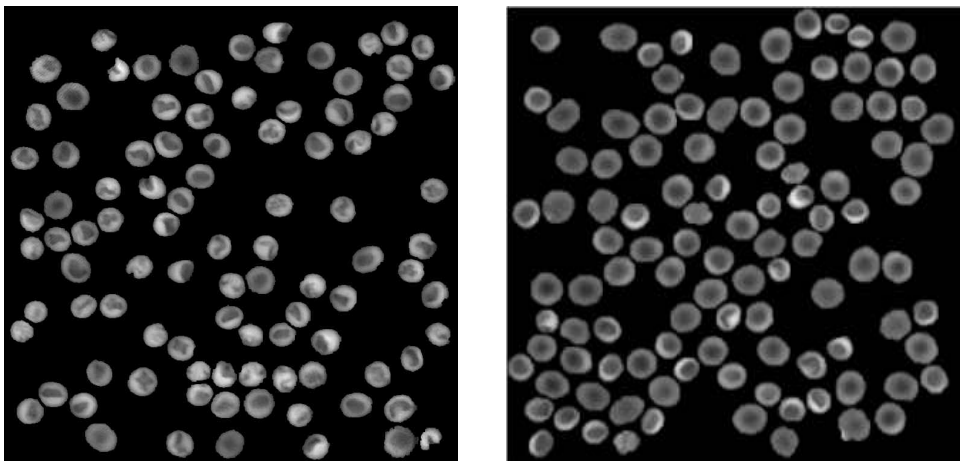

(a) (b)

Fig. 4 The segmented RBCs phase image. (a) The segmented RBCs of Fig.3(a) (b) The segmented RBCs of Fig.3(b).

Moreover, the inside part of RBCs are also helpful for the analysis of RBC-related disease. It is meaningful to extract the inner part of RBCs as well. The marker-controlled watershed transform method can also be used to segment the inside area of RBCs based on the segmented RBCs phase images shown in Figure 4. Consequently, it is easy to derive the outer part of RBCs

once the inner parts are obtained. The segmentation results of inner and outer part of RBCs are given in Figure 5 [37].

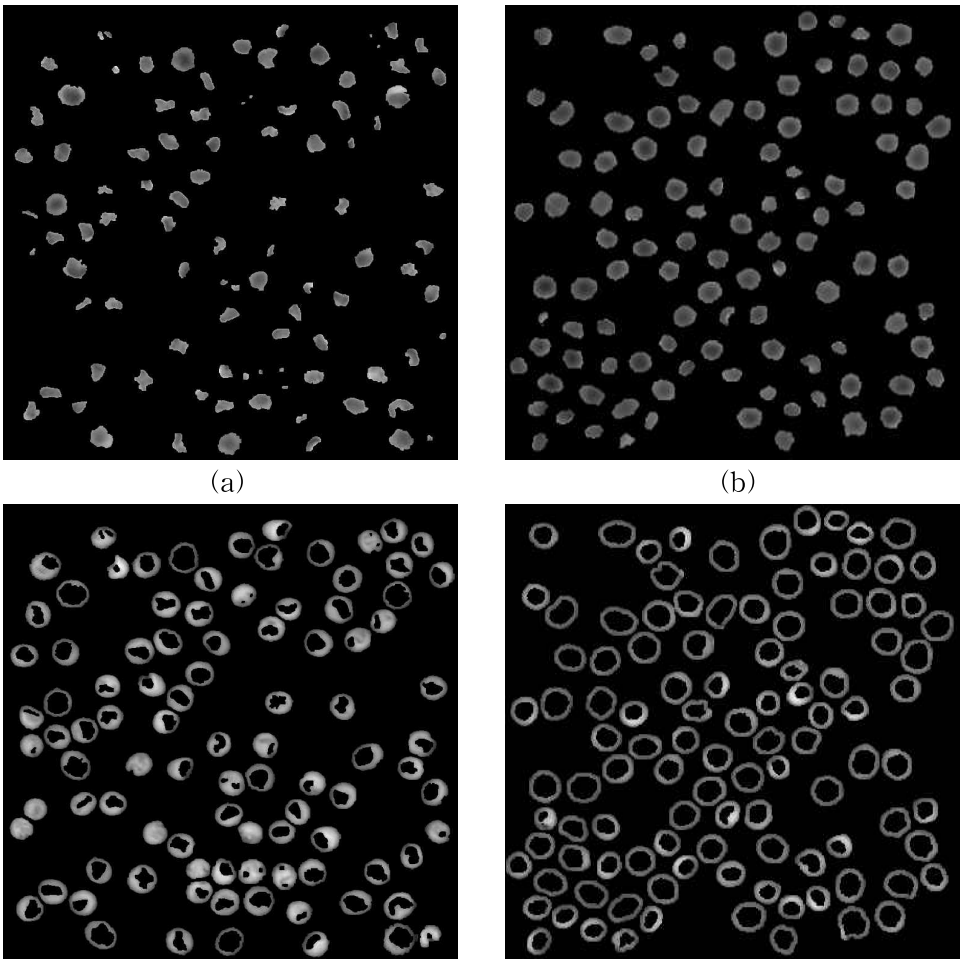

Fig. 5 Segmentation results of the inner and outer parts of the RBC phase images. (a) and (b) are the inner part of RBCs in Fig. 4(a) and (b). (c) and (d) are the outer part of the RBCs in Fig. 4(a) and (b).

It is noted from Figure 4 and Figure 5 that the marker-controlled watershed transform segmentation method combined with morphological operation can segment the RBCs phase image properly, not only robust to the whole RBCs

but also to the inner and outer part of the RBCs. This segmentation method can be used to segment the RBCs phase images and do the further analysis about RBCs.

3.1.3 Performance Comparison and Evaluation

The segmentation results about RBCs with predominantly stomatocyte and discocyte shape are compared and evaluated. These RBCs segmented with conventional marker-controlled watershed algorithm in [59] are given in Figure 6. It is noted from Figure 4 and Figure 6 that our method can get much better segmentation results in terms of over-segmentation and under-segmentation.

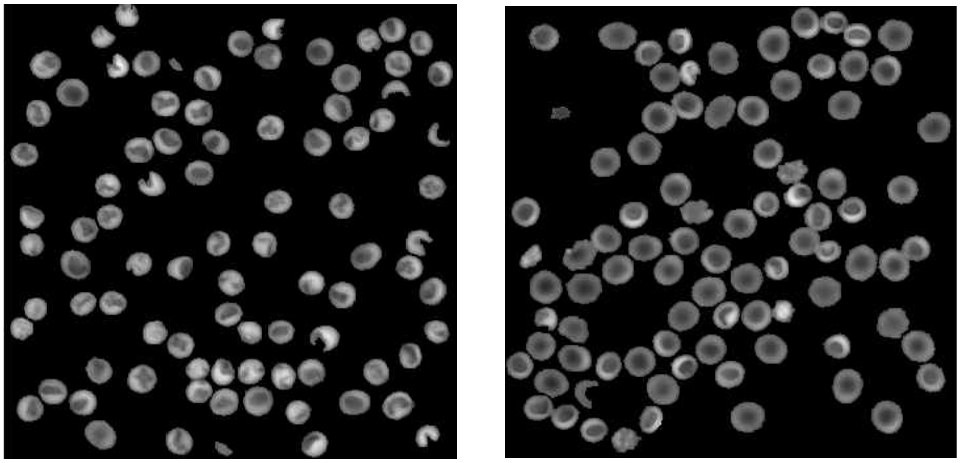

(a) (b)

Fig. 6. The segmented RBCs with marker-controlled watershed method in [59]. (a) The segmented RBCs of Fig. 3(a) (b) The segmented RBCs of Fig. 3(b).

Moreover, a scientific tool developed by F. Sadjadi [103], which is based on the experimental design methodology and independent of the systems output has been applied for performance evaluation. The performance comparison of two algorithms with biased results is mainly dependent on the varied parameters in

segmentation. The procedure of the performance evaluation approach can be briefly described as steps of data characterization, data sampling, primary parameter selection, parameter sampling, performance metrics definition, performance model calculation and statistical analysis. The quantitative phases of RBCs in this study are given to two categories namely stomatocyte and discocyte shape RBCs. The primary parameter which largely affects the segmentation result in our procedure is the value of threshold obtained by Otsu's method while the main parameter for the marker-controlled watershed in [59] is also a threshold which is used to find the regional minimum values. The assessment of segmentation results for RBC inner and outer parts are not conducted because they heavily rely on the previous segmentation results. For the performance metrics, the segmentation accuracy is adopted and it is simply defined as the absolute value of correlation between segmented RBCs image and reference image which is manually obtained. The closer the segmented image is to the reference image, the closer the segmentation accuracy will tend to approach 1.

The homologous performance models between segmentation accuracy and threshold for RBCs with stomatocyte and discocyte shape are presented in Figure 7. For curve fitting, the least square error estimation technique was employed and the polynomials were examined with degrees up to 6. Then, statistical analysis of Chi-squared test was performed for checking of the similarity between the obtained results (the measured data with the segmentation method and that in the fitted polynomial) [103]. Consequently, the p-values for the null hypothesis that the predictive performance models approximately satisfy with the measured response curve were achieved to be 0.7578, 0.3571, 0.9135 and 0.1213 for Figure 7(a), (b), (c) and (d) respectively. Therefore, the null hypothesis that the fitting curve is similar with the measured one should be accepted at the 0.05 level of significance. It is also noted that the maximum segmentation accuracy in our method outperforms that presented in [59].

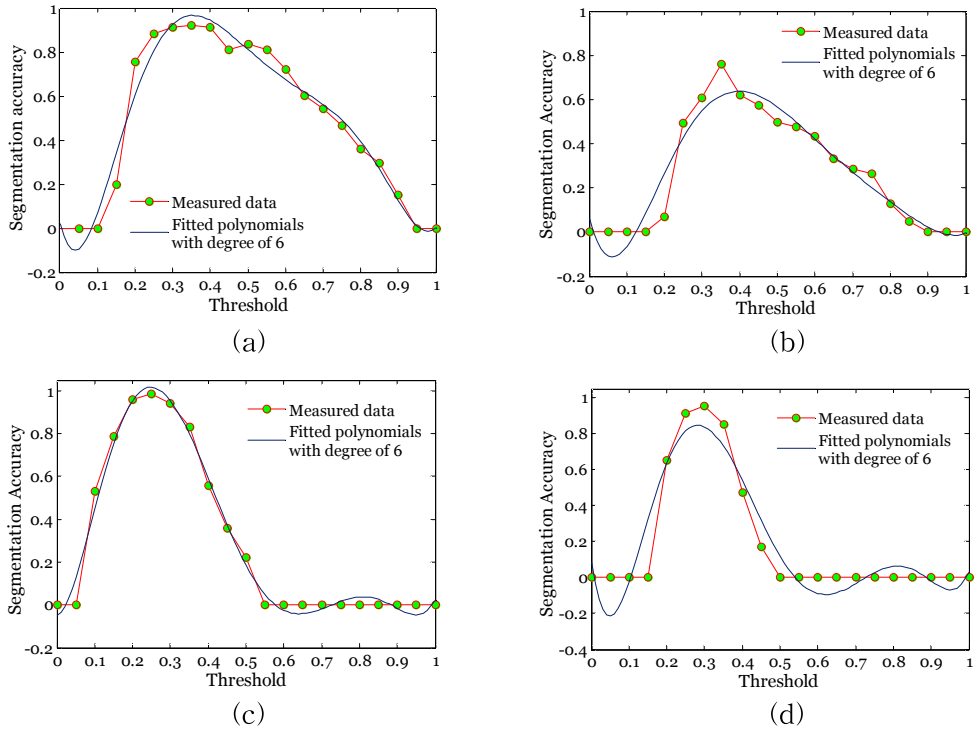

Fig. 7 Performance models. (a) and (b) are performance models for RBCs with stomatocyte and discocyte shape in the method of [59]. (c) and (d) are performance models for RBCs with stomatocyte and discocyte shape in our proposed procedure.

3.1.4 Subsection Summaries

In summary, all of the segmentation methods can work well for image that the target is very different from the background and the intensity values of the pixel points of the same region are very similar. Among these segmentation approaches, thershold-based method has the advantage of fast computation time. However, it is difficult to choose an appropriate threshold. Region growing, region splitting and merging method can get better segmentation results when the property of target is very similar. This kind of method suffers from unsmooth boundary and is not easy to define the stop criterion. In addition, this

method is not good for segmented targets with weak boundary. As edge-based segmentation algorithms, the most used methods such as Sobel, Prewitt, Roberts, Laplacian of a Gaussian and Canny will work well when they are combined with other post-processing techniques such as morphology operation. It is also easy for these methods to produce false edges due to image noise. For watershed transform segmentation algorithm, it has the advantage to get isolated object and disadvantage of producing over-segmentation. However, when the object can be approximately detected, the marker-controlled watershed algorithm will work well and can reduce the over-segmentation problem. Usually, the segmentation results are not good when the edge-based method is used solely. For clustering-based segmentation, assumption that each region should have similar property is required. This kind of method is also robust to color image. After clustering the pixel point, post processing such as merging small region is necessary. Snakes and level set segmentation method can be applied to medical image with heavy noise and weak edge in object. Compared with snakes, level set algorithm can solve the split and merge problem during the curve evolution. These kinds of methods are widely used in biomedical images. For the graph cut segmentation method, the regional and boundary information on image are combined. The graph cut can work well when different targets are existed in image. The graph cut method can get appropriate segmentation results to all kinds of image when the user's intervention is introduced. All kinds of segmentation methods have many improved version which can reach an acceptant execution time. For the segmentation of RBCs phase images, the RBCs phase images are segmented by using marker-controlled watershed transform algorithm due to its advantages of achieving isolated object while the internal and external markers are identified with morphological operation and thresholding technique. Moreover, the execution time of watershed transform algorithm is acceptable compared with active contour and graph-based segmentation approaches.

3.2 Quantitative Analysis of Human Red Blood Cells Stored in Different Periods

In this section, the modifications of the 3D morphology and mean hemoglobin (MCH) in RBCs induced by the length of storage time for the purpose of 3D classification of RBCs having different storage periods by using an off-axis DHM is studied. To analyze the morphological changes in RBCs induced by the length of storage time, datasets from blood samples stored for 8, 13, 16, 23, 27, 30, 34, 37, 40, 47, and 57 days are used, respectively. The datasets are divided into eleven classes of RBCs stored in eleven different periods. The eleven classes have more than 3,300 blood cells, with averagely more than 300 blood cells per class. The classes indicate the storage period of RBCs and are listed in chronological order. Using the RBCs donated by healthy persons, off-axis digital holographic microscopy reconstructs several RBC quantitative phase images from each class of blood sample. In order to automatically calculate the characteristic properties such as projected surface area, averaged phase value, corpuscular volume, hemoglobin content and hemoglobin surface density of RBCs, the image segmentation method [37] based on marker-controlled watershed algorithm [59] is applied to remove the unnecessary background in the RBC quantitative phase image. All the RBCs that exist in the quantitative phase image are extracted to measure the characteristic properties of RBCs. Averagely, more than 300 RBCs are extracted from the segmented quantitative phase images for each class of blood sample. The sample size is large enough to allow us to obtain statistical distributions of the characteristic properties of RBCs at a specific storage time. Our main focus is to quantitatively analyze the relationship between the RBC characteristic properties and their aging. This analysis will be beneficial to the understanding of the features of RBCs with different storage periods and evaluation of any modifications in the 3D cell morphology and hemoglobin content induced by the length of storage time.

3.2.1 Sample Preparation

The original RBC's were donated by healthy people and stored in a transfusion bag which were obtained from the Service Régional Vaudois de Transfusion Sanguine in Switzerland and stored at 4°C during the storage period. The erythrocyte concentrate was extracted from the blood transfusion bag and diluted in HEPA buffer (15 mM HEPES pH 7.4, 130 mM NaCl, 5.4 mM KCl, 10 mM glucose, 1 mM CaCl2, 0.5 mM MgCl2 and 1 mg/ml bovine serum albumin) at a concentration of ~ 0.15 % Vol. 0.2 ml of the erythrocyte suspension was then introduced into the experimental chamber, consisting of two coverslips separated by spacers 1.2 mm thick. In order to allow for sedimentation of the cells on the bottom coverslip, cells were incubated for 30 min at a temperature of 37°C before mounting the chamber on the DHM stage. All experiments were conducted at room temperature.

3.2.2 Three-dimensional Sensing and Segmentation of Red Blood Cells

To analyze morphological changes in RBCs induced by the length of storage time, eleven classes of blood samples stored for 8, 13, 16, 23, 27, 30, 34, 37, 40, 47, and 57 days were prepared. The off-axis DHM reconstructed several RBC quantitative phase images for each class of blood samples, where holograms of RBC preparations were acquired in an out-of-focus plane. In-focus phase images of RBCs were obtained through a numerical reconstruction of the object wavefront and subsequent digital propagation of the reconstructed field to the focus plane. Most of the contained RBCs are discocyte RBCs which have a discoid-shape. Some of the reconstructed RBCs phase images are given in Figure 6 [86].

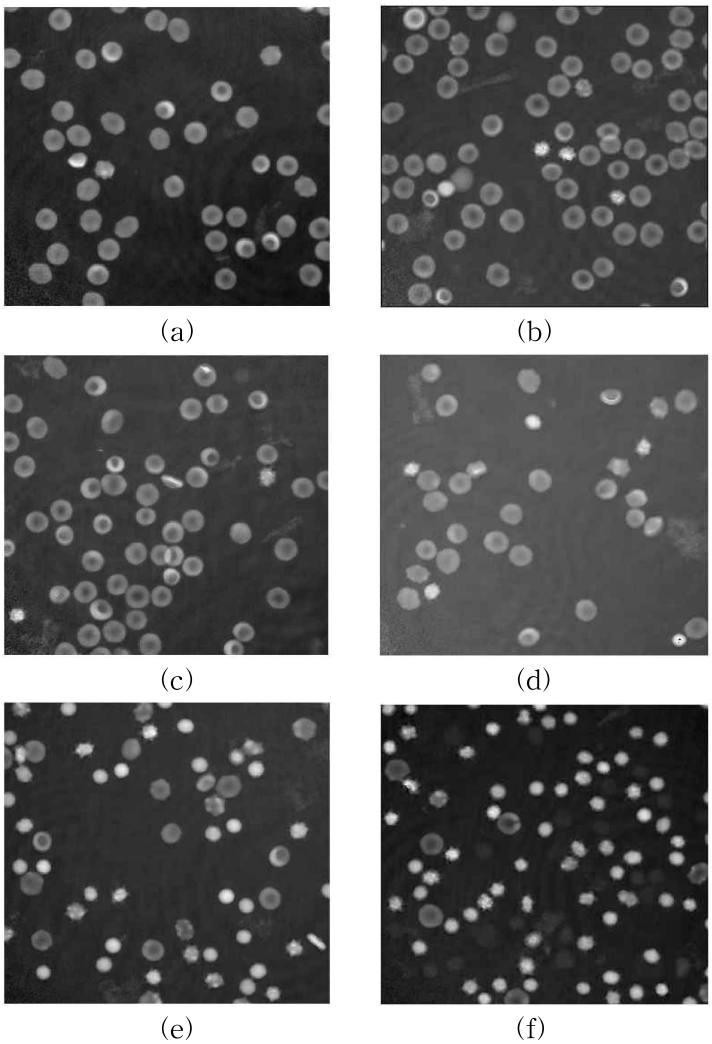

Fig. 8 Reconstructed RBCs images at different storage days. (a)-(f) are RBCs with 8, 16, 30, 34, 47 and 57 days of storage, respectively.

For automated investigation of the characteristic properties of RBCs, individual RBC must be extracted from the quantitative phase image. The segmentation method based on marker-controlled watershed algorithm as described in section 3.1 is applied to remove the background from the quantitative phase images. For the purpose of comparing the RBC quantitative phase images with different storage times, the phase value of the background of

the RBC quantitative phase image is set to 0°. The corresponding segmentation results for RBCs phase images shown in Figure 8 are given in Figure 9.

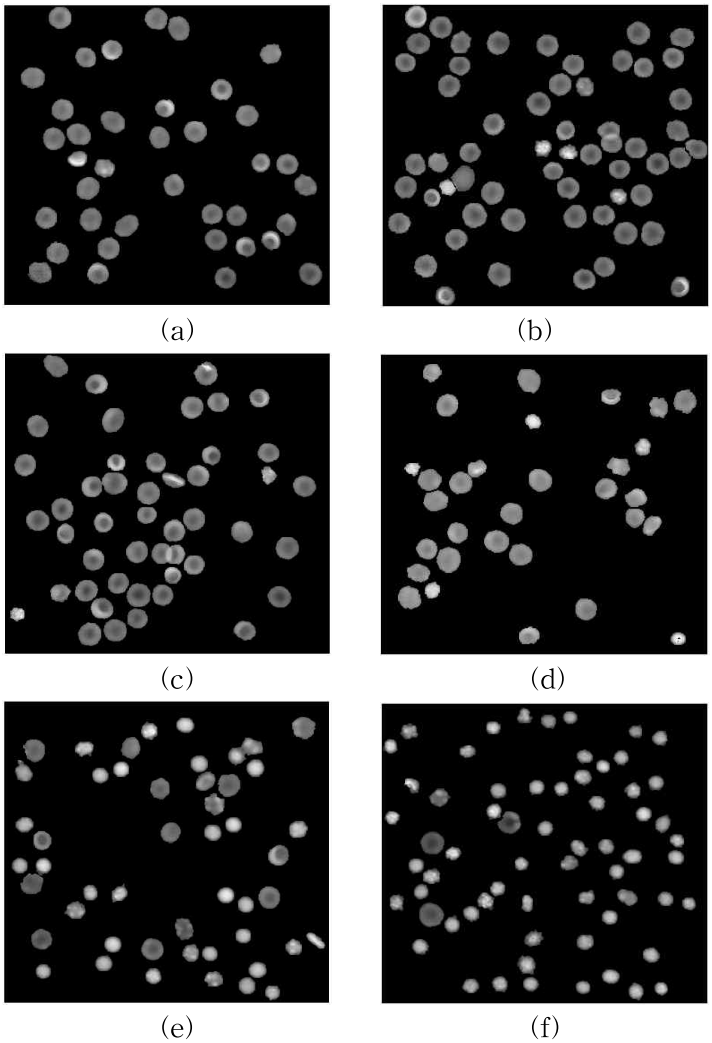

Fig. 9 Segmentation results of Reconstructed RBCs images at different storage days. (a)-(f) are the corresponding segmented RBCs images shown in Fig.6 (a)-(f) with 8, 16, 30, 34, 47 and 57 days of storage, respectively.

3.2.3 Measurement of Red Blood Cells Features

The characteristic properties used to analyze the 3D morphological changes in RBCs induced by the length of storage time are the projected surface area, the mean phase value allowing to calculate mean corpuscular volume (MCV), hemoglobin (MCH) – the average volume and mass of hemoglobin per red blood cell in a sample of blood – and MCH surface density (MCHSD), defined as the ratio of MCH to the projected surface, three highly relevant parameters, altered in various pathological states.

The average phase value Φ induced by the whole RBC which is related to the dry mass [87] and the projected surface area S which may influence the functionality of RBCs are defined as follows:

$$\Phi = \frac{1}{N}\sum_{i=1}^{N}\varphi_i \tag{22}$$

$$S = Np^2 \tag{23}$$

where N is the total number of pixels within a RBC, p denotes the pixel size in the quantitative phase image, and φ_i is the phase value of each pixel within the RBC. RBC volume or the size of RBC is a good indicator of the functionality of RBCs. A RBC with a larger volume means a larger surface area and thus can transform more oxygen [88]. It is also beneficial to the diagnosis of polycythemia vera [89]. According to [87], the volume of a single RBC, or the corpuscular volume is denoted as:

$$V \cong \frac{p^2\lambda\sum_{i}^{N}\varphi_i}{2\pi(n_{rbc}-n_m)}, \tag{24}$$

where p is the pixel size in quantitative phase image, φ_i is the phase value of each pixel within the RBC, and λ is the wavelength of the light source. Coherently, when a population of RBCs is considered, Equation. (24) allows us to derive the mean corpuscular volume (MCV) [90]. The refractive index of RBCs, nrbc, has been measured with a dual-wavelength digital holographic

microscope as described in [91]. Here, nrbc, is 1.396 with no significant difference between groups of different ages. The index of refraction of the HEPA medium, nm, is 1.3334. Another important characteristic property is the dry mass which measures the weight of the cell after dehydration. The dry mass is a reliable biomass, which is widely used to compare cells since it is free from the disturbance of water existing in living beings [87]. According to [87, 92], the dry mass of a cell is related to the phase value and can be defined as follows:

$$Dry\ Mass(DM) = \frac{10\lambda}{2\pi\alpha}\int_s \varphi ds = \frac{10\lambda}{2\pi\alpha}\Phi S, \tag{25}$$

where λ is the wavelength of the light source, Φ is the average phase value induced by the whole cell, α is a constant known as the specific refraction increment (in m3/kgordl/g) related mainly to the protein concentration [29]. As far as RBCs are concerned, $\alpha = \alpha_{Hb} = 0.00196$dl/g is the hemoglobin refraction increment between 663nm and 682nm [90]. When a RBC population is considered Equation. (25) provides the mean corpuscular hemoglobin (MCH) according to [92]. The MCH is used as an important parameter for the investigation of change in the hemoglobin content in the RBCs.

The last property used to evaluate the morphological changes in RBC induced by the length of storage time is the MCH surface density (MCHSD), which can show the hemoglobin concentration. It is defined as the ratio between MCH and projected surface area S as follows:

$$MCHSD = \frac{MCH}{S} \tag{26}$$

All the properties defined as in the above equations can be appropriately calculated and compared by using the segmented RBCs phase images stored at different periods.

3.2.4 Experimental Results and Discussion

After segmentation and extraction of RBCs from the quantitative phase images, the characteristic properties including the mean projected surface area $\overline{S}$, the mean average phase value $\overline{\Phi}$, MCV, MCH and MCHSD as well as their standard deviation were calculated for each class of blood sample with method of moments [34]. In the same way, the mean and standard deviation of the projected surface area for RBCs with different storage periods can be calculated. The other properties of RBCs including corpuscular volume (CV) hemoglobin (CH) and hemoglobin surface density (CHSD) can also be obtained by the method of moments. Table 2 shows the calculated mean and standard deviation for all of the characteristic properties of RBCs with different storage times [86].

Table. 2 Characteristic properties of RBCs with different storage days

storage time[days]		8	13	16	23	27	30	34	37	40	47	57
projected area	mean	45	46	47	45	47	42	43	41	39	34	26
	std	5	6	7	7	10	8	9	8	9	9	6
Mean phase value	mean	74	74	81	76	77	76	78	87	96	112	136
	std	12	15	16	16	15	24	21	26	27	28	28
CV	mean	91	92	102	94	98	88	86	93	98	98	94
	std	9	12	14	14	15	20	12	11	12	13	11
CH	mean	32.2	32.3	35.7	32.8	34.8	29.2	30.9	32.7	33.6	34.6	32.5
	std	5.0	5.5	7.7	7.3	8.6	7.6	6.1	5.7	5.0	6.8	5.1
CH surface density	mean	0.70	0.70	0.76	0.71	0.72	0.71	0.73	0.82	0.90	1.05	1.28
	std	0.11	0.13	0.14	0.15	0.14	0.23	0.20	0.24	0.25	0.26	0.26

All of the property values are measured automatically once the RBC phase images are successfully segmented. It can be seen from Table.2 that the mean phase value and CH surface density have similar variation tendency that tend to increase as the increase of storage time. For CV and CH, they don't change quickly as the extension of storage time and seem to fluctuate around their

respective mean value. In contrast, the RBC projected area is obviously decreased as the increase of storage days. On the other hand, the standard deviations for all of these properties achieve significant value when the RBCs storage time is around 30 days (27-34days). Around 30 days' storage, the standard deviations of projected area, CV and CH achieve big value. As RBCs mean phase value and CH surface density, the standard deviations are inclined to increase at the time with 30 storage days. These phenomena may be explained that the RBCs are suffering from drastic variation when the stored days are around 30 days.

In order to view the trend of the modification of the 3D morphology of RBCs as a function of storage time, the mean and standard deviation are plotted against storage time.

Figure 10 presents the relationship between the mean projected surface area, mean average phase value and the varied storage time of RBC samples. It was discovered that the variation trends of RBC projected surface area and the average phase value are almost opposite as the increase of storage days.

Figure 10(a) shows the relationship between the mean projected surface area $\overline{S}$ and storage time. Roughly, the trend of $\overline{S}$ of RBCs decreases with increasing storage time. As shown in Figure 10(a), it is noted that when the storage time of RBCs is less than 27 days, $\overline{S}$ remains quite constant. Furthermore, the decrease rate of $\overline{S}$ for RBCs with storage time less than 34 days is much smaller than that for those with storage time longer than 34 days. When the storage time is longer than 34 days, $\overline{S}$ experiences a substantial decrease. On the other hand, Figure 10(b) shows the relationship between the mean average phase value $\overline{\Phi}$ [see Equation.(22)]and storage time. $\overline{\Phi}$ and its standard deviation are obtained from 300 individual RBCs in each class of blood sample. From Figure 10(b), it can be observed that does not experience a significant change when the storage time is less than around 34 days. In contrast, when the storage time is longer than 34 days, $\overline{\Phi}$ apparently increases. As can be seen

from Figure 10(a) and Figure 10(b), both $\overline{S}$ and $\overline{\Phi}$ remain constant when the storage time is less than around 34 days. However, $\overline{S}$ and $\overline{\Phi}$ change in the opposite directions when the storage time of RBCs is longer than 34 days. Decrease in $\overline{S}$ results in the increasing occurrence of echinocytes in the RBC preparations. RBCs that have aged significantly begin decomposition and have a serrated margin and burr appearance. The RBCs with this morphologic abnormality are called echinocytes.

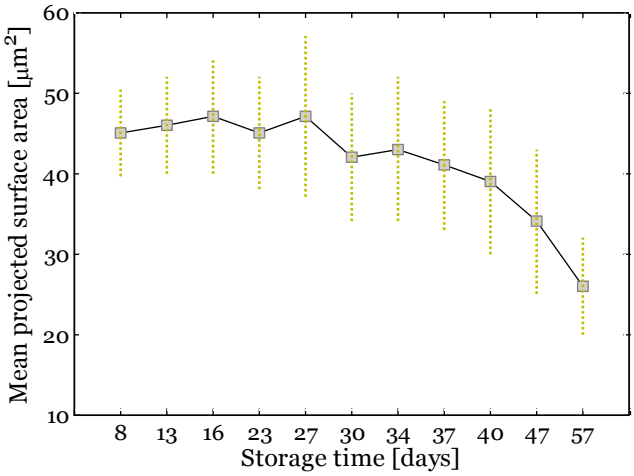

(a)

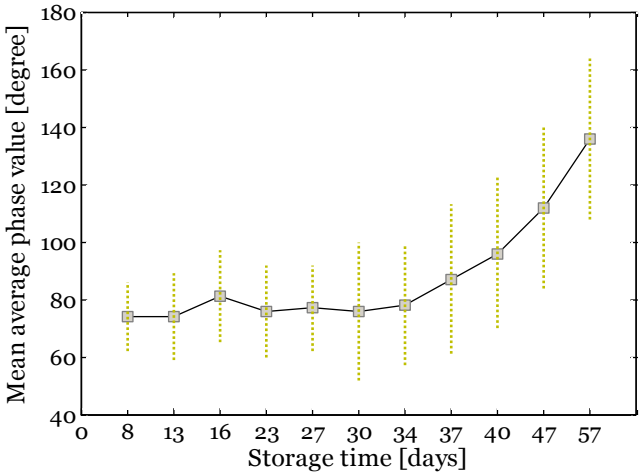

(b)

Fig. 10 Relationship between the mean projected surface areas, mean average phase value and the different storage times. (a) Relationship between S and storage time. (b) Relationship between $\overline{\Phi}$ and storage time. Square and bar are the mean and standard deviation of $\overline{\Phi}$ and S.

Figure 11 illustrates the relationship between RBCs MCV, MCH and the different storage time of RBC samples. The results reveal that the trends for RBCs MCV and MCH with increase storage time are almost the same. In addition, both MCV and MCH values seem to swing around their respective mean value.

Figure 11(a) shows the relationship between the mean corpuscular volume MCV and the storage time. It is noted that the MCV fluctuates around a value of 94 μm^3 even if the storage time of RBCs is increased. Therefore, one conclusion that may be derived is that the MCV is not significantly affected by the storage time. In contrast, Figure 11(b) shows the relationship between the mean corpuscular hemoglobin MCH and RBC storage time. As shown in Figure 11(b), although the MCH fluctuates around a value of 32pg, the MCH is almost stable even if the storage time is increased. Therefore, it may conclude that the hemoglobin content within RBCs does not change as a function of storage time.

Since MCV and nrbc do not vary over storage time, this is an expected result.

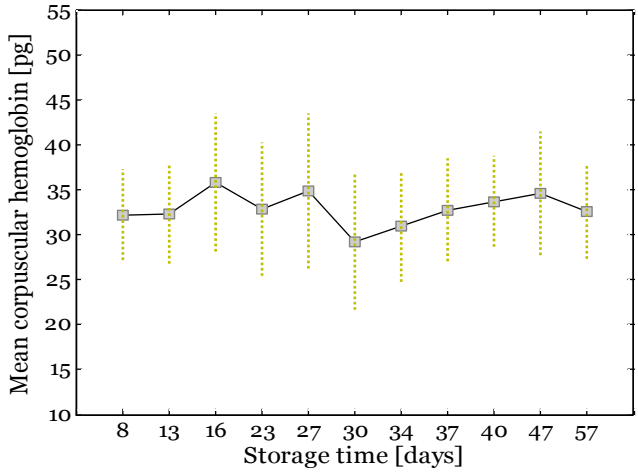

(a)

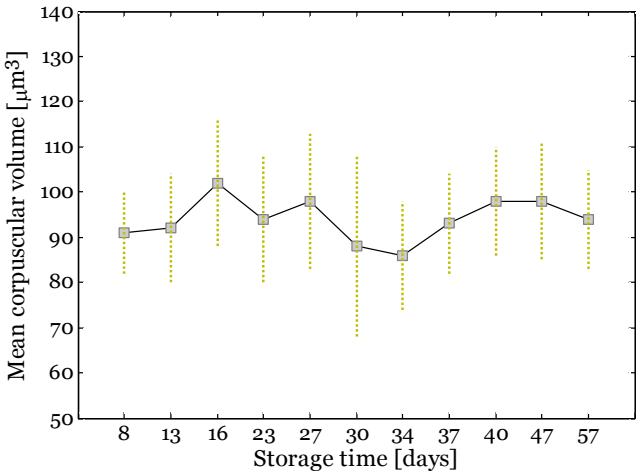

(b)

Fig. 11 Relationship between MCV, MCH of RBCs and varied storage time. (a) Relationship between MCV and storage time. Square is the mean and bar is the standard deviation of corpuscular volume. (b) Relationship between MCH of RBCs and storage time. Square represents the mean and bar represents the standard deviation of the corpuscular hemoglobin content.

Figure 12 shows the relationship between the mean corpuscular hemoglobin surface density MCHSD and storage time. Even though the MCH in Figure

11(b) shows little fluctuations over the storage period, the MCHSD tends to increase as shown in Figure 12. This can be explained by the fact that the MCH remains constant while the mean projected surface area of RBCs tends to decrease with increased storage time. It can also be noted that the MCHSD is almost constant when the storage time of RBCs is less than 34 days. When the storage time is longer than 34 days, the increase in MCHSD is noticeable and the 3D morphological modification of RBC is drastic.

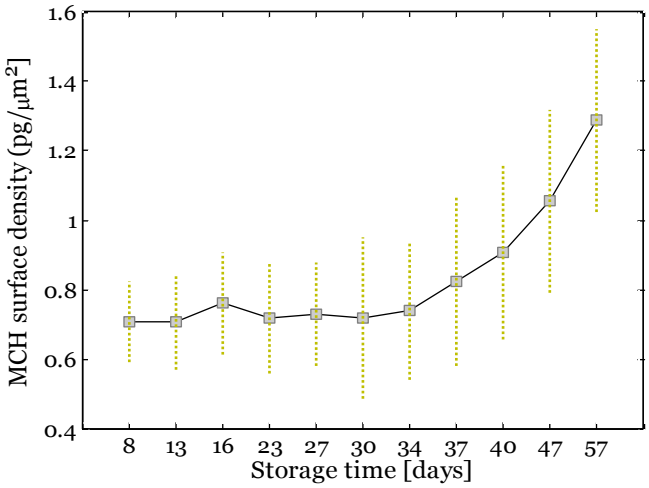

Fig. 12 Relationship between MCHSD of RBCs and varied storage time. Square represents the mean and bar represents the standard deviation of the dry mass surface density.

From the relationship between 3D morphological modifications of RBCs and the storage time, it is found that the MCH of RBCs with different storage times remains constant while the other properties such as $\overline{S}$, $\overline{\Phi}$ and MCHSD change more substantially. When the storage time is less than 34 days, there is no change in the 3D morphology of RBCs. However, when the storage time is longer than 34 days, the morphological change of RBCs is drastic such that the functionality of RBCs can be altered. From these experimental results, it can be seen that the modifications of the 3D morphology and the MCHSD of RBCs are

induced by the length of storage time and that the shelf-life of RBC's may be about 35 days when the blood is stored at refrigerator temperatures [93, 94].

3.2.5 Subsection Summaries

In this section, the 3D morphology and MCH of RBCs with different storage periods are investigated. First, RBC quantitative phase images have been obtained by off-axis digital holographic microscopy and numerical reconstruction method. Then, many single RBCs have been extracted from the RBC quantitative phase images by using the segmentation method based on marker-controlled watershed algorithm. Finally, the characteristic properties of RBCs including projected surface area, average phase value, volume, hemoglobin content and surface density measured at a single cell level have been evaluated over samples of several hundred RBCs using an automated analysis of the quantitative phase images. A statistical analysis indicates that 3D morphological changes in RBCs are induced by the length of storage time, while the hemoglobin content within RBCs is not changed substantially. In addition, it is concluded that 34 days of storage may be a threshold across which the morphology of RBCs starts to change substantially and hence possibly alter their functionality. Automated analysis of the relationship between the characteristic properties of RBCs and storage time may be helpful for drug tests.

3.3 Automated Method for Counting of Morphological Normal Red Blood Cells

The counting morphologically normal cells in human red blood cells (RBCs) is extremely beneficial in the health care field. In this paper, a three-dimensional

(3D) classification method of automatically determining the morphologically normal RBCs in the phase image of multiple human RBCs that are obtained by off-axis digital holographic microscopy (DHM) is proposed. The RBC holograms are first recorded by DHM, and then the phase images of multiple RBCs are reconstructed by a computational numerical algorithm [56-57]. To design the classifier, the three typical RBC shapes, which are stomatocyte, discocyte, and echinocyte, are used for training and testing. Non-main or abnormal RBC shapes different from the three normal shapes are defined as the fourth category. Ten features, including projected surface area, average phase value, mean corpuscular hemoglobin (MCH), perimeter, MCH surface density (MCHSD), circularity, mean phase of center part, sphericity coefficient, elongation, and pallor, are extracted from each RBC after segmenting the reconstructed phase images by using watershed transform algorithm [4]. Moreover, four additional properties, such as projected surface area, perimeter, average phase value, and elongation, are measured from the inner part of each cell that can give significant information beyond the previous ten features for the separation of the RBC groups; these are verified in the experiment by the statistical method of Hotelling's T-square test [96]. The principal component analysis (PCA) algorithm [97] is also applied to reduce the dimension number of variables and establish the Gaussian mixture densities using the projected data with the first eight principal components. Consequently, the Gaussian mixtures are used to design the discriminant functions based on Bayesian decision theory [98]. To improve the performance of Bayes classifier and the accuracy of estimation of its error rate, the leaving-one-out technique is applied [98]. Experimental results show that the proposed method can yield good results for calculating the percentage of each typical normal RBC shape in a reconstructed phase image of multiple RBCs that will be favorable to the analysis of RBC-related diseases. In addition, it shows that the discrimination performance for counting of normal shapes of RBCs can be improved by using 3D features of a RBC.

3.3.1 Bayesian Decision Algorithm

Bayesian decision algorithm is a kind of statistical decision making approach for the problem of pattern classification. The probability of a pattern belonging to a specific class is the combination of prior probability and a likelihood probability which can be expressed as following equation with one feature and n classes [3, 59].

$$P(C_i|x) = \frac{p(x|C_i)p(C_i)}{p(x)}, \tag{27}$$

where $p(x) = p(x|C_1)p(C_1) + p(x|C_2)p(C_2) + \ldots + p(x|C_n)p(C_n)$ is viewed as scale factor so as to make the summation of posterior probabilities $p(C_i|x)$ equal to 1 or just be taken as constant, $p(C_i)$ is the priori probability which represent the probability of class i appeared among all of the populations while conditional probability $p(x|C_i)$ is called as likelihood which denotes the probability of feature x occurring in a given class C_i, n is the number of classes. Consequently, the posterior probabilities $p(C_i|x)$ which means the probability for a given feature x that is classified into a specific class i can be derived by basic Bayes theorem in equation 27. Most of the time, a single feature is not enough to discriminate the classes. Multiple features are a better choice to distinguish the classes in a high dimension. The Bayes theorem for multiple features can be expressed as equation 28 which is similar as equation 27 but replacing single feature x with a feature vector x including multiple features and the likelihood $p(C_i|x)$ is a joint conditional probability (for discrete case).

$$P(C_i|X) = \frac{p(X|C_i)p(C_i)}{p(X) = \sum_{j=1}^{n} p(X|C_j)p(C_j)} \tag{28}$$

For the pattern classifiers based on Bayesian decision theory, discriminant functions, which are represented as $g_i(x)$ while i=1,...,n denoting the ith class, are widely used. For a sample with multiple features X, when $g_i(X) > g_j(X)$

and $i \neq j$,the sample is classified into class C_i that is corresponding to the class with the highest posterior probability in the Bayes theorem. Thus, the discriminant functions can be achieved by the following equation.

$$g_i(X) = P(C_i|X) = \frac{p(X|C_i)p(C_i)}{p(X) = \sum_{j=1}^{n} p(X|C_j)p(C_j)} \tag{29}$$

Since $p(X)$will not affect the decision and can be viewed as constant, the denominator in Equation (29) can be eliminated. In order to simplify and make the discriminant function much easier to understand, the discriminant function can be written in a simpler form as follows by taking natural logarithm to the numerator in Equation (29):

$$g_i(X) = \ln p(X|C_i) + \ln p(C_i). \tag{30}$$

As a result, the discriminant function based on bayesian decision theory is decided by the conditional probabilities (likelihood) $p(X|C_i)$ and priori probabilities $p(C_i)$.In particular, when the multiple features satisfy with the multivariate normal distribution, the conditional probabilities can be described by multivariate normal density as follows[3].

$$p(X|C_i) = \frac{1}{(2\pi)^{d/2}\left|\sum i\right|^{1/2}} \exp\left[-\frac{1}{2}(X-\mu_i)^t\left(\sum\right)^{-1}(X-\mu_i)\right] \tag{31}$$

where X is a d-dimensional feature column vector, μ_i is the d-dimensional mean vector of the ith class, $\sum i$ is the d-by-d dimensional covariance matrix of the ith class, $\left|\sum i\right|$ and $\left(\sum\right)^{-1}$ are the determinant and inverse of covariance matrix respectively. Consequently, the discriminant fuction in Equation (30) can be easily evaluated as Equation (32) if the conditional probabilities are mixture gaussian distribution (replace $p(X|C_i)$ in Equation (30) with Equation (31)).

$$g_i(X) = -\frac{1}{2}(X-\mu_i)^t\left(\sum i\right)^{-1} - \frac{d}{2}ln\,2\pi - \frac{1}{2}ln\left|\sum i\right| + \ln p(C_i) \tag{32}$$

Thus, the features are classified into the class that can achieve the biggest discriminant value. The discriminant function derived from bayesian decision

theory is proven that can achieve minimum-error-rate among all of the classifiers [3, 59].

3.3.2 Leaving-One-Out Technique

It is evident that a classifier designed with as much training and testing sets as possible will be much more robust in terms of improving the performance of classifier and the accuracy for estimating its error rate. However, due to the restriction of available sample data, the accuracy for both training and testing in a classifier design will be limited. Leaving-one-out method is such kinds of technique that can avoid the previous drawback to a large extent since this approach can nearly double the effective size of the sample data [3]. The procedure of leaving-one-out technique is described as follows. Suppose n samples are given in the data set, the classifier obtained by leaving-one-out is not designed and investigated by simply dividing the samples into training and testing sets at one time but n times. In this process, one sample from the data set is withdraw for testing set and the other n-1 samples is used to design the classifier. Thus, this withheld sample can be tested by the designed classifier with n-1 samples. It makes sense because the classifier is designed without this sample. The previous step can be repeatedly processed with n times so that each time one different testing sample will be left out and totally n samples can be conducted as testing set. For each round, a new classifier will be established with n-1 samples and tested by the one sample that is not used in the design of classifier. Consequently, the expected probability of error can be deduced as k/n on an average classifier which is trained on the n-1 samples and k is the number of errors in the testing phase. Since the samples in this technique is avoided to be both training and testing for a given classifier, the estimate of error rate can be regarded as unbiased and it will be as accurate as possible since all of the samples are used for testing [98-99]. Finally, the

classifier is designed by using the total n samples as training and its expected error rate will be at least as low as k/n since this classifier is created with n samples but not n-1 samples which is used in the leaving-one-out step. This process is illustrated in Figure 13. Step 1 in Figure 13 is conducted n times until no new sample can be used as test. The classifier gi(x) is designed based on Bayesian decision algorithm. After the table showed in step 2 of Figure 13 is achieved, the misclassification rate can be measured. Finally, all of the samples are applied to design the classifier which will be used to predict the sample with unknown class.

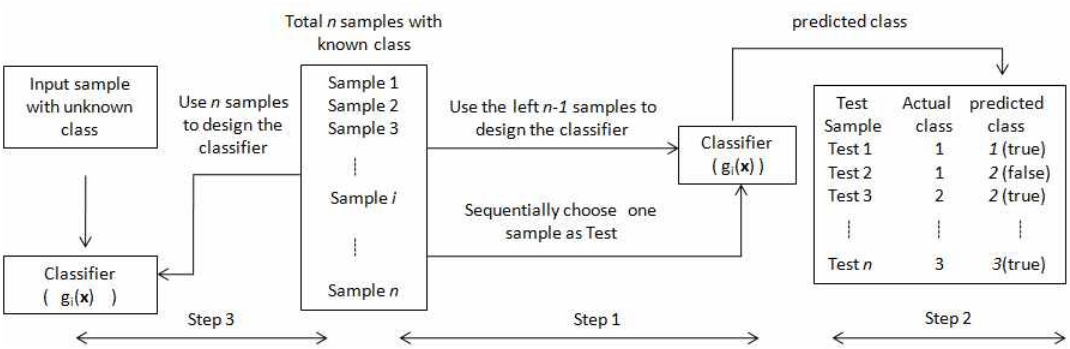

Fig. 13 Flowchart of leaving-one-out technique

3.3.3 Procedures of the Classifier Design

When the RBCs phase images are reconstructed by using computational numerical algorithm from the holograms obtained by off-axis digital holographic microscopy, each RBC is extracted with the background removed by marker-controlled watershed transform segmentation approach [37]. Then, ten features showed in table 3 are calculated from each whole segmented RBC. In addition, in order to increase the performance for separating the RBC groups, four more features including projected surface area, perimeter, average phase value and elongation are measured from the inside part of segmented RBCs which is also presented in Table 3. The whole segmented and inside part of

RBC is illustrated in Figure 14.

Table. 3 Description of Total Fourteen Features

The whole segmented RBC	
Feature	Description
F1: projected surface area	Number of pixels within single RBC×one pixel area
F2: perimeter	The length of cell boundary
F3: circularity	(Perimeter×perimeter)/area
F4: average phase value	Average phase value for pixels with in single RBC
F5: mch	mean corpuscular hemoglobin
F6:mchsd	mch surface density
F7: phase of center pixel	phase value of center pixel (average 5×5 pixels)
F8: sphericity coefficient	Center part phase value/maximal phase value
F9:elongation	Orientation of chain code in the cell boundary
F10: D-value	Center pixel phase value minus maximal pixel phase value
Inside part of the segmented RBC	
F11: projected surface area	Number of pixels within inside part of RBC×one pixel area
F12: perimeter	The length of boundary in the inside part of cell
F13: average phase value	Average phase value for pixels with in inside part of RBC
F14:elongation	Orientation of chain code in the boundary of inside part of cell

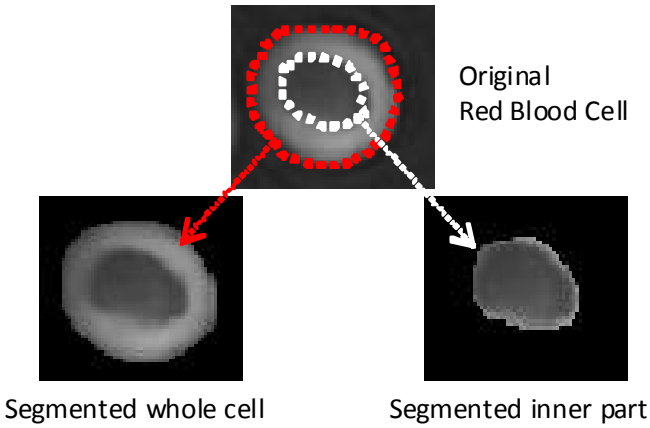

Fig. 14 Illustration of segmented whole and inside part of the cell.

The projected surface area, average phase value, mean corpuscular hemoglobin (MCH) and MCH surface density (MCHSD) are calculated from each whole segmented RBC as following equations respectively.

$$S = N\frac{p^2}{M^2} \tag{33}$$

$$\overline{\varphi} = \frac{1}{N}\sum_{i=1}^{N}\varphi_i \tag{34}$$

$$MCH = \frac{10\lambda}{2\pi\alpha}S\overline{\varphi} \tag{35}$$

$$MCHSD = \frac{MCH}{S} \tag{36}$$

where N is the number of pixels within a single RBC, p is the pixel size, M is the magnification of the digital holography microscopy, φ_i is the phase value at ith pixel within a single RBC, λ is the wavelength of the light source and α known as the specific refraction increment is a constant. When the boundary of each cell is marked by an 8-directional Freeman chain code [100], the features of perimeter, circularity and elongation can be achieved by equations as follows [100].

$$perimeter = N_e \times 1 + N_0 \times \sqrt{2}, \tag{37}$$

$$cirularity = perimeter^2 / S \tag{38}$$

$$elongation = \max(|N_{0,4} - N_{2,6}|, |N_{1,5} - N_{3,7}|), \tag{39}$$
$$where\ N_{j,k} = \sum_{\substack{i=1 \\ a_{i=j} \text{ or } a_{i=k}}}^{n} 1,$$

where N_e is the number of even valued elements while N_o is the number of odd element in the chain code of boundary in single RBC, n (=N_e+N_o)is total number of element in the Freeman chain code for each RBC. Also, the phase value of center pixel (pcp) is defined as the average phase value of the center 5×5 pixel, sphericity coefficient (sc) is the division between phase value of center pixel and maximal phase value within each whole segmented RBC and the D-value (dValue) is the difference between phase value in center pixel and maximal phase value. These features are defined as following equations.

$$pcp = \frac{1}{25} \sum_{-2 \le i \le 2} \sum_{-2 \le j \le 2} \varphi^{ij}, \tag{40}$$

$$sc = \frac{pcp}{\varphi_{\max}} \tag{41}$$

$$dValue = pcp - \varphi_{\max} \tag{42}$$

where φ^{ij} is the phase value at location (i,j) within a 5×5 window while (0,0) is the central location of the single RBC or inner part of RBC, $\varphi_{\max}$ is the maximal phase value within the analyzed single RBC or inner part of RBC.

For the measurement of four features in the inside part of RBC, the previous equations can be repeatedly used while only need to determine these features in the inside part instead of the whole segmented cell.

Here, the statistically method of Hotelling's T-square test [95] is applied to evaluate that the features calculated from the inside part of cell can indeed provide additional separation between each pair of RBC groups beyond the separation already achieved by the ten features obtained from the whole segmented cell. Let y denote the p×1 vector where p=10 here which include ten variables for measuring the features in the segmented cell and x denote the q×1 vector where q=4 that express the four variables for calculating the properties in the segmented inside part of cell. It is assumed that each pair of samples is

from multivariate normal populations and x1, x2 are two q×1 vectors while y1,, y2 are two p×1 vectors from two different groups. Then, the null hypothesis [H_0: x1 and x2 are redundant for separating the two classes beyond y1, and y2]can be represented as follows [95,97-98]:

$$T^2(x|y) = (v-p)\frac{T_{p+q}^2 - T_p^2}{v + T_p^2}, \tag{43}$$

which is distributed as $T_{q,v-p}^2$ where v=n_1+n_2-2 while n1,n2 are the number of samples in two groups respectively. When, $T^2(x|y) \geq T_{\alpha,q,v-p}^2$ the null hypothes is that x is redundancy would be rejected at significance level of α where the critical value of $T_{\alpha,q,v-p}^2$ can be achieved from the T^2-table with q and v-p degree of freedom. In Equation (43), T_{p+q}^2 and T_p^2 are expressed as following equations respectively [95].

$$T_{p+1}^2 = \frac{n_1 n_2}{n_1+n_2}\left[\begin{pmatrix}\overline{y_1}\\ \overline{x_1}\end{pmatrix} - \begin{pmatrix}\overline{y_2}\\ \overline{x_2}\end{pmatrix}\right]^T \begin{pmatrix}S_{yy} & S_{yx}\\ S_{xy} & S_{xx}\end{pmatrix}^{-1}\left[\begin{pmatrix}\overline{y_1}\\ \overline{x_1}\end{pmatrix} - \begin{pmatrix}\overline{y_2}\\ \overline{x_2}\end{pmatrix}\right], \tag{44}$$

$$T_p^2 = \frac{n_1 n_2}{n_1+n_2}(\overline{y_1} - \overline{y_2})^T S_{yy}^{-1}(\overline{y_1} - \overline{y_2}), \tag{45}$$

where $\overline{y_1}$ and $\overline{y_2}$ are the sample mean vectors, S_{yy},S_{yx} and S_{xx} are the covariance matrixes. In the experimental section, the T^2statistic test results among each pair of RBC groups are presented.

In order to demonstrate that 3D features of a RBC extracted from DHM imaging technique are beneficial to distinguish different kinds of RBCs, the RBC's features are divided into two categories that are given in Table. 4. One is defined as 2D features which can be acquired from 2D imaging system and the other is defined as 3D features which are obtained from DHM technique. Then, the Hotelling's T-square test as previous description for inner part feature analysis is conducted to check whether the 3D features can provide additional separation among RBCs classes beyond the partition already achieved by the 2D features. In this case, x in Equation (43) denotes the seven features from 2D features category and y represents the other seven features from 3D

features group.

Table. 4 Division of RBC features

2D Features	F1, F2, F3, F9, F11, F12, F14
3D Features	F4, F5, F6, F7, F8, F10, F13

Table. 5 Samples for training the classifier

RBCs with stomatocyte shape (Total samples: 87)	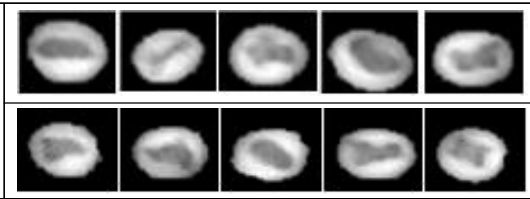
RBCs with discocyte shape (Total samples: 103)	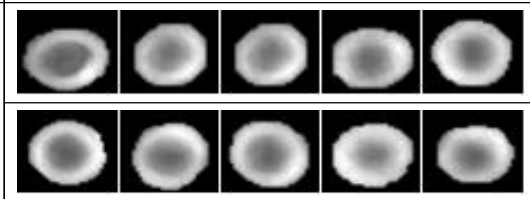
RBCs with echynocyte shape (Total samples: 106)	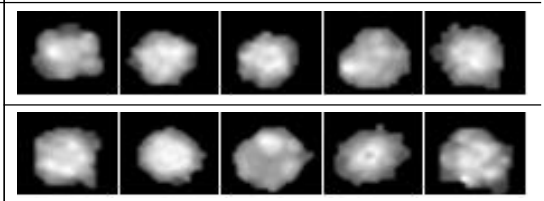

In our experiment, 87 RBCs labeled with stomatocyte shape, 103 RBCs labeled with discocyte shape and 106 RBCs labeled with echinocyte shape are extracted as samples. Also, the total fourteen features denoted by feature vector as $[X_1, X_2, \cdots, X_{14}]$ in each single RBC are calculated. What calls for special attention is that when there are no inside part for some RBCs, a random value from standard normal distribution will be assigned to the features from F11 to F14 in Table 3. Samples with known class which will be used to design the classifier are showed in Table 5.

After all of the fourteen properties are determined from the samples, the PCA algorithm is applied to these features so as to reduce the variables dimension

and the 60% principal components that is 8 components are retained for the classifier design in the next step. Consequently, the original data can be projected onto an eight dimension space by using the 8 principal components. Here, it is assumed that the all of the obtained data satisfy with the multivariate normal distribution. Accordingly, the joint density (conditional probability in Equation (28)) of the multiple features for each type of RBCs can be represented by mixture Gaussian density as expressed in Equation (31) with features after being projected from the eight principle components. Furthermore, It can assume that the priori probabilities ($p(C_i)$ in Equation (32)) for each class are equal so that this term can be removed from the discriminant function as well as the constant term $0.5d\ln 2\pi$ since they do not affect the pattern classification in this case. Therefore, the discriminant function in Equation (32) based on Bayesian decision theory can be further simplified as follows:

$$g_i(x) = -\frac{1}{2}(x-\mu_i)^T\left(\sum i\right)^{-1}(x-\mu_i) - \frac{1}{2}ln\left|\sum i\right|,\ 1 \le i \le 3 \tag{46}$$

where μ_i and $\sum i$ are estimated from respective sample data by using unbiased estimator [97]. As a consequence, one type of RBCs is corresponding to one discriminant function and three dicriminant functions are needed for the classification of three classes of RBCs (Class 1: stomatocyte shape RBCs, Class 2: discocyte shape RBCs, Class 3: echinocyte shape RBCs). The testing pattern will be categorized into the class which can achieve the biggest value by the corresponding discriminant function. Considering the situation that there are other types of RBCs excepting the three typical kinds of RBCs, the fourth class, which includes all types of RBCs excluding these three classical classes, is defined. When the probability of one sample belonging to any one of the three typical types of RBCs is low, it will be grouped into the fourth class. This can be achieved by Equation. (31) since the discriminant function in Equation. (29) is proportional to the value of likelihood (Equation.(31)) when the priori probability is assumed to be the same for all types of RBCs. In this paper, when the density in the likelihood (Equation. (31)) for the extracted

features from a RBC is less than 0.001 among all of the three typical types of RBCs, the corresponding RBC will be classified into the fourth class. The flowchart for our classifier design and RBCs classification is presented in Figure 15.

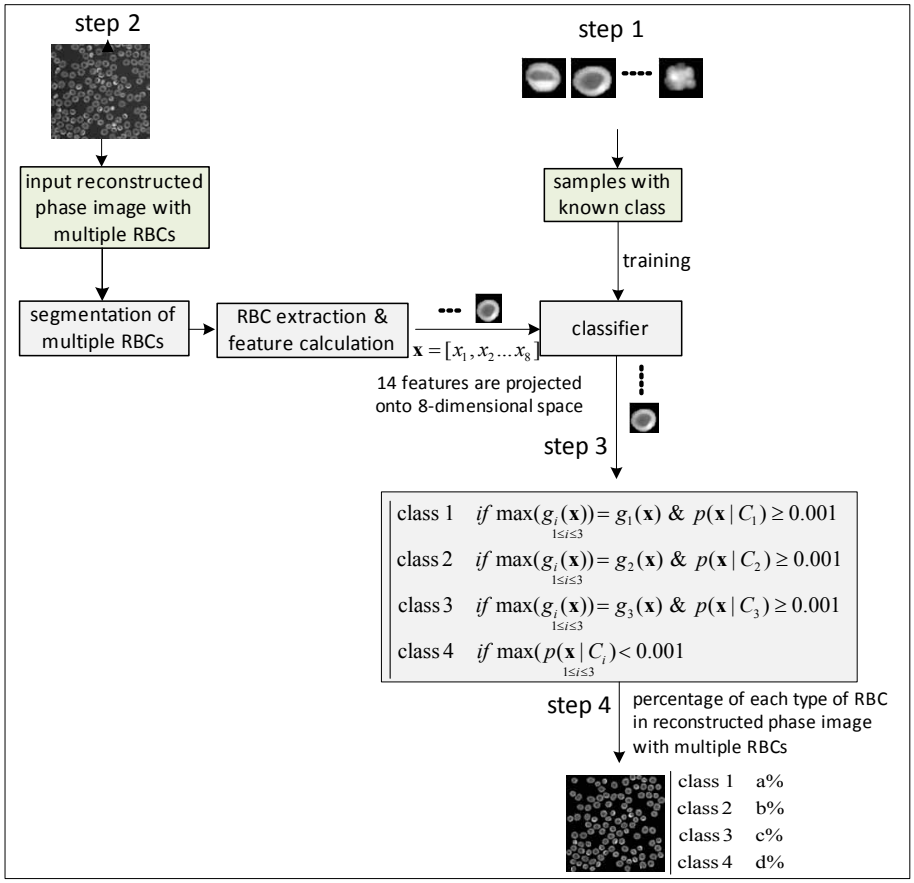

Fig. 15 Flowchart of RBCs classification.

Firstly, the classifier will be designed based on the Bayesian design theory by the leaving-one-out technique with the samples of known class (step 1 in Figure 15). Then, the obtained classifier is used to classify the RBCs in a reconstructed phase image with multiple RBCs (step 2 in Figure 15). In this step, the original RBCs phase image and the inside part of the RBC has to be segmented so as to extract all of the RBC and calculate the corresponding

features.

After that, all of the RBCs in the reconstructed RBCs phase image are grouped into one of the four types of RBCs as described in Figure 15. Finally, the percentage of different kinds of RBCs in the RBCs phase image can be calculated and analyzed (step 4 in Figure 15). Especially, when the occupation ratio of the fourth class achieves a highest value in a reconstructed RBCs phase image, this image should be examined carefully in further since this situation is not normal for a normal person. The leaving-one-out technique for improving the design of classifier and estimating the error rate is implemented by the pseudo-code showed in Figure 16 (based on Matlab). For the final design of classifiers (Class 1 denoted as $g_1(x)$, Class 2 denoted as $g_2(x)$ and Class 3 denoted as $g_2(x)$),all of the sample data are used as training set.

Step 1:	samples preparation (87 RBCs with stomatocyte shape, 103 RBCs with discocyte shape, 106 RBCs with echinocyte shape)
Step 2:	feature calculation (measure features from F1 to F14 for each RBC)
Step 3:	conduct principle component analysis (PCA) and derive new data with the main eight components.
Step 4:	design the classifier with the discriminant function based on Bayesian decision theory by using leaving-one-out technique
Step 5:	measure the misclassification rate
Step 6:	design the classifier without leaving one out (using all of the samples)

Fig. 16 Pseudo-code for the leaving-one-out test.

3.3.4 Experimental Results

The RBCs of healthy laboratory personnel were obtained through the Laboratoire Suisse d' Analyse Du Dopage--CHUV and stored at 4 °C during the storage period. The DHM measurements were performed several days after the blood was collected from the laboratory personnel. A total of 100-150 μl of

RBC stock solution were suspended in a HEPA buffer (15 mM HEPES pH 7.4, 130 mM NaCl, 5.4 mM KCl, 10 mM glucose, 1 mM Cacl2, 0.5 mM MgCl2, and 1 mg/ml bovine serum albumin) at 0.2% hematocrit for predominantly stomatocyte and discocyte shape RBCs while at a concentration of ~0.15% for predominantly echinocyte shape RBCs. A total of 4 μl of the erythrocyte suspension were diluted to 150 μl of the HEPA buffer and introduced into the experimental chamber, including two cover slips separated by spacers 1.2 mm thick. The cells were incubated for 30 min at a temperature of 37 °C before mounting the chamber on the DHM stage. All experiments were performed at room temperature (22 °C).

The simulation and measurement in this section are all executed on a 32-bit Windows 7 computer with a 3.30 GHz Intel Core i5-2500 CPU,4GB RAM, and 4 cores. The RBC phase images are reconstructed using the computational numerical algorithm from the holograms obtained by the off-axis DHM; then, the phase images are segmented by the watershed transform algorithm. Some of the reconstructed phase images, segmented RBCs, and the segmented inner part of the RBCs are shown in Figure 17 with the three typical types of RBC. After segmentation, all the 14 features are measured. Table 6 lists the quantitative validation for the extracted 14 features.

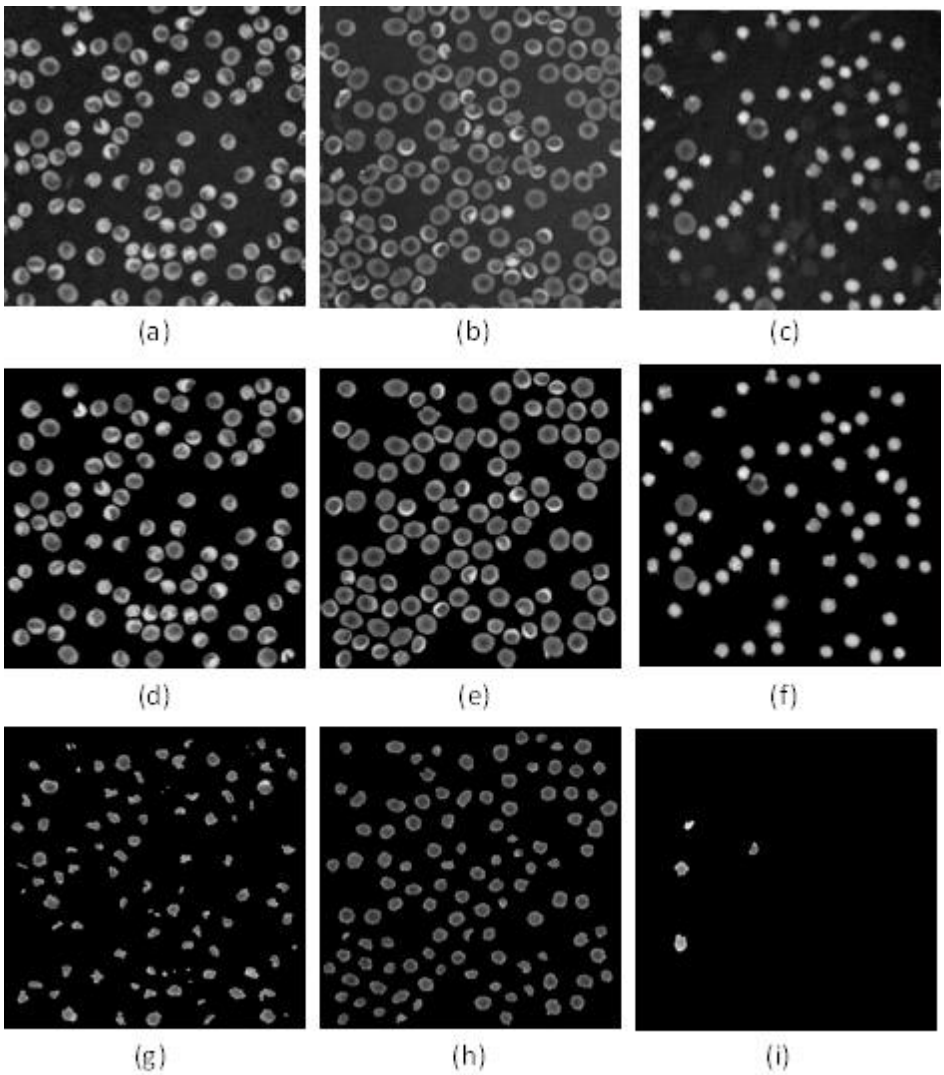

Fig. 17 Reconstructed RBC phase images and their segmented phase images. (a), (b), and (c) are reconstructed phase images for predominantly stomatocyte, discocyte, and echinocyte shape RBCs, respectively.(d),(e),and (f) are the corresponding segmented phase images from (a),(b),and (c). (g),(h),and (i) are the segmented inner part of the RBCs in (a),(b),and (c).

Table. 6 Quantitative validation of calculated 14 features from samples

Features	RBCs with stomatocyte shape (87 samples)		RBCs with discocyte shape (103 samples)		RBCs with echinocyte shape (106 samples)	
	Mean	Std	Mean	Std	Mean	Std
F1	34.31	3.83	47.28	5.40	25.76	3.96
F2	21.96	1.30	25.36	1.58	18.83	1.73
F3	14.13	0.44	13.67	0.37	13.84	0.93
F4	97.75	12.58	67.55	10.13	136.86	16.77
F5	31.60	4.12	30.10	5.01	33.04	4.29
F6	0.92	0.11	0.65	0.08	1.29	0.15
F7	84.35	28.21	26.84	14.41	207.70	37.73
F8	0.50	0.11	0.24	0.12	0.91	0.10
F9	7.73	5.32	8.38	5.73	6.12	4.75
F10	81.88	24.07	88.70	25.60	23.21	20.41
F11	9.83	3.36	20.50	4.43	0.01	0.93
F12	12.61	2.43	17.03	1.94	0.08	0.83
F13	81.50	11.65	56.72	7.72	0.10	0.97
F14	12.13	6.25	7.30	5.69	0.06	1.03

In this experiment, it has demonstrated that the features from the inner part of the RBCs are not redundant, but can contribute information to the separation of the RBC groups by Hotelling's T-square test. The calculated $T^2(x|y)$ value and critical value of $T^2_{\alpha,q,v-p}$ (see Section 3.3.3 for details) searched from the T^2- table are shown in Figure 18. It is noted that all the $T^2(x|y)$ values among each pair of RBC groups are larger than their corresponding critical value. Consequently, the null hypothesis H_0 when the features from the inner part of the RBCs are not significant in separating the RBC groups at the 0.05 level of significance is rejected. In other words, the features from the inner part of the RBCs can be helpful to classify the RBCs. Similarly, Statistical analysis results shown in Figure 19 reveal that 3D features of a RBC extracted from DHM imaging system can contribute to separate the RBCs classes. Therefore,

the discrimination performance for counting normal shapes of RBCs can be improved by adding to the 3D features of a RBC to the 2D ones.

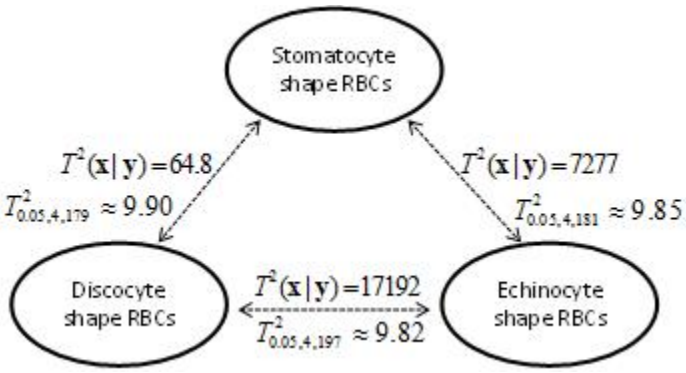

Fig. 18 Redundance analysis results for inner part features of RBCs with Hotelling's T-square test

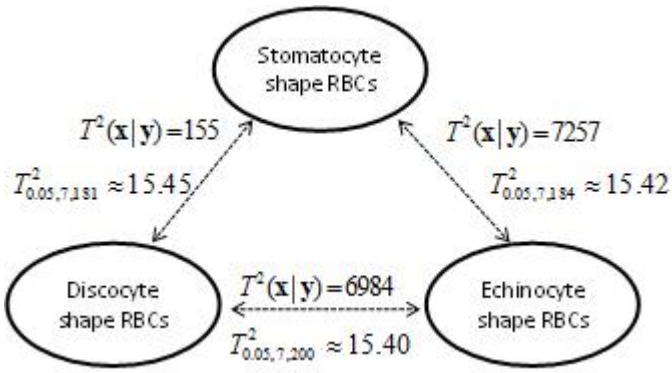

Fig. 19 Redundance analysis results for 3D features [see Table.4] of RBCs with Hotelling's T-square test

Next, the PCA algorithm is applied to the 14 features, and the 60% principal components (that is eight principal components) are retained to design the Bayesian-based classifier. Because it assumes that the multiple variables satisfy the multivariate Gaussian distribution, the mixture Gaussian density of each

group can be established by the features obtained from the multiplication of the original sample features with the extracted eight principal components. Therefore, the corresponding discriminant function can be realized with the created mixture Gaussian density for each RBC population as Equation (46). As the design presented in Figure 16, the leave-one-out experiment results show that the misclassification rate for the RBCs with stomatocyte shape is 3 / 87 = 3.45%, the misclassification rate for the RBCs with discocyte shape is 4 / 103 = 3.88%, and the misclassification rate for the RBCs with echinocyte shape is 3 / 106 = 2.83%. On the contrary, the misclassification rates for RBCs with stomatocyte, discocyte and echinocyte shape by only using 2D features (see Table.4) are measured to be 11/87=12.64%, 13/103=12.62 and 6/106=5.66% respectively. It is noted that the classifier based on the Bayesian decision algorithm with both 2D and 3D features achieved a very good result for the classification of RBCs with three different shapes. These classification results and misclassification rate for the three types of RBC by using 2D and 3D features are shown in Table. 7. It demonstrates that the discrimination performance for classification of different types of RBCs can be enhanced by using 3D features of a RBC. Moreover, the throughput which is defined as the processed data per second in our method is measured to be 27.64Mb/s and the total computational time for training and testing process is calculated to be 0.0024 second by averaging simulation result of 20 times.

The results of analyzing the percentage of morphologically normal RBCs in the reconstructed phase images with multiple RBCs are also shown in Figure 20. Figures 18(a), (b), and (c) are the measured percentages of the typical normal shapes of RBCs in the reconstructed RBC phase images. It is visually found that the majority of RBCs in each RBCs phase image are consistent with the highest percentage rate for the corresponding image in Figure 20. These percentages are automatically derived from the classifier that is obtained by our classifier algorithm whose misclassification rates are demonstrated to be low. It is believed that the proposed classifier can be adopted to count automatically

the morphologically normal cells in multiple human RBCs. In addition, the classifier can be helpful for the analysis of RBC-related diseases because the occupation ratio of the different types of RBC is associated with certain types of diseases.

Table. 7 Classification Results of the three types of RBCs

Using Both 2D and 3D Features for RBC Classification					
Actual Group	Number of Observations	Predicted Group			Misclassification rate
		Stomatocyte RBC	Discocyte RBC	Echinocyte RBC	
Stomatocyte RBC	87	84	3	0	3.45%
Discocyte RBC	103	3	99	1	3.88%
Echinocyte RBC	106	3	0	103	2.83%
Using only 2D Features for RBC Classification					
Stomatocyte RBC	87	66	9	2	12.64%
Discocyte RBC	103	11	90	2	12.62%
Echinocyte RBC	106	5	1	100	5.66%

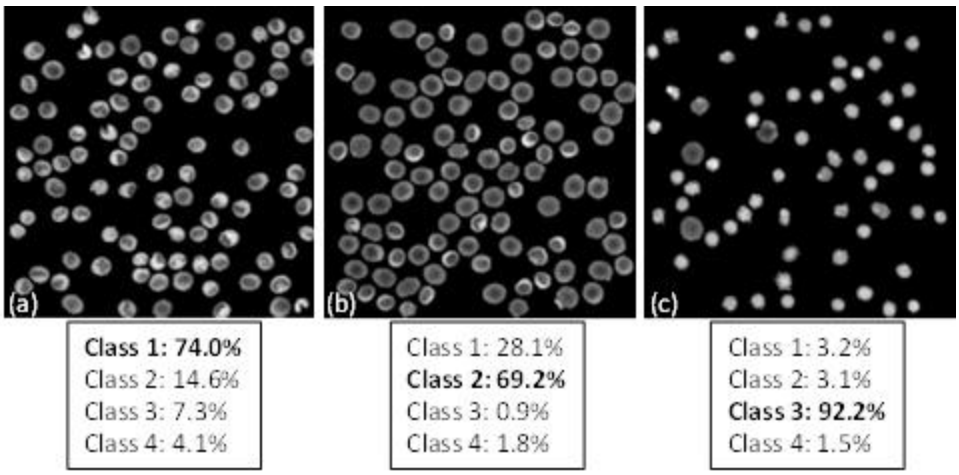

Fig. 20 Analysis of reconstructed phase image with multiple RBCs. (a), (b), and (c) are segmented images with percentages of each type of RBC labeled by our designed classifier method. (Class 1: RBCs with stomatocyte shape, Class 2: RBCs with discocyte shape, Class 3: RBCs with echinocyte shape, Class 4: other types of RBC).

3.3.5 Subsection Summaries

In this section, a classifier using DHM and Bayesian decision theory for automatic counting of the morphologically normal RBCs of stomatocyte, discocyte, and echinocyte shapes which allows us to quantitatively determine the percentage of normal cell shapes in multiple human RBCs is designed. The hologram patterns of the RBCs were first captured by the off-axis DHM, and the RBC phase images were reconstructed through the computational numerical algorithm. Ten patterns were calculated from each RBC that was extracted from the RBC phase images through the watershed transform segmentation method, and four more features were collected from the inner part of the RBC. Hotelling's T-square test showed that the features from the inner part of the RBC can significantly improve the separation of different RBC groups. In order

to reduce the dimension space of the variables, the PCA algorithm was adopted, and the first eight principal components were retained to retrieve new projected features to establish the mixture Gaussian densities for each type of RBC. Subsequently, the discriminant function based on Bayesian decision theory was used to design the classifiers. Finally, in order to improve the accuracy for estimating the error rate of the classifier, the leaving-one-out technique was used and tested. Experimental results demonstrated that our classifier can give a good performance for the classification of RBCs with stomatocyte, discocyte, and echinocyte shape. Their misclassification rates were at least as low as 3.45%, 3.88% and 2.83%, respectively. In addition, we demonstrate that the discrimination performance for RBCs classification can be improved by using both 2D and 3D features of a RBC. Furthermore, the designed classifier was able to group an RBC into a fourth class when the 2D and 3D features of the RBC are extremely different from the three typical types of RBC. This automatic RBC classification method can be extremely helpful for drug testing and for analyzing certain RBC-related diseases because the percentage of normal cell shapes in multiple human RBCs varies from disease to disease.

4. Automated Analysis of Three-dimensional Cardiomyocytes

Compounds tested during drug development may have adverse effects on the heart; therefore all new chemical entities have to undergo extensive preclinical assessment for cardiac liability. Conventional intensity-based imaging techniques are not robust enough to provide detailed information for cell structure and the captured images result in low-contrast, especially to cell with semi-transparent or transparent feature, which would affect the cell analysis. In this dissertation it is shown, for the first time, that digital holographic microscopy (DHM) integrated with information processing algorithms automatically provide dynamic quantitative phase profiles of beating cardiomyocytes. It is experimentally demonstrated that relevant parameters of cardiomyocytes can be obtained by our automated algorithm based on DHM phase signal analysis and used to characterize the physiological state of resting cardiomyocytes. Our study opens the possibility of automated quantitative analysis of cardiomyocyte dynamics suitable for further drug safety testing and compounds selection as a new paradigm in drug toxicity screens.

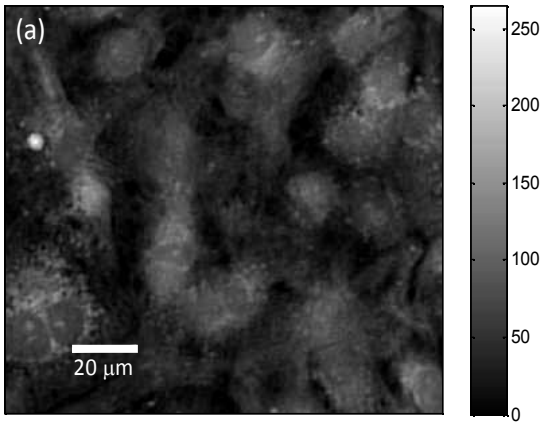

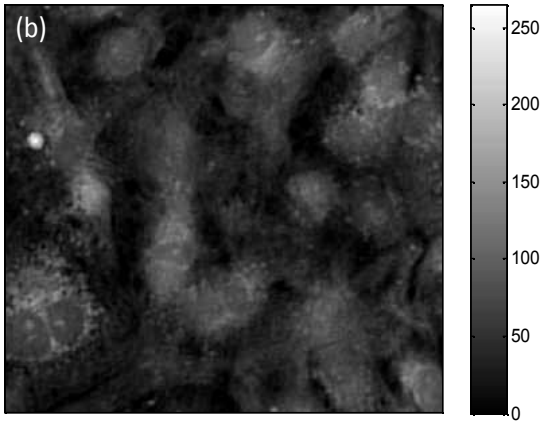

Fig. 21 Two optical path difference (OPD)[nm] images of cardiomyocytes captured at different time.(a) Frame #101 (b) Frame #102 (total 540 frames).

In the present work, the dynamic beating profile of cardiomyocytes obtained by DHM is analyzed using two proposed methods, either by monitoring the average or the variance information of imaged cells. The contraction and relaxation movement are also quantified by analyzing the difference between two successively acquired DHM quantitative phase images. From these experimental results, automated procedures are proposed for multiple parameters recording on cardiomyocytes dynamics imaged by DHM for a new methodology in drug toxicity screens. For the quantitative analysis of cardiomyocyte dynamics, the beating activity are calculated using two alternative methods, averaged optical path difference (OPD) images and variance of OPD images. The contraction and relaxation feature of cardiomyocyte were also measured using the proposed automated procedure. Figure 21 shows two OPD images of cardiomyocytes reconstructed from holograms.

4.1 Cell Culture and Imaging

iCell cardiomyocytes (human induced pluripotent stem (iPS) cell-derived cardiomyocytes) obtained for Cellular Dynamics Int. (Madison, WI) were culture according to the manufacturer's indication and grown for 14 days before recording. Measurements were achieved in a Chamlide WP incubator system for 96-well plate (LCI, South Korea) set at 37°/5% C02 with high humidity.

DHM images were acquired in an off-axis configuration on a commercially available DHM T-1001 from LynceeTec SA (Lausanne, Switzerland) equipped with a motorized xy stage (Märzhäuser Wetzlar GmbH & Co. KG, Wetzlar, Germany, ref. S429). Images were recorded using a Leica 20×/0.4 NA objective (Leica Microsystems GmbH, Wetzlar, Germany, ref. 11566049). Time-lapse images were acquired at 10 Hz for 1 minute.

4.2 Cardiomyocytes Beating Profile Measurement using Averaged OPD Images

The beating profile of cardiomyocytes was briefly calculated by thresholding the cardiomyocyte OPD images [see Figure 21] with a threshold value of 10% of the maximum OPD signal and then the thresholded images were averaged. 10% is an empirical value and is used to restrain the effect of noise. This process is described by the following equation:

$$\overline{opd}^{(i)} = average(opd\_thresh(x,y)^{(i)}), \tag{47}$$

$$with\ opd\_thresh(x,y)^{(i)} = \begin{matrix} opd(x,y)^{(i)} & \text{if } opd(x,y)^{(i)} \geq \max(opd(x,y)^{(i)} \times 0.10 \\ 0 & \text{if } opd(x,y)^{(i)} < \max(opd(x,y)^{(i)} \times 0.10 \end{matrix}$$

where $\overline{opd}^{(i)}$ is the average value of ith OPD image after thresholding, opd_ $opd\_thresh(x,y)^{(i)}$ is the OPD value at location of (x,y) on the ith threshodled

cardiomyocyte image, opd(x,y) is the OPD value at location of (x,y) for the ith cardiomyocyte image in optical path difference while 1≦x≦M, 1≦y≦N (M and N are the size of cardiomyocyte OPD image), $\max(opd(x,y))^{(i)}$ means the maximum value of ith cardiomyocyte image. One of the thresholded cardiomyocyte images obtained with this method is given in Figure 22. In addition, the beating profile with the capture time of cardiomyocytes resulted from this method is showed in Figure 23 including a small inset with a zoom on a single beating pattern. It is noted that the beating activity of cardiomyocytes is obvious (short peaks of high amplitude).

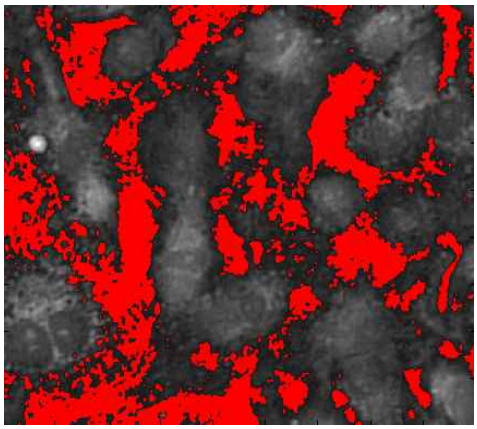

Fig. 22 Threshold cardiomyocyte image (red color denotes background after thresholding).

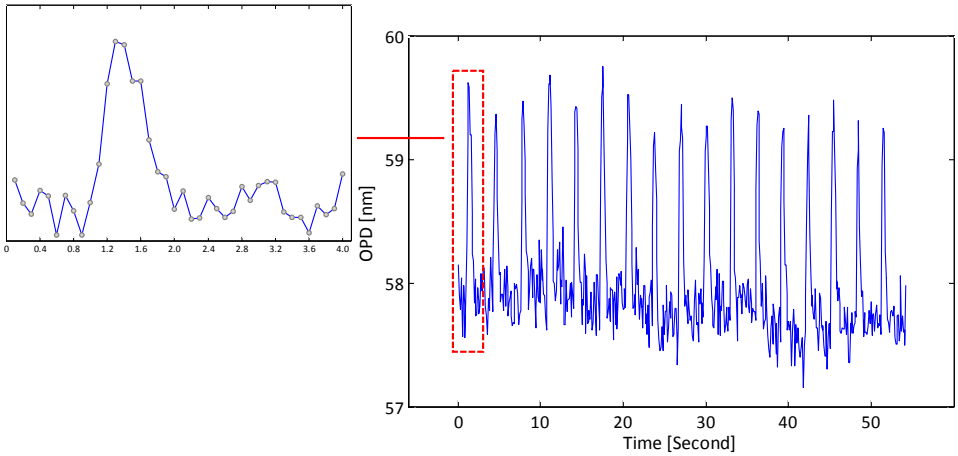

Fig. 23 Beating activity of cardiomyocyte (Inset shows a single beat).

After the segmentation, every single RBC can be extracted. Then, the RBC's properties such as Mean phase value, Area, Dry Mass and sphericity coefficient can be obtained. The following subsections are the definition of these properties used for RBCs analysis. Then, multiple parameters including amplitude, rising time, falling time, IBD50, IBD10, rising/falling slope, beating rate and beating period based on beating profile in Figure 23 were derived. These parameters are defined in Table 8 [101]:

In order to measure the above-defined parameters, peaks are detected by applying the first derivative technique to the original data curve in Figure 23 and finding locations where the first derivative values are zeros. The detected peaks based on cardiomyocytes beating profile are given in Figure 24(a).

Table. 8 Characteristic Parameters of Cardiomyocyte

Parameter	Definition
Amplitude	Value difference from each positive peak to the following negative peak (Amplitude=Ampmax - Ampmin)[see Fig. 25]
Rising time	The time elapsed from Amp20toAmp80(=T3-T1)[see Fig. 25]
Falling time	The time elapsed from Amp80toAmp20(=T6-T4)[see Fig. 25]
IBD50	The time elapsed for two points compose one Amp50(=T5-T2)[see Fig. 25]
IBD10	The time elapsed for two points compose on Amp10(=T7-T0)[see Fig. 25]
Rising/ Falling slope	The change of increased/decreased amplitude over the time course between Amp80andAmp20(=Amp80 - Amp20)[see Fig. 25]
Beating rate	The total number of positive/negative peaks in 1 minute (= total number of positive peaks/total time)
Beating period	The time between two adjacent positive and/or negative peaks (= the time of ith positive peak-the time of (i-1)th positive peak)
Frequency	The number of beating period per second (= total number of beating period/total time)

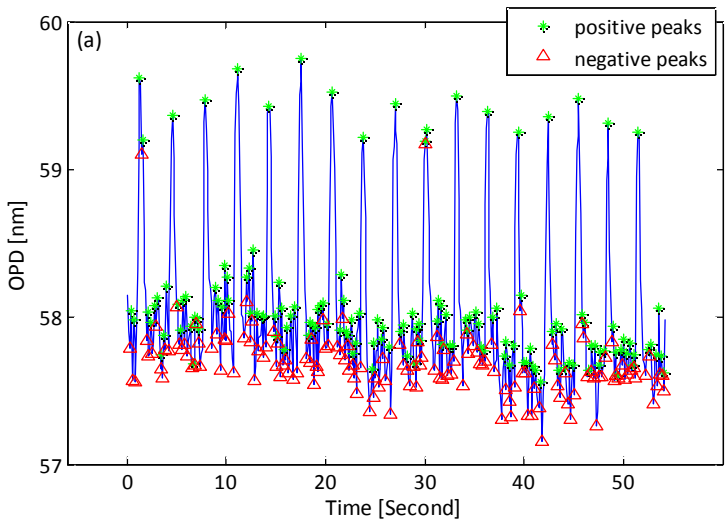

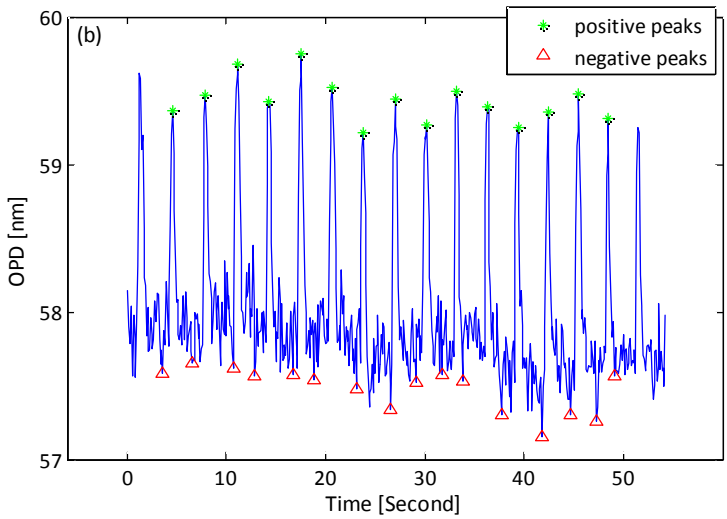

Fig. 24 Detected peaks in beating profile of cardiomyocytes. (a) Detected peaks on raw data. (b) Filtered peaks based on results of (a).

It can be noted from Figure 24(a) that many peaks including false peaks are detected. As a sorting process, positive peaks with values below a threshold and the negative peaks with values above a threshold are removed. This threshold can be automatically determined with Otsu's method [59] by using all of the positive peaks detected in Figure 24(a). In addition, the minimum negative peak between two neighbor positive peaks is extracted and then the maximum positive peak between two neighboring negative peaks is selected. This process reduces some inappropriate peaks and results in appropriate peaks for each beating period as shown in Figure 24(b).

Consequently, the beating profile between two adjacent negative peaks considered as one beating period is extracted [see Figure 25]. It is noted that the beating periods calculated between two negative peaks is approximately equal to that between two positive peaks. At the same time, the extracted beating profile for each beating period can be fitted with polynomials of degree 9 in a least-square criterion. The degree of 9 is reached by examining polynomials of up to degree 9 (up to degree 9 because data samples among

some beating profiles are around 10) for fitting the data based on the final fitting errors. The fitted polynomial with degree of 9 is described with the following equation:

$$f(x) = \sum_{i=1}^{10} a_i x^{10-i}, \tag{48}$$

where x represents the sample point on each beating period and ai which is the coefficient of polynomial are obtained with least-square criterion based on sample points. The average absolute error for each sample point (absolute error between actual and fitted point) is measured to be 0.1900. One of the fitting polynomial curves and the measured parameters are given in Figure 25.

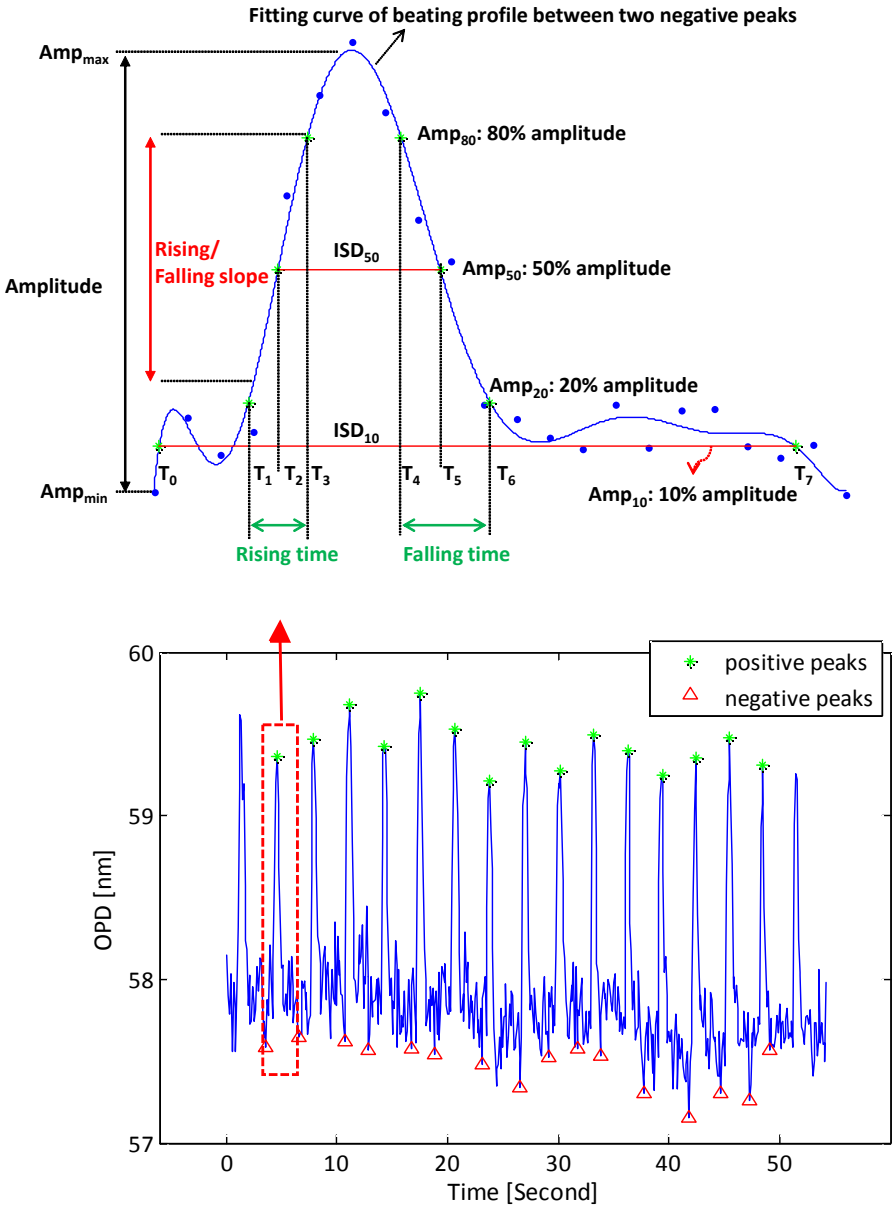

Fig. 25 Illustration of the fitted curves with parameters within one beating period on cardiomyocytes beating profile.

With the fitted polynomials curves, the amplitude value defined in Table 8 can be calculated as the maximum value minus the minimum value on the

fitted curve. Thus, the corresponding time [unit is second] in x axis for Amp10, Amp20, Amp50, Amp80 [see Figure 25] can be also be computed by solving the fitted polynomial equation. Then, all of the above mentioned parameters are measured for each individual beating period and a population average with coefficient of variation, (cv=standard deviation/average value, a parameter often used in high-throughput screening) is computed as shown in Table 9.

Table. 9 Measured Values of Multiple Parameters on Cardiomyocytes Beating Profile

Multi-parameter	Values (mean/cv)
1: Amplitude:	2.05/0.30
2: Rising time:	0.58/1.05 (seconds)
3: Falling time:	0.86/0.69 (seconds)
4: IBD50:	0.79/0.33 (seconds)
5: IBD10:	2.94/0.19 (seconds)
6: Rising/Falling slope:	1.19/0.30
7: Beating rate:	21.86/0
8: Beating period:	2.94/(sd=0.10 seconds)
9: Frequency	0.34/0

4.3 Cardiomyocytes Beating Profile Measurement using Variance of OPD Images

An alternative way to derive the beating profile of cardiomyocytes which is less sensitive to noise (originating from shot noise, speckle and contribution of out-of-focus structures), but requires more computer resources is to measure the variance of each OPD image after the temporal mean of the image stack is subtracted. This method is illustrated by Equation 49:

$$\delta_{opd}^{(i)} = variance\left[opd(x,y)^{(i)} - \overline{opd}_{temp}\right], \tag{49}$$

where opd(x,y)(i) is the ith OPD image, while 1≦x≦M and 1≦x,y≦N (M and N are the size of cardiomyocyte OPD image), $\delta_{opd}^{(i)}$ represents the variance of the ith cardiomyocyte image after temporal mean subtracted and $\overline{opd}_{temp}$ is the temporal mean which is calculated as the mean value of the image stack in the temporal dimension. The beating profile measured with this method is showed in Figure 26. Compared to the previous analysis method (Figure 24), this approach is more stable and less sensitive to noise (changes in the absolute value of the OPD signal).

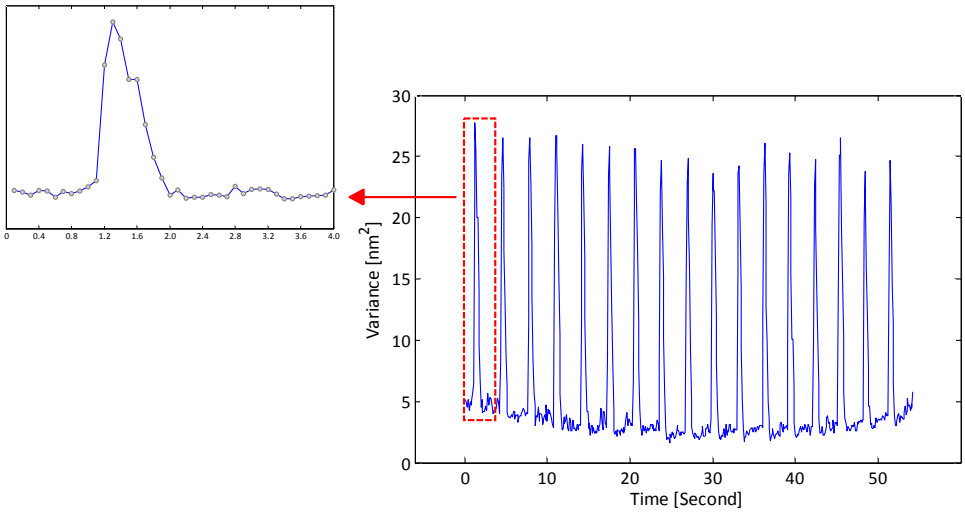

Fig. 26 Measured beating profile with variance information (inset shows a single beat)

Similar with the previous method, the peaks in Figure 26 can be detected using the first derivative property [see Figure 27(a)]. In addition, the positive and negative peaks are screened with a threshold value obtained by Otsu's method [30]. Consequently, the minimum negative peak between two neighboring positive peaks and the maximum positive peak between two neighboring negative peaks are selected [see Figure 27(b)].

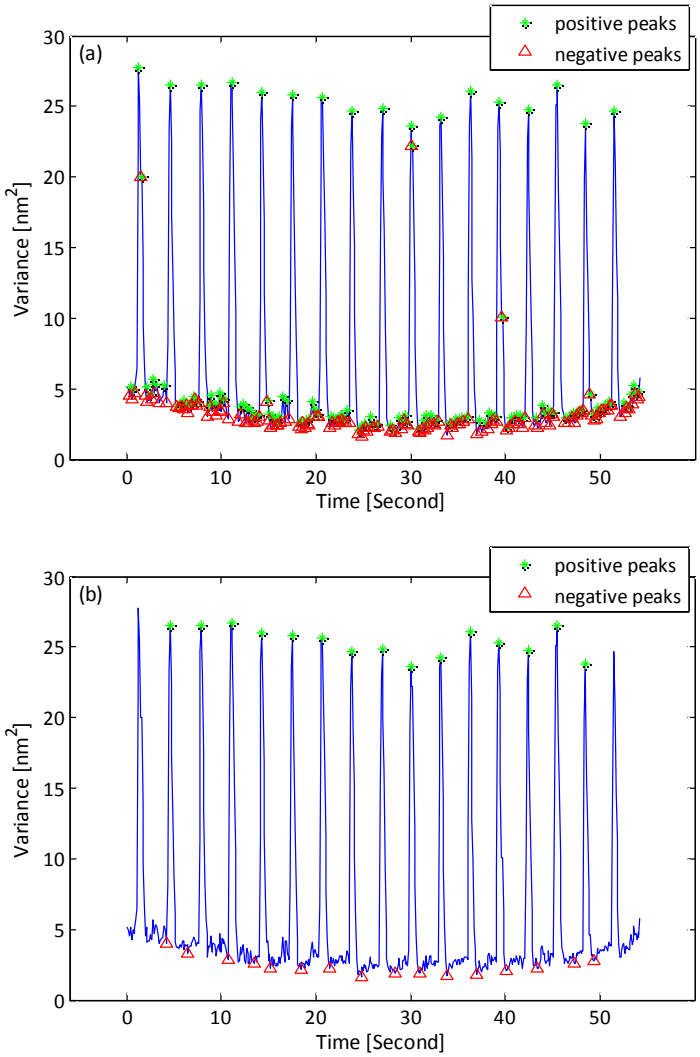

Fig. 27 Detected peaks on cardiomyocyte beating profile. (a) Detected multiple peaks. (b) Detected multiple peaks with some false peaks removed.

The beating profile within one beating period (between two negative peaks) can be individually extracted and is fitted with polynomial equation of degree 9 in a least-square error sense as that in Figure 25. The average absolute error for each sample point is measured to be 2.0359. Consequently, the same parameters as in the previous method can be measured and the corresponding

mean and coefficient of variation (cv) are given in Table 10. The measured parameters are in excellent agreement with the literature [102].

Table. 10 Measured Multiple Parameters on Cardiomyocytes Beating Profile

Multi-parameter	Values (mean/cv)
1: Amplitude:	23.06/0.17
2: Rising time:	0.45/0.98 (seconds)
3: Falling time:	0.26/1.04 (seconds)
4: IBD50:	0.66/0.23 (seconds)
5: IBD10:	2.30/0.25(seconds)
6: Rising/Falling slope:	13.83/0.17
7: Beating rate:	21.91/0
8: Beating period:	2.93/(sd=0.10)
9: Frequency	0.34/0

4.4 Cardiomyocytes Contraction and Relaxation Measurement

In order to observe the contraction and relaxation feature of cardiomyocyte, each captured image in the temporal stack is subtracted from the following one and then the spatial variance of the OPD is measured thus quantifying the amount of spatial displacement between successive frames (the cells used here are the same as those showed in Figure 21). The resulting image contains cardiomyocytes contraction and relaxation information (both indicated by an increase in the temporal variance signal). Two of the subtracted images are shown in Figure 28 where Figure 28(a) and 26(b) are different images at the minimum and maximum of a beat, respectively. The beating profile with contraction and relaxation information of cardiomyocyte is given in Figure 29(a), where one higher peak is for contraction and the neighboring lower peak is for relaxation. Then, the peaks can be detected with the first derivative criterion

(locations where the first derivative values are zeros). Similarly, positive peaks for contraction can be properly extracted with Otsu's thresholding algorithm by using all of the detected positive peaks. Next, a maximum peak between two neighboring contraction peaks is chosen as a positive peak for relaxation. Consequently, the inappropriate peaks can be removed. The resulted curves from Figure 29(a) with peaks indicated are given in Figure 29(b).

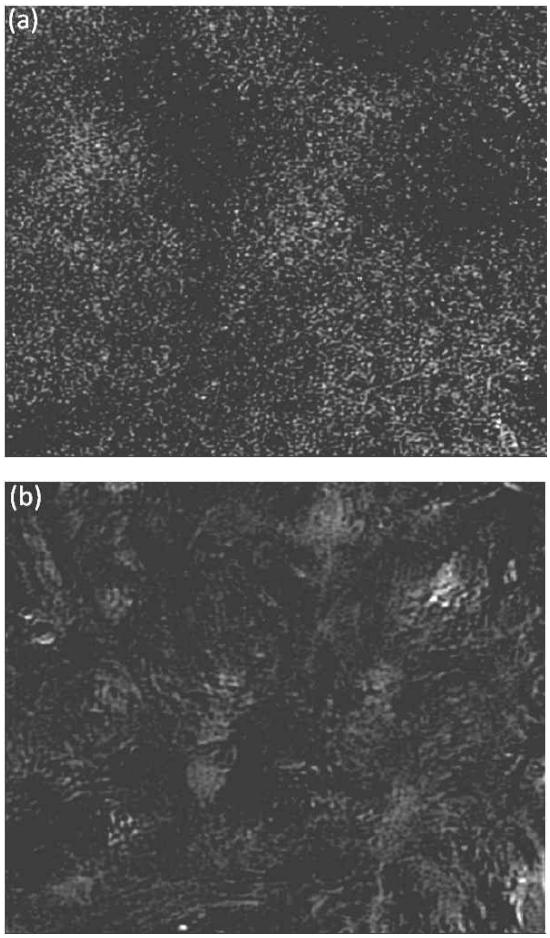

Fig. 28 Illustration of the difference images. (a) different image at the minimum of a beat (b) different image at the maximum of a beat.

Finally, the beating rate, beating period and frequency for cardiomyocytes

contraction and relaxation can be measured based on the detected positive peaks that include contraction and relaxation peaks. In addition, the time between the cardiomyocytes contraction and the following relaxation can be also calculated with the detected peaks in Fig. 27(b). These measured data are given in Table 11.

Table. 11 Measured Multiple Parameters on Cardiomyocyte Contraction and Relaxation Curve

Multi-parameters		Values (mean/cv)
Contraction	Beating rate:	23.14/0
	Beating period:	2.94/0.03
	Frequency	0.36/0
Relaxation	Beating rate:	23.14/0
	Beating period:	3.06/0.16
	Frequency	0.36/0
Time between contraction and the following relaxation		0.41/0.14

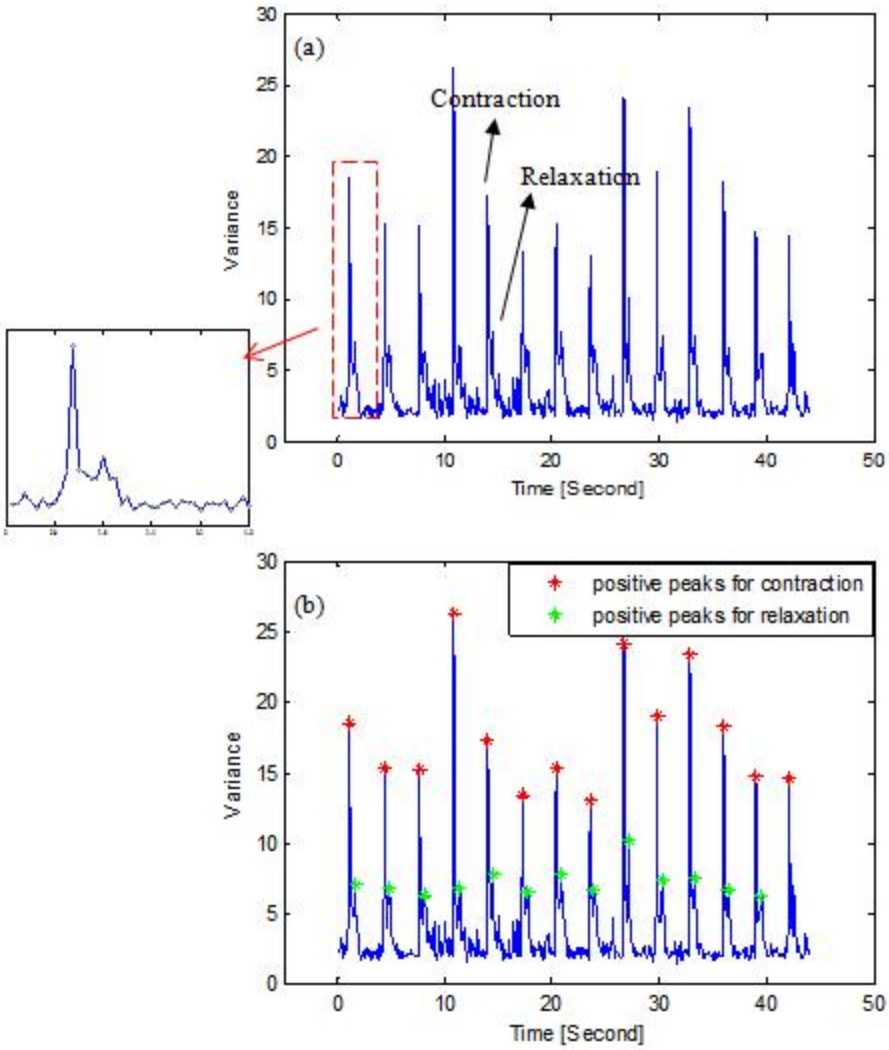

Fig. 29 Cardiomyocytes beating profile with contraction and relaxation information. (a) raw data of cardiomyocytes beating profile. (b) cardiomyocytes beating profile with contraction and relaxation peaks indicated. (inset shows a single beat with contraction and relaxation peaks)

4.5 Discussions and Section Summaries

In this paper, for the first time, human cardiac muscle cells' dynamics and

their spontaneous beating rates are quantitatively explored through the fusion of digital holography microscopy and information processing algorithms.

Experimental demonstrations have been provided for this new concept on multiple parameters recording on cardiomyocytes dynamics. From the experiments in the cardiomyocytes beating profile measurement using averaged OPD images and variance of OPD Images reported in Figure 25, Figure 27, Table 9 and Table 10, it is assured that interesting parameters of cardiomyocytes dynamics can be automatically measured. In addition, statistical parameters such as mean and coefficient of variation on the cardiomyocyte characteristics can be estimated. Four more cardiomyocyte image sequences were analyzed in order to show the generality of the proposed methods.

Among these image sequences, one of them is acquired with difficult conditions which mean having severe disturbance (a few out-of-focus debris are flowing through the field of view during the acquisition) while the other sequences are comparable inquality to the one presented previously.Four image sequences with peaks detected using the first (Section 4.2),second (Section 4.3) and third (Section 4.4) methods are given in Figure 30, Figure 31 and Figure 32 respectively where Figure 30 (a), Figure 31 (a) and Figure 32 (a) are from image sequences under tough/difficult conditions. It should be noted from these figures that our proposed method can detect all of the peaks, even in image sequences with debris interference. However, we found that the first method generated many noisy peaks in difficult conditions (1st image sequence) which makes the parameter measurement not accurate. On the other hand, the second and third methods are more stable to analyze these image sequences even those obtained under difficult conditions. Consequently, all of the needed multi-parameters can be measured based on these images, therefore proving the robustness of the analysis algorithm.

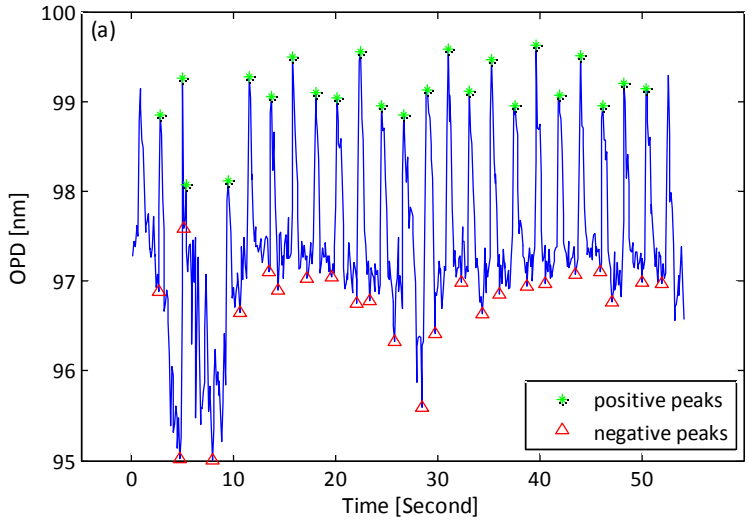

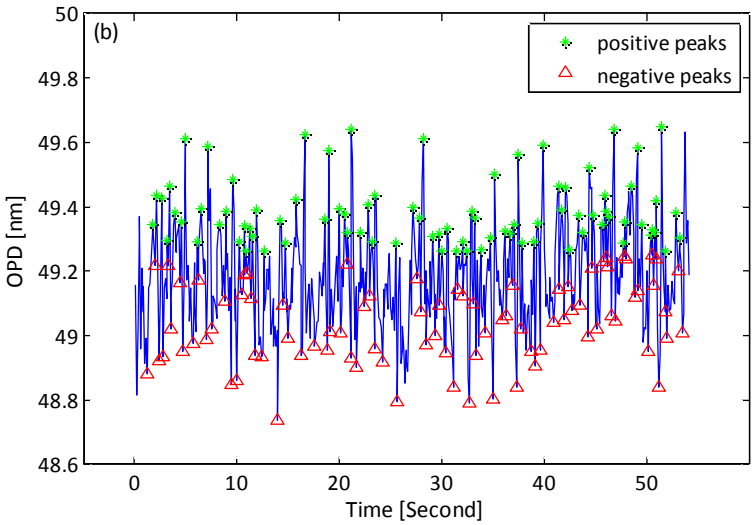

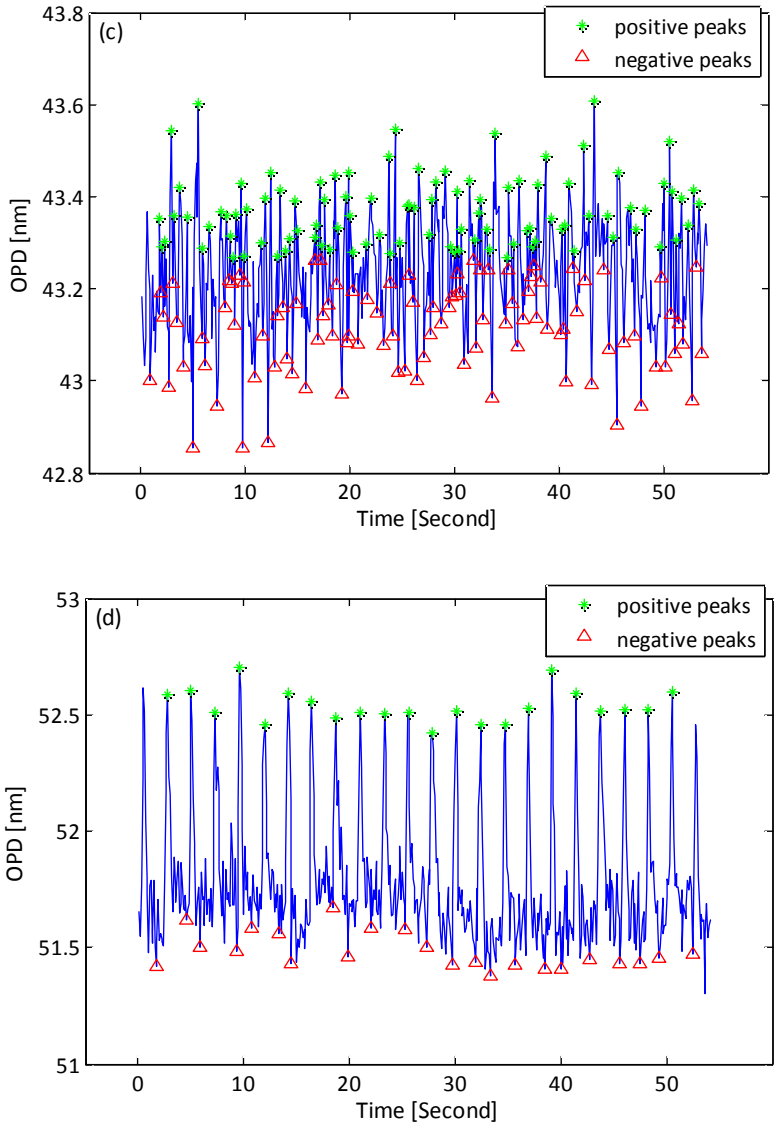

Fig. 30 Detected peaks based on four more cardiomyocyte sequences with the method in the Section 4.2. (a) cardiomyocyte image sequences acquired with difficult conditions. (b), (c), and (d) "noise-free" recordings (i.e. no debris interfering with the measurement) similar to the previous recording.

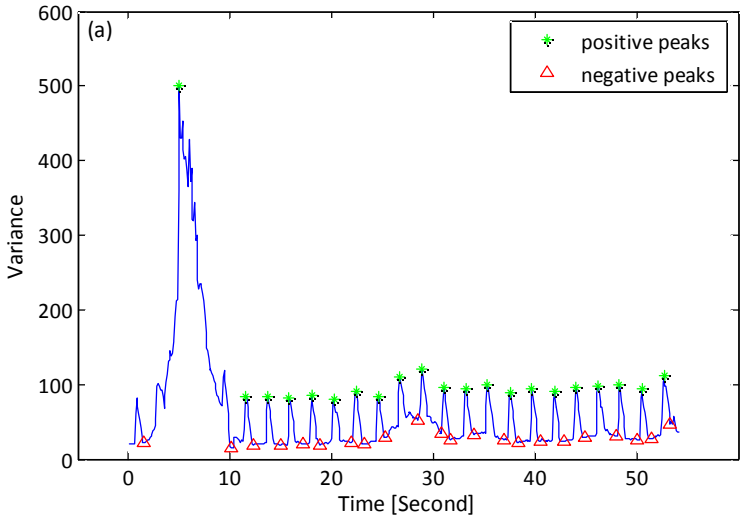

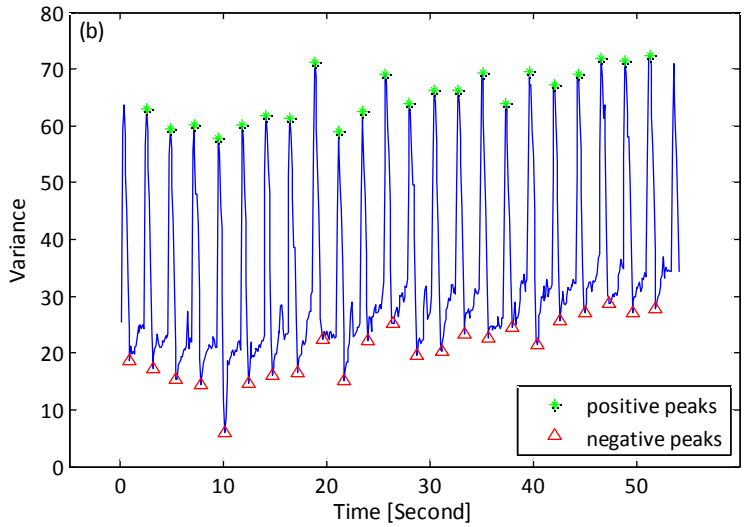

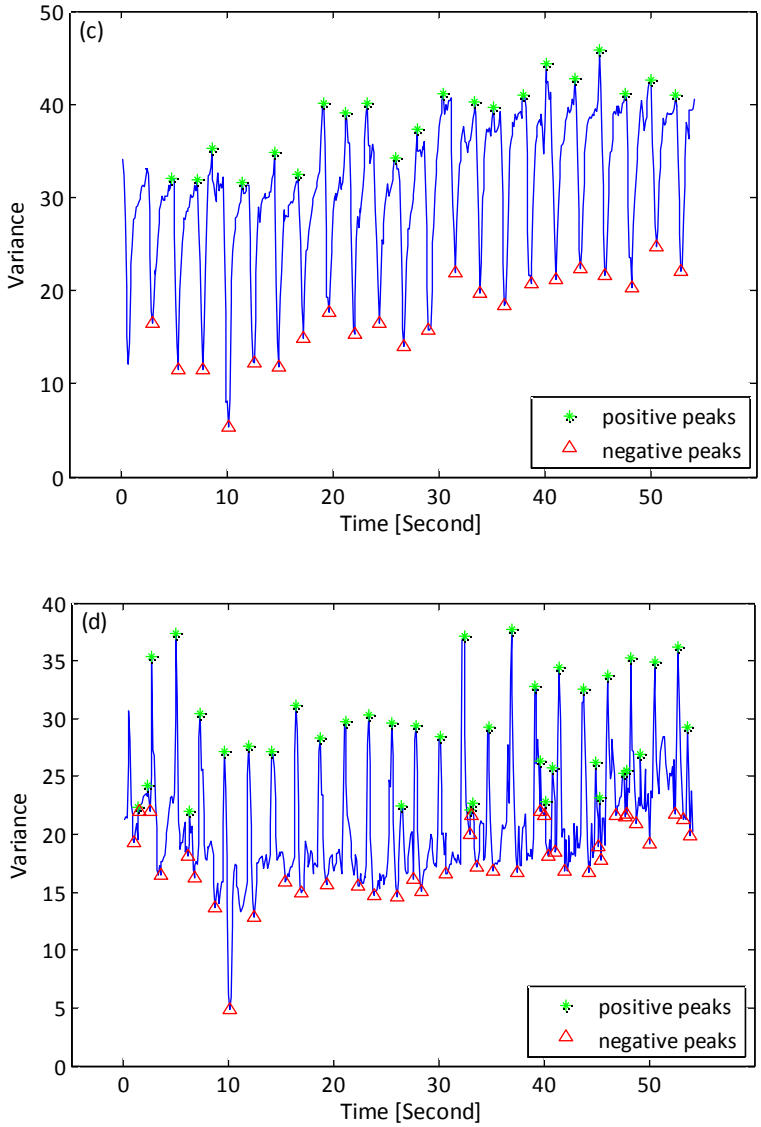

Fig. 31 Detected peaks based on four more cardiomyocyte sequences with the method in the Section 4.3. (a) cardiomyocyte image sequences acquired with difficult conditions. (b), (c), and (d) "noise-free" recordings (i.e. no debris interfering with the measurement) similar to the previous recording.

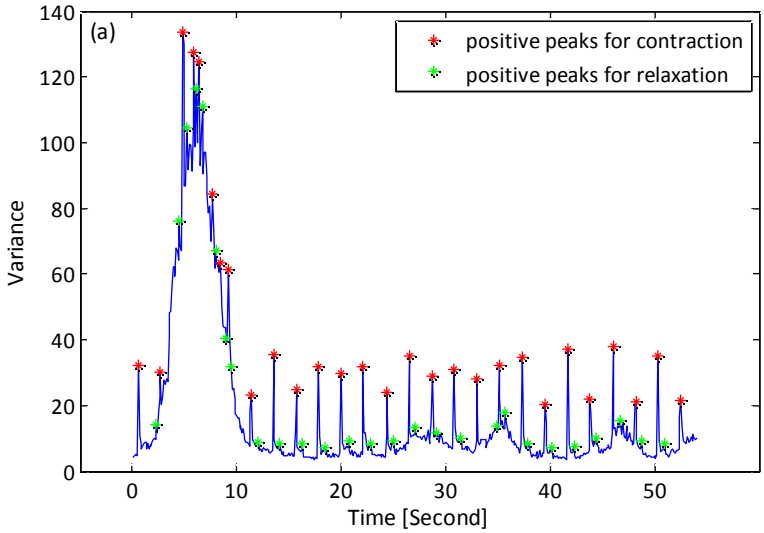

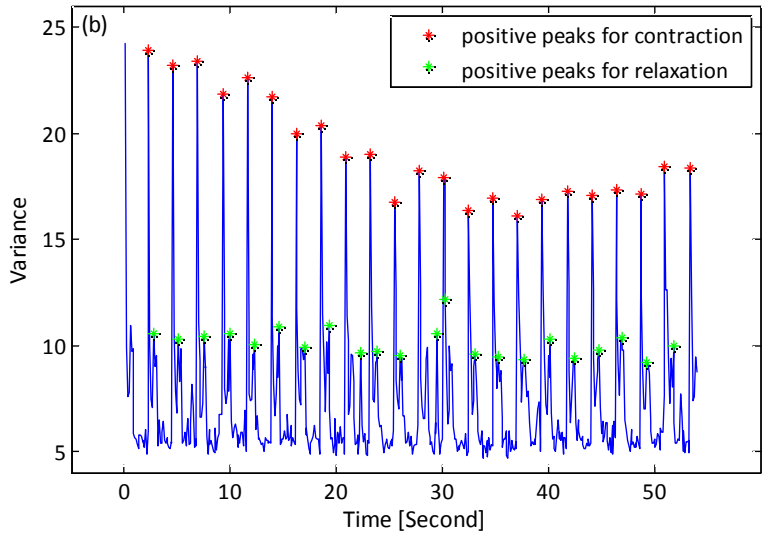

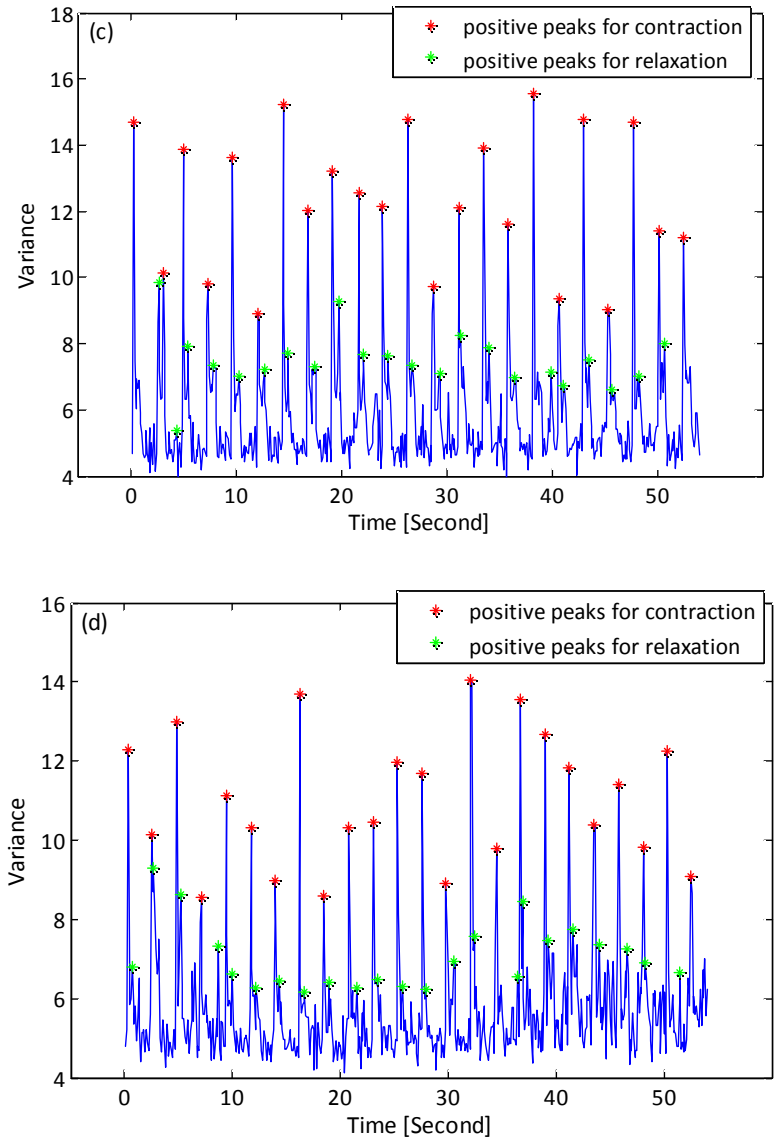

Fig. 32 Detected peaks based on four more cardiomyocyte sequences with the method in the Section 4.4. (a) cardiomyocyte image sequences acquired with difficult conditions. (b), (c), and (d) "noise-free" recordings (i.e. no debris interfering with the measurement) similar to the previous recording

Finally, the mean value of each of the parameter described in the first

(Section 4. 2), second (Section 4. 3) and third (Section 4. 4) methods is measured based on all the five sequences used previously. The measured mean values for the three methods are given in Table 12, Table 13, and Table 14, respectively.

Table. 12 Measured Multiple Parameters on Cardiomyocytes Beating Profile on Five Sequences with the First Method

Multi-parameter	Values (mean/cv)
1: Amplitude:	0.85/1.50
2: Rising time:	0.62/1.37 (seconds)
3: Falling time:	0.85/0.99 (seconds)
4: IBD50:	0.44/0.50 (seconds)
5: IBD10:	2.44/0.45 (seconds)
6: Rising/Falling slope:	0.51/1.52
7: Beating rate:	71.14/0.81
8: Beating period:	0.95/ (sd=0.84 seconds)
9: Frequency	1.16/0.83

Table. 13 Measured Multiple Parameters on Cardiomyocytes Beating Profile on Five Sequences with the Second Method

Multi-parameter	Values (mean/cv)
1: Amplitude:	40.01/1.21
2: Rising time:	0.57/0.86 (seconds)
3: Falling time:	0.43/1.13 (seconds)
4: IBD50:	0.79/0.65 (seconds)
5: IBD10:	2.35/0.38(seconds)
6: Rising/Falling slope:	24.00/1.21
7: Beating rate:	34.48/0.36
8: Beating period:	1.98/(sd=0.83)
9: Frequency	0.55/0.37

Table. 14 Measured Multiple Parameters on Cardiomyocytes Contraction and Relaxation Curve on Five Sequences

Multi-parameters		Values (mean/cv)
Contraction	Beating rate:	31.31/0.17
	Beating period:	2.20/0.19
	Frequency	0.49/0.17
Relaxation	Beating rate:	31.31/0.17
	Beating period:	2.23/0.31
	Frequency	0.49/0.17
Time between contraction and the following relaxation		0.59/0.62

The combined measurements show the robustness of the proposed algorithm and how they allows quantify important cardiomyocyte dynamic parameters that can be used to screen compounds cytotoxic effects. The beating profile contains more information than that is obtained by electrophysiology or fluorescence imaging as it integrates the effect of all the ion-channel involved and thus offer a signature that can be used to predict the effect of specific compounds. For instance inhibitors of hERG channel (the main class of channels assessed in cardio safety, which are involved in repolarization current) all results in a similar profile.In addition, due to the non-invasive aspect of the measurements, both short-term and long-term effects of the monitored compounds can be assessed with DHM.

The suitability of DHM is demonstrated for monitoring and quantifying the beating function of cardiomyocytes and automatically measuring multiple parameters of cardiomyocytes based on the quantitative phase profiles acquired with DHM. The proposed method can be rapid, noninvasive and effective and allows for automated analysis between normal cardiomyocyte dynamics and all other abnormal activities. It is believed that our automated non-invasive measurement procedures can open new perspectives for cardiotoxicological screening or profiling of candidate molecules in preclinical drug discovery and safety testing programs.

5. Conclusions

In this dissertation, a three dimensional imaging technique which is digital holographic microscopy has been applied to visualize human red blood cells and cardiomyocytes. The digital holographic microscopy has advantages of low cost, easy configuration, non-destruction, and fast imaging. Compared with conventional two dimensional imaging approaches, digital holographic microscopy is robust to sense semitransparent or transparent microorganism. The reconstructed image from holograms obtained by digital holographic microscopy with numerical reconstruction algorithm can provide rich three dimensional information such as the optical thickness of biological cells in live and dynamic conditions, which are helpful for the quantitative analysis of three-dimensional cells. Two kinds of transparent cells which are red blood cells and cardiomyocytes are imaged with digital holographic microscopy and the reconstructed images are automatically analyzed. For the analysis of three-dimensional red blood cells, the reconstructed phase images are segmented with marker-controlled watershed transform algorithm and the corresponding red blood cells features are measured. The modifications of three-dimensional morphology and mean hemoglobin of red blood cells induced by the length of storage time are also studied. This analysis is beneficial to the understanding of the features of RBCs with different storage periods and evaluation of any modifications in the 3D cell morphology and hemoglobin content. Moreover, a classifier using Bayesian decision theory for automatic counting of the morphologically normal RBCs of stomatocyte, discocyte, and echinocyte shapes which allows us to quantitatively determine the percentage of normal cell shapes in multiple RBCs has been designed. This proposed method is favorable to the analysis of RBC-related diseases. In addition, it is shown that the discrimination performance for counting of normal shapes of RBCs can be improved by using 3D features of a RBC. For the analysis of 3D

cardiomyocytes, the dynamic beating profile of cardiomyocytes obtained by digital holographic microscopy is investigated using two proposed methods, either by monitoring the average or the variance information of imaged cells. The contraction and relaxation movement are also quantified by analyzing the difference between two successively acquired digital holographic microscopy quantitative phase images. From the experimental results, automated procedures for multiple parameters recording on cardiomyocytes dynamics imaged by digital holographic microscopy for a new methodology in drug toxicity screens is proposed. It is shown, for the first time, that digital holographic microscopy integrated with information processing algorithms can automatically provide dynamic quantitative phase profiles of beating cardiomyocytes. Our study opens the possibility of automated quantitative analysis of red blood cells and cardiomyocyte dynamics suitable for further drug safety testing and compounds selection as a new paradigm in drug toxicity screens.

REFERENCES

[1] K. Onda and F. Arai, "Robotic approach to multi-beam optical tweezers with computer generated hologram," in IEEE Conf. ICRA, 1825-1830, 2011.

[2] I. Moon, M. Daneshpanah, B. Javidi, A. Stern, "Automated three-dimensional identification and tracking of micro/nanobiological organisms by computational holographic microscopy," Proc. IEEE 97(6), 990-1010, 2009.

[3] F. Yi, I. Moon, Y. H. Lee, "Extraction of target specimens from bioholographic images using interactive graph cuts," Journal of biomedical optics, 18(12), 126015-126015,2013.

[4] F. Yi, I. Moon, Y. H. Lee, "Three-dimensional counting of morphologically normal human red blood cells via digital holographic microscopy," Journal of biomedical optics, 20(1), 016005-016005, 2015.

[5] C. Curl, C. J. Bellair, P. J. Harris, B. E. Allman, A. Roberts, K. A. Nugent, L. Delbridge, "Quantitative phase microscopy-a new tool for investigating the structure and function of unstained live cells," Proc. Aust. Physiol. Pharmacol. Soc. 34(12), 896-901, 2004.

[6] D. Fu et al., "Quantitative DIC microscopy using an off-axis self-interference approach," Opt. Lett. 35(14), 2370-2372, 2010.

[7] T. Tishko, Holographic Microscopy of Phase Microscopic Objects: Theory and Practice, World Scientific, Maryland, 2011.

[8] B. Javidi, F. Okano, and J. Sun, 3D Imaging, Visualization, and Display Technologies, Springer, New York, 2008.

[9] W. Osten, T. Baumbach, and W. Juptner, "Comparative digital holography," Opt. Lett. 27, 1764-1766, 2002.

[10] B. Rappaz, E. Cano, T. Colomb, J. Kuhn, C. Depeursinge, V. Simanis, P. J. Magistretti, and P. Marquet, "Noninvasive characterization of the fission yeast cell cycle by monitoring dry mass with digital holographic microscopy," J.

Biomed. Opt. 14(3), 034049-034049, 2009.

[11] Y. Frauel, T. Naughton, O. Matoba, E. Tahajuerce, and B. Javidi, “Three dimensional imaging and display using computational holographic imaging,” Proc. of IEEE 94, 636-654, 2006.

[12] I. Moon et al., “Automated three dimensional identification and tracking of micro/nano biological organisms by computational holographic microscopy,” Proc. IEEE 97, 990-1010, 2009.

[13] B. Javidi, I. Moon, and S. Yeom, “Real-time 3D sensing and identification of microorganisms,” Opt. Photon. News Mag. 17, 16-21, 2006.

[14] J. Goodman and R. Lawrence, “Digital image formation from electronically detected holograms,” Appl. Phys. Lett. 11(3), 77-79 ,1967.

[15] L. Onural and P. Scott, “Digital decoding of in-line holograms,” Opt. Eng. 26(11), 1124-1132, 1987.

[16] U. Schnars, “Direct phase determination in hologram interferometry with use of digitally recorded holograms,” J. Opt. Soc. Am. A 11(7), 2011-2015, 1994.

[17] D. Carl, B. Kemper, G. Wernicke, and G. von Bally, “Parameter-optimized digital holographic microscope for high-resolution living-cell analysis,” Appl. Opt. 43(36), 6536-6544, 2004.

[18] C. Wagner, W. Osten, and S. Seebacher, “Direct shape measurement by digital wavefront reconstruction and multi-wavelength contouring,” Opt. Eng. 39(1), 79-85, 2000.

[19] Y. Zhang, G. Pedrini, W. Osten, and H. J. Tiziani, “Reconstruction of in-line digital holograms from two intensity measurements,” Opt. Lett. 29(15), 1787-1789, 2004.

[20] M. Paturzo, F. Merola, S. Grilli, S. De Nicola, A. Finizio, and P. Ferraro, “Super-resolution in digital holography by a two-dimensional dynamic phase grating,” Opt. Express 16(21), 17107-17118, 2008.

[21] P. Langehanenberg et al., “Autofocusing in digital holographic phase contrast microscopy on pure phase objects for live cell imaging,” Appl. Opt. 47, D176-D182, 2008.

[22] J. Sheng, E. Malkiel, and J. Katz, “Digital holographic microscopy for measuring three-dimensional particle distributions and motions,” Appl. Opt. 45, 3893-3901, 2006.

[23] I. Moon and B. Javidi, “Shape tolerant three-dimensional recognition of biological microorganisms using digital holography,” Opt. Exp. 13, 9612-9622, 2005.

[24] F. Dubois, L. Joannes, and J. C. Legros, “Improved three-dimensional imaging with a digital holography microscope with a source of partial spatial coherence,” Appl. Opt. 38(34), 7085-7094, 1999.

[25] W. Xu, M. H. Jericho, I. A. Meinertzhagen, and H. J. Kreuzer, “Digital in-line holography for biological applications,” Proc. Natl. Acad. Sci. U. S. A. 98(20), 11301-11305, 2001.

[26] E. Cuche, F. Bevilacqua, and C. Depeursinge, “Digital holography for quantitative phase-contrast imaging,” Opt. Lett. 24(5), 291-293, 1999.

[27] E. Cuche, P. Marquet, and C. Depeursinge, “Simultaneous amplitude and quantitative phase contrast microscopy by numerical reconstruction of Fresnel off-axis holograms,” Appl. Opt. 38(34), 6994-7001, 1999.

[28] T. Colomb, E. Cuche, F. Charriere, J. Kuhn, N. Aspert, F. Montfort, P. Marquet, and C. Depeursinge, “Automatic procedure for aberration compensation in digital holographic microscopy and applications to specimen shape compensation,” Appl. Opt. 45(5), 851-863, 2006.

[29] E. Tajahuerce, O. Matoba, and B. Javidi, “Shift-invariant three dimensional object recognition by means of digital holography,” Appl. Opt. 40, 3877-3886, 2001.

[30] D. Abdelsalam, B. Baek, and D. Kim, “Precise test sieves calibration method

based on off-axis digital holography," J. Opt. Soc. Korea 15, 146-151, 2011.

[31] D. Boss et al., "Exploring red blood cell membrane dynamics with digital holographic microscopy," SPIE Photonics Europe, 77153I-77153I, 2010.

[32] E. Cuche, F. Bevilacqua, and C. Depeursinge, "Digital holography for quantitative phase-contrast imaging," Opt. Lett. 24(5), 291-293, 1999.

[33] B. Bhaduri et al., "Optical assay of erythrocyte function in banked blood," Sci. Rep. 4, 6211-6211, 2014.

[34] R. Liu et al.,"Recognition and classification of red blood cells using digital holographic microscopy and data clustering with discriminant analysis," J. Opt. Soc. Am. A 28(6), 1204-1210, 2011.

[35] I. Moon, B. Javidi, F. Yi, D. Boss, P. Marquet, "Automated statistical quantification of three-dimensional morphology and mean corpuscular hemoglobin of multiple red blood cells," Optics express, 20(9), 10295-10309, 2012.

[36] I. Moon, et al. "Automated quantitative analysis of 3D morphology and mean corpuscular hemoglobin in human red blood cells stored in different periods." Optics express 21(25), 30947-30957,2013.

[37] F. Yi, I. Moon, B. Javidi, D. Boss, P. Marquet, "Automated segmentation of multiple red blood cells with digital holographic microscopy," Journal of biomedical optics, 18(2), 026006-026006, 2013.

[38] N. Shaked, L. Satterwhite, and N. Bursac, "Whole-cell-analysis of live cardiomyocytes using wide-field interferometric phase microscopy," Biomedical optics express 1(2) 706-719, 2010.

[39] V. Salnikov, Y. Lukyanenko, W. Lederer, and V. Lukyanenko, "Distribution of ryanodine receptors in rat ventricular myocytes," J. Muscle Res. Cell Motil. 30(3-4), 161-170, 2009.

[40] D. Hickson-Bick, G. Sparagna, L. Buja, and J. McMillin, "Palmitate-induced apoptosis in neonatal cardiomyocytes is not dependent on the generation of ROS," Am. J. Physiol. Heart Circ. Physiol. 282(2), H656-H664, 2002.

[41] E. Azeloglu and K. Costa, “Cross-bridge cycling gives rise to spatiotemporal heterogeneity of dynamic subcellular mechanics in cardiac myocytes probed with atomic force microscopy,” Am. J. Physiol. Heart Circ. Physiol. 298(3), H853-H860, 2010.

[42] A. Kamgoue, J. Ohayon, Y. Usson, L. Riou, and P. Tracqui, “Quantification of cardiomyocyte contraction based on image correlation analysis,” Cytometry A 75(4), 298-308, 2009.

[43] J. Dykens, Y. Will, “The significance of mitochondrial toxicity testing in drug development,” Drug discovery today 12(17), 777-785, 2007.

[44] B. Xi, T. Wang, and N. Li, “Functional cardiotoxicity profiling and screening using the xCELLigence RTCA Cardio System,” Journal of the Association for Laboratory Automation 16(6), 415-421, 2011.

[45] O. Sirenko, C. Crittenden, and N. Callamaras, “Multiparameter in vitro assessment of compound effects on cardiomyocyte physiology using iPSC cells,” Journal of biomolecular screening 18(1), 39-53, 2013.

[46] S. Braam, L. Tertoolen, and A. Stolpe, “Prediction of drug-induced cardiotoxicity using human embryonic stem cell-derived cardiomyocytes,” Stem cell research, 4(2), 107-116, 2010.

[47] M. Jonsson, Q. Wang, and B. Becker, “Impedance-based detection of beating rhythm and proarrhythmic effects of compounds on stem cell-derived cardiomyocytes,” Assay and drug development technologies 9(6), 589-599, 2011.

[48] Y. Abassi, B. Xi, N. Li, W. Ouyang, A. Seiler, M. Watzele, R. Kettenhofen, H. Bohlen, A. Ehlich, E. Kolossov, X. Wang, and X. Xu, “Dynamic monitoring of beating periodicity of stem cell-derived cardiomyocytes as a predictive tool for preclinical safety assessment,” British journal of pharmacology 165(5), 1424-1441, 2012.

[49] C. Carlson, C. Koonce, N. Aoyama, S. Einhorn, S. Fiene, A. Thompson, B. Swanson, B. Anson, and S. Kattman, “Phenotypic screening with human iPS

Cell-Derived Cardiomyocytes HTS-Compatible Assays for Interrogating Cardiac Hypertrophy," Journal of biomolecular screening 18(10), 1203-1211, 2013.

[50] O. Sirenko, E. F. Cromwell, C. Crittenden, J. Wignall, F. Wright, I. Rusyn, "Assessment of beating parameters in human induced pluripotent stem cells enables quantitative in vitro screening for cardiotoxicity," Toxicology and applied pharmacology 273(3), 500-507, 2013.

[51] P. Marquet, B. Rappaz, P. Magistretti, E. Cuche, Y. Emery, T. Colomb, and C. Depeursinge, "Digital holographic microscopy: a noninvasive contrast imaging technique allowing quantitative visualization of living cells with subwavelength axial accuracy," Optics letters 30(5), 468-470, 2005.

[52] B. Rappaz, B. Breton, E. Shaffer, and G. Turcatti, "Digital holographic microscopy: a quantitative label-free microscopy technique for phenotypic screening," Combinatorial chemistry & high throughput screening 14(1), 80-88, 2014.

[53] B. Rappaz, P. Marquet, E. Cuche, Y. Emery, C. Depeursinge, and P. Magistretti, "Measurement of the integral refractive index and dynamic cell morphometry of living cells with digital holographic microscopy," Optics express 13(23), 9361-9373, 2005.

[54] B. Rappaz, E. Cano, T. Colomb, J. Kühn, C. Depeursinge, V. Simanis, P. Magistretti, and P. Marquet, "Noninvasive characterization of the fission yeast cell cycle by monitoring dry mass with digital holographic microscopy," Journal of biomedical optics, 14(3), 034045-034049, 2009.

[55] B. Rappaz, A. Barbul, Y. Emery, R. Korenstein, C. Depeursinge, P. Magistretti, and P. Marquet, "Comparative study of human erythrocytes by digital holographic microscopy, confocal microscopy, and impedance volume analyzer," Cytometry Part A 73(10), 895-903, 2008.

[56] E. Cuche, P. Marquet, and C. Depeursinge, "Simultaneous amplitude and quantitative phase contrast microscopy by numerical reconstruction of Fresnel off-axis holograms," Appl. Opt. 38(34), 6994-7001, 1999.

[57] T. Colomb et al., “Automatic procedure for aberration compensation in digital holographic microscopy and application to specimen shape compensation,” Appl. Opt. 45(5), 851-863, 2006.

[58] F. Yi, I. Moon, “Image segmentation: A survey of graph-cut methods,” In Systems and Informatics (ICSAI), 2012 International Conference on, 1936-1941, IEEE, 2012.

[59] R. C. Gonzalez, R. E. Woods, Digital Imaging Processing; Prentice Hall, New York, NY, USA, 2002

[60] F. Yi, I. Moon, “Automatic calculation of tree diameter from stereoscopic image pairs using digital image processing,” Applied Optics, 51 (18), 4120-4128, 2012.

[61] P. Soille, Morphological image analysis: principles and application; Springer-Verlag, NewYork, 2003.

[62] F. Meyer, “Topographic distance and watershed lines,” Signal process, 38(1), 113-125, 1994.

[63] S. Saraswathi, A. Allirani, “Survey on image segmentation via clustering,” International conference on information communication and embedded systems, 331-335, 2013.

[64] F. Yi, I. Moon, “Extended K-Means Algorithm,” In 5th International Conference on Intelligent Human-Machine Systems and Cybernetics (IHMSC), 2, 263-266, 2013.

[65] W. Tao, H. Jin, Y. Zhang, “Color image segmentation based on mean shift and normalized cuts,” IEEE Trans on systems, man, and cybernetics-part B: cybernetics, 37(5), 1382-1389, 2007.

[66] D. Comaniciu, P. Meer, “Mean shift: A robust approach toward feature space analysis,” IEEE Trans on pattern analysis and machine intelligence, 24(5), 603-619, 2002.

[67] Y. Cheng, “Mean shift, mode seeking, and clustering,” Pattern Analysis and Machine Intelligence, IEEE Transactions on 17(8), 790-799, 1995.

[68] M. Sonka, V. Hlavac, R. Boyle, Image processing, analysis, and machine vision. Thomson, United States, 2008.

[69] M. Kass, A. Witkin, D. Terzopoulos, “Snakes: active contour models,” International journal of computer vision, 1(4), 321-331, 1988.

[70] C. Xu, J. L. Prince, “snakes, shapes, and gradient vector flow,” IEEE Trans on image processing, 7(3), 359-369, 1998.

[71] I. Dagher, K. EI Tom, “Water Balloons: A hybrid watershed Balloon Snake segmentation,” Image and Vision Computing, 26(7), 905-912, 2008.

[72] J. Malek, et al. “Automated breast cancer diagnosis based on GVF-Snake segmentation, wavelet features extraction and fuzzy classification,” Journal of Signal Processing Systems, 55(1-3), 49-66, 2009.

[73] P. Yu, C. L. Poh, “Region-based snake with edge constraint for segmentation of lymph nodes on CT images,” Computers in biology and medicine, 60, 86-91, 2015.

[74] V. Caselles, R. Kimmel, G. Sapiro, “Geodesic active contours,” International journal of computer vision, 22(1), 61-79, 1997.

[75] S. Osher, J. A. Sethian, “Fronts propagating with curveature dependent speed: algorithms based on Hamilton-jacobi formulations,” Journal of computational physics, 79(1), 12-49, 1988.

[76] C. Li, et al. “A level set method for image segmentation in the presence of intensity inhomogeneities with application to MRI,” IEEE Transactions on Image Processing, 20(7), 2007-2016, 2011.

[77] F. P. Van der Meer, N. Moës, and L. J. Sluys, “A level set model for delamination – Modeling crack growth without cohesive zone or stress singularity,” Engineering Fracture Mechanics 79, 191-212, 2012.

[78] K. Zhang, et al. “Reinitialization-free level set evolution via reaction diffusion,” IEEE Transactions on Image Processing, 22(1), 258-27, 2013.

[79] C. Feng, et al. “Segmentation of the left ventricle using distance regularized two-layer level set approach,” Medical Image Computing and Computer-Assisted Intervention-MICCA, Springer Berlin Heidelberg, 477-484, 2013.

[80] Y. Liu, et al. “A novel level set method for segmentation of left and right ventricles from cardiac MR images,” Engineering in Medicine and Biology Society (EMBC) 36th Annual International Conference of the IEEE. 4719-4722, 2014.

[81] K. Zhang, L. Zhang, and M. H. Yang, “Real-time object tracking via online discriminative feature selection,” IEEE Transactions on Image Processing, 22(12), 4664-4677, 2013.

[82] Y. B. Yuri, G. F. Lea, “Graph cuts and efficient N-D image segmentation,” International journal of computer vision, 70(2), 109-131, 2006.

[83] Y. B. Yuri, M. P. Jolly, “Interactive graph cuts for optimal boundary &region segmentation of objects in N-D image,” International conference on computer vision, I, 105-112, 2001.

[84] Y. Boykov, V. Kolmogorov, “An experimental comparison of min-cut/max-flow algorithm for energy minimization in vision,” IEEE Trans on PAMI, 26(9), 1124-1137, 2004

[85] Y. Hou, B. L. Guo, J. S. Pan, “The application and study of graph cuts in motion segmentation,” International conference on IAS, 265-268, 2009.

[86] I. Moon, et al. “Automated quantitative analysis of 3D morphology and mean corpuscular hemoglobin in human red blood cells stored in different periods,” Optics express 21(25), 30947-30957, 2013.

[87] H. G. Davies, M. H. F. Wilkins, J. Chayen, and L. F. La Cour, “The use of the interference microscope to determine dry mass in living cells and as a quantitative cytochemical method,” Quarterly journal of microscopical science 3(31), 271-304, 1954.

[88] T. Tishko, T. Dmitry, and T. Vladimir, Holographic Microscopy of Phase

Microscopic Objects Theory and Practice, World Scientific, 2011.

[89] V. Fairbanks, G. Klee, G. Wiseman, J. Hoyer, A. Tefferi, R. Petitt, and M. Silverstein, "Measurement of blood volume and red cell mass: Re-examination of 51Cr and 125I methods," Blood Cells Foundation 22(2), 169-186, 1996.

[90] B. Rappaz, A. Barbul, Y. Emery, R. Korenstein, C. Depeursinge, P. J. Magistretti, and P. Marquet, "Comparative study of human erythrocytes by digital Holographic microscopy, confocal microscopy, and impedance volume analyzer," Cytometry 73A(10), 895-903, 2008.

[91] D. Boss, J. Kuhn, P. Jourdain, C. Depeursinge, P. J. Magistretti, and P. Marquet, "Measurement of absolute cell volume, osmotic membrane water permeability, and refractive index of transmembrane water and solute flux by digital holographic microscopy," J. Biomed. Opt. 18(3), 036007-036007, 2013.

[92] R. Barer, "Interference microscopy and mass determination," Nature 169(4296), 366-367, 1952.

[93] W. B. Lockwood, R. W. Hudgens, I. O. Szymanski, R. A. Teno, and A. D. Gray, "Effects of rejuvenation and frozen storage on 42-day-old AS-3 RBCs," Transfusion 43(11), 1527-1532, 2003.

[94] "Transfusion handbook, summary information for red blood cells," National Blood Transfusion Committee.

[95] A. Rencher, Methods of Multivariate Analysis, Wiley-Interscience, New York, 2002.

[96] E. Tajahuerce, O. Matoba, and B. Javidi, "Shift-invariant three dimensional object recognition by means of digital holography," Appl. Opt. 40, 3877-3886, 2001.

[97] E. Gose and R. Johnsonbaugh, Pattern Recognition and Image Analysis, Prentice Hall, New Jersey, 1996.

[98] R. Duda, P. Hart, and D. Stork, Pattern Classification, Wiley-Interscience, New York, 2000.

[99] F. Yi, I. Moon, and Y. H. Lee, “Three-dimensional counting of morphologically normal human red blood cells via digital holographic microscopy,” Journal of biomedical optics 20(1), 016005-016005, 2015.

[100] J. Bacus and J. Weens, “Automated method of differential red blood cell classification with application to the diagnosis of anemia,” J. Histochem. Cytochem. 25, 514-632, 1977.

[101] B. Xi, T. Wang, and N. Li, “Functional cardiotoxicity profiling and screening using the xCELLigence RTCA Cardio System,” Journal of the Association for Laboratory Automation 16(6), 415-421, 2011.

[102] W. Moerner and D. Fromm, “Methods of single-molecule fluorescence spectroscopy and microscopy,” Review of Scientific Instruments, 74(8), 3597-3619, 2003.

[103] F. Sadjadi, “Experimental design methodology: The scientific tool for performance evaluation,” Proceedings of SPIE 1310, 100-107, 1990.

ACKNOWLEDGEMENTS

When I finish typing the last character of my doctoral dissertation in the evening, a lot of things appear in my head. I believe the future is wonderful. There were so many meaningful moments I cannot forget and so many people I have to thank.

I am most grateful to my supervisor, Professor Inkyu Moon, for his patient assistance and constant guidance. Without his consistent and illuminating instruction, this dissertation could not have reached its present form. Prof. Moon not only leads me into the world of scientific research but also helps me a lot in life. I clearly remember that Prof. Moon always treated me to dinner after I joined his research group in the year of 2010. In addition, Prof. Moon often helped me buy the air ticket when I went back to China for Chinese New Year. Most importantly, Prof. Moon trusts me very much, which lets me feel free to do any researches. He is also concerned about my future and supports me to do any programs that are beneficial to my future.

I am greatly indebted to my three key mentors in my life. They are 유영철, Kyusung Chung, and Yonghui Xue. It is the encouragement and praise from them that make me from an inferior person to a confident one. They have set a good example for me regarding how to treat others and achieve the value of life. The characteristics of these three mentors have also been my guiding torch in life.

My deepest gratitude goes to my parents, Xuxin Yi and Huoxiu Zhou, who are the greatest persons in my heart. Their unconditional love and support have always been the invariants of my life. Different from my peers' parents in my homeland who only want their children to make money when they become adults, my parents give me enough support to pursue knowledge in school because they believe that knowledge change destiny. I also give my thanks to my old brother and sister who have shared uncountable hours of laughter and joy with me. It is they that take care of my parents when I am out of China. Special thanks are given to my parents-in-law, sister-in-law, and brother-in-law, for their unmatched support and understanding.

I feel grateful to all the professors at Chosun University who once offered me valuable courses and advice during my study. These professors include Prof. Moon Inkyu, Prof. Lee Sangwoong, Prof. Kang Moonsu, Prof. Chung Ilyong, Prof. Cho Beomjoon, Prof. Kim Choongwon, Prof. Moh Sangman, Prof. Shin Yongsuk, and Prof. Kwon Gurak. Especially, I would like to thank Prof. Chung Ilyong for his help before I came to Chosun University. I also wish to thank my colleagues who made my experience a joyful one. These colleagues consist of 정유선, Tabassum Nasrin, Han Minggu, Inbarasan Muniraj, Rao Saifullah, We Jonggob. Senior colleague 정유선 is a very patient person and helps me a lot in terms of preparation of Korean document and adaption of Korean life.

My gratitude also extends to my friends who I always play together with in Korea, especially, my friends Hongzhuo Qian and Huan Xu. It is they who let me know Korea better and make my spare time rich and colorful. I will never forget the happy time we spent together in Korea. I also want to express my thanks to my other two friends Zeming Zhao and Zuoming Zhou who always let me feel pleased and stress-free. It is indeed my honor to have these wonderful friends.

Last my thanks would go to my beautiful and charming wife Xinfeng Feng who has supported me a lot for every choice I made. If we say there is a great woman behind every man who has got his doctoral degree, this great woman is definitely my wife in my case. It is she who shares with me every happy moment. It is also she who enhances my happiness. She agreed to marry with me at the time when I have nothing. Undoubtedly, I will appreciate my wife forever.

In brief, I deeply appreciate all of the professors, relatives, colleagues, and friends who have helped me a lot. I sincerely wish them all the best in their lives.

致謝

当在寂静的夜晚敲完博士論文的最后一个字符時，我思緒万千。這一路的歷程就如電影般精彩絶倫，我不是導演，但确是主角。太多的事値得回憶，太多的人値得感謝。相信這所經歷的一切都預示了未來的美好。我也确信，未來必定美好。

忘記不了影響我一生，給我指引前進道路的三位老師，兪榮哲，丁奎盛，薛永輝。是他們的教導，鼓勵与贊美讓我樹立起了自信，感触到人生的美好。他們的話使我倍感親切并充滿无窮的力量。非常感謝他們。

感謝在我來韓國之前，是丁教授 (Prof. Chung Ilyong) 提前帮我聯系好了導師和奬學金。沒有丁教授的帮助，我不會認識在碩博階段一直指導着我的文教授（Prof. Moon Inkyu). 文教授不僅在學術上指導我，讓我知道怎么去思考，研究，寫作論文。在生活上，文教授也給与了我极大大的帮助。清楚的記得，当我在第一年還沒适應韓國的飲食習慣時，是文教授經常帶着我去吃我比較喜歡的飲食（主要是不用我買單）。每次回國，文教授都給我路費，讓我倍感溫馨。最重要的是，文教授對我十分的信任，使我能放開的去做研究，去處理身邊的事情。同時，教授也十分關心我的未來，只要對我有益的事，教授都給予全力的支持。在此，把我最誠摯的謝獻給我尊敬的文教授。

我也非常感謝我的爸爸，媽媽。爸爸媽媽是我心中最偉大的人，也是我永遠的榜樣。是他們靠着自己勤勞的双手讓我順利念完大學。不同農村很多其他父母希望孩子們早点出來掙錢，我爸爸媽媽一直非常支持我求學的道路，因爲他們相信，知識能改變命運。即使自己再苦再累，也始終无怨无悔。在讀博的歲月里，爸媽的双鬢也慢慢變白了，作爲儿子，實在感覺亏欠他們太多。然而，爸媽還是一如既往的支持着我一切的選擇。謝謝爸爸媽媽。同時也感謝我的哥哥姐姐。是他們給了我童年的歡樂，是他們在我遠离家鄉時照顧着爸媽，讓我能安心求學。因爲哥哥姐姐，我們的家庭才始終充滿了溫暖。同樣，也感謝我的嫂子和姐夫，家庭的溫馨离不開她們的支持。

其次，衷心的感謝教過我課程的老師們。他們是：Prof. Moon Inkyu, Prof. Lee Sangwoong, Prof. Kang Moonsu，Prof. Chung, Ilyong, Prof. Cho Beomjoon, Prof. Kim Choongwon, Prof. Moh Sangman, Prof. Shin Yongsuk, and Prof. Kwon Gurak. 是他們讓我獲取到更多更全面的知識。也感謝和我一个實驗室的同僚們。他們是정유선，Tabassum Nasrin, Han Minggu, Inbarasan Muniraj, Rao Saifullah, We Jonggob. 是她們讓實驗室充滿有活力，使我有个和諧的辦公环境。特別感謝정유선學姐，每次有材料信息需要處理時，都能得到她熱心的帮忙。對我的帮助，정유선學姐非常有耐心，而且會帮到底。非常感謝有這么一位前輩。

同樣感謝在韓國經常一起玩的小伙伴們。感謝月光的朋友們，特別是錢紅卓和徐歡。是紅卓和徐歡讓我更多的了解韓國，他們讓我的業余生活更加多彩。忘不了我們在韓國一起旅游的日子。也謝謝我倆个叫胖子的好朋友，趙則名和周佐明。有煩惱壓力時，來自他們的哪怕一个扣鼻屎的QQ圖，都能讓我壓力大減。

最后，非常感謝我漂亮的妻子，馮新鳳。從我們相識開始，她就一直支持着我所做出的任何一个選擇。如果說每个完成博士學位的男人背后都有一个支持他的女人的話，那對于我，這个女人就是我的妻子。是她，讓我沒有后顧之憂，是她，讓我有更强的幸福感，也是她陪我度過每个困難的時刻，分享每个歡樂的時光。在我一无所有的時候，她愿意成爲我的妻子，使我万分感動，我將永遠銘記在心。

總之，在博士論文完成之際，謹以此文獻給所有帮助過我的親人，老師，同學和朋友們。也衷心祝福他們，愿他們一生幸福！

2015년 8월

박사학위 논문

Quantitative Analysis of Three-dimensional Morphology and Biophysical Cell Parameters of Live Cells using Digital Holographic Imaging

조선대학교 대학원

컴 퓨 터 공 학 과

역 발 류

Quantitative Analysis of Three-dimensional Morphology and Biophysical Cell Parameters of Live Cells using Digital Holographic Imaging

디지털 홀로그래픽 영상 기반 생물세포 3차원 모폴러지 및 생물리학적 셀파라미터의 정량적 분석방법에 관한 연구

2015년 8월 25일

조선대학교 대학원

컴 퓨 터 공 학 과

역 발 류

Quantitative Analysis of Three-dimensional Morphology and Biophysical Cell Parameters of Live Cells using Digital Holographic Imaging

지도교수 문 인 규

이 논문을 공학 박사학위신청 논문으로 제출함

2015년 4월

조선대학교 대학원

컴 퓨 터 공 학 과

역 발 류

역발류의 박사학위논문을 인준함

위 원 장	조선대학교	교 수	정 일 용(인)
위 원	조선대학교	교 수	이 상 웅(인)
위 원	조선대학교	교 수	권 구 락(인)
위 원	한경대학교	교 수	조 명 진(인)
위 원	조선대학교	교 수	문 인 규(인)

2015년 6월

조선대학교 대학원

CONTENTS

LIST OF FIGURES

LIST OF TABLES

ABSTRACT

Quantitative Analysis of Three-dimensional Morphology and Biophysical Cell Parameters of Live Cells using Digital Holographic Imaging

Faliu Yi
Advisor : Prof. Inkyu Moon, Ph.D.
Department of Computer Engineering
Graduate School of Chosun University

For semitransparent or transparent biological cells, the intensity based two-dimensional (2D) imaging system suffers from losses of a large amount of quantitative detailed information about cell structure and content. 2D imaging method also results in low-contrast image. On the contrary, three-dimensional imaging (3D) technique such as digital holography comes to the forefront as promising tools for 3D biological cells visualization, pattern recognition and study of their dynamics as it can provide rich 3D information, such as the surface morphological and optical thickness data of these microscopic objects. Among a large number of developed 3D imaging platforms, digital holographic microscopy (DHM) as a promising 3D imaging system has widely viewed in life sciences, medical diagnoses, and medicine due to its advantages in terms of easy configuration and fast imaging, low-cost and non-destruction to microorganisms.

In this dissertation, The automated analysis of 3D cells that are obtained by DHM is focused. Totally, two different kinds of transparent cells, which are

red blood cells (RBCs) and cardiomyocytes, are three-dimensionally imaged and quantitatively analyzed. Both RBCs and cardiomyocytes phase images are numerically reconstructed from holograms recorded by DHM. RBCs has been extensively studied in bio-medical fields due to its important functionality in delivering oxygen from lungs to body tissues and transporting carbon dioxide from the tissues to the lungs. The resulted characteristic properties of 3D RBCs from DHM are beneficial to characterize cell storage lesions, recognize unnormal RBCs, and evaluate drug testing. On the other hand, cardiomyocytes or myocardial cells, which are the main contractile elements of the heart muscle, generate human heart beating and control blood flow through the blood vessels of the circulatory system. The automated analysis of 3D cardiomyocytes are crucial to improve the predictability of compound toxicity through safety profiling assays during the lengthy drug discovery process in order that potentially toxic compounds are detected early in the process before significant time and important financial investments are made. Experimental results are presented that demonstrate the feasibility of the automated analysis procedure for both 3D RBCs and cardiomyocytes.

초 록

디지털 홀로그래픽 영상 기반 생물세포 3차원 모폴러지 및 생물리학적 셀파라미터의 정량적 분석방법에 관한 연구

Faliu Yi
Advisor : Prof. Inkyu Moon, Ph.D.
Department of Computer Engineering
Graduate School of Chosun University

2D 이미징 시스템 기반에 집중된 반투명 또는 투명 생물학적 세포는 세포 구조와 내용에 대한 상세한 정량적 정보가 대량 손실된다.2D 이미징 기술은 저채도 이미지에서 동일한 결과를 보인다. 반대로, 디지털 홀로그램과 같은 3차원 이미징 기술은 3D 생물학적 세포 시각화, 표면 형태와 세포의 광학적 두께와 같은 풍부한 3D정보를 제공함으로써 패턴 인식과 그 동적 연구 분야를 위한 선두 기술로써 각광을 받고 있다.개발된 3D 이미징 기술 중, 촉망되는 3D 이미징 시스템으로써 DHM에 기반한 3D 이미징 플랫폼은 쉬운 구조와 빠른 이미징 처리, 저비용 그리고 미생물 비파괴 측면의 이점으로 인하여 생명과학, 의료진단 그리고 의학에서 광범위하게 보여진다.

본 논문에서는 DHM에 의해 획득한 3D 셀의 자동 분석에 중점을 둔다. 전적으로, 적혈구와 심장근육세포와 같은 두 가지 다른 종류의 투명 세포는 3차원적 영상화와 정량 분석을 하였다. 적혈구와 심장근육세포 위상 이미지는 DHM에 의해 기록된 홀로그램으로부터 절대적으로 재구성된다.적혈구는 폐에서 신체 조직으로 산소를 전달 및 조직에서 폐로 이산화탄소를 보내는 것에서 중요한 기능을 하기 때문에 바이오 메디컬 분야에서 광범위하게 연구되어지고 있다. DHM에서 생성된 3D 적혈구의 특유 성질은 세포 병변 특성, 비정상 적혈구 인식 그리고 약물 테스트에 유

익하다. 한편, 심장근육 수축의 주요소인 심장근육세포나 심근세포는 일반적인 사람의 심장 박동과 순환계의 혈관을 통해 혈액 흐름을 제어할 수 있다. 자동 분석된 3D 심장근육세포는 잠재적인 독성 화합물이 긴 시간과 투자비용으로 만들어지기 전에 프로세서 초기에 감지되어지는 순서로 오랜 신약 개발 과정동안 안전적인 프로파일 링 분석을 통하여 화합물 독성의 예측을 향상시키기 위해 매우 중요하다. 본 실험 결과는 3D 적혈구와 심장근육세포 모두에 자동화된 분석 과정의 실행성을 증명하여 보여준다.

1. Introduction

For semitransparent or transparent biological targets, the intensity based two-dimensional (2D) imaging system suffers from losses of a large amount of quantitative detailed information about cell structure and content. 2D imaging method also results in low-contrast image [1-4]. Even though some advanced 2D imaging systems, such as quantitative phase contrast and differential interference contrast microscopes [3-6], have the feature to quantitatively investigate the biological microorganisms to some extent, they cannot provide optical thickness information about the imaging biological cells, which in turn make the analysis of microscopic object limited. 2D imaging microscopic system has fundamental limitations on quantifying information about 3D morphology, dry mass production, and density of the biological cells. Moreover, it is difficult to dynamically visualize the character of variations in morphology of semitransparent or transparent microorganisms because they seen to be the same under 2D imaging microscopic systems [7].

The three-dimensional (3D) holographic imaging system has been studied for visualization, identification, and tracking of biological micro/nano- organisms [8-20]. In the areas of biomedical imaging, defense, medical diagnosis, medical therapeutics, and security, the 3-D holographic imaging system has a lot of potential [8-26]. Consequently, 3D digital image processing, which can directly affect future research on the microscopic objects under study, becomes more and more important because it becomes easier and more convenient to obtain the computational 3D image of the microorganisms with the development of the 3D optical holographic imaging system. Without limitations existed in 2D image system, the holographic images reconstructed numerically from a hologram obtained by 3D digital holography-based imaging systems can provide rich 3D information, such as the surface morphological and optical thickness data of the microorganism targets, which make it possible for the 3D measurement of

microscopic objects. Among varied number of 3D imaging techniques, digital holographic microscopy (DHM) as one of the promising 3D imaging methods has been widely researched for observation, metrology, and tracking of biological micro/nano-organism as it is a low-cost and non-invasive, fast imaging and easy configured approach [27-32]. Compared with classical optical microscopy, DHM provides a major advantage in overcoming the classical depth of field limitation. DHM is also a quantitative phase imaging technique which directly and non-invasively provides the optical thickness of biological cells in live and dynamic conditions which other 3D imaging techniques such as the electron microscopy are destructive to the imaging cells. Since DHM is not destructive for specimens, they can be investigated once more by any other optical imaging systems.

In this dissertation, the automated analysis of 3D cells that are obtained by DHM is focused. Totally, two different kinds of transparent cells, which are red blood cells (RBCs) and cardiomyocytes, are three-dimensionally imaged and quantitatively analyzed. Both RBCs and cardiomyocytes quantitative phase images are numerically reconstructed from holograms recorded by DHM. As essential ingredients of human being, the automated analysis of both 3D RBCs and cardiomyocytes are helpful to the investigation of RBC-related and cardiomyocyte-related diseases [7]. Moreover, the characteristic properties of these 3D cells can be used to screen the compounds during drug testing.

RBCs are essential ingredients of bloodstream in human being. They cannot only deliver oxygen to body tissues via the blood flowing through the circulatory system in vertebrate organisms, but also absorb oxygen in the lungs and release it when squeezing through the body's capillaries [33-34]. Normally, a relatively stable number of RBCs is maintained in the circulatory system and it is necessary to stimulate RBCs production with medications for patients suffering from anemia. Recent studies show that there are numerous biochemical, structural, inflammatory, and physiologic changes in stored red cells, referred to as red cell storage lesion, which to some extent impacts the

clinical outcome in transfused patients [35]. Therefore, the analysis of some quantitative cell parameters provided by DHM, including 3D morphology, mean corpuscular volume, and hemoglobin content at different storage periods will be helpful to characterize red cell storage lesions [36]. Moreover, it is estimated that the composition of RBCs types in human blood would be different for varied RBC-related diseases. The disordered change of 3D RBC in morphology shape can affect other body tissues indirectly. As a result, it is extremely important to have a classificaton algorithm that can categorize different types of RBCs effectively and efficiently in order to overcome the shortage of the traditional method that is time-consuming and labor-intensive [4]. In addition, counting cell types in the blood is an important task for evaluating clinical status. However, the RBCs extraction which refers to as RBCs segmentation has to be conducted first in order to measure the characteristic properties of each RBC. RBCs segmentation also benefit to the further RBCs analysis such as RBC recognition and tracking. In this dissertation, three directions are done in terms of automated 3D RBCs analysis after the RBCs phase images are numerically reconstructed from holograms that are recorded with DHM system. The fundamental and the most important one is the RBCs segmentation [37]. The results of RBCs segmentation can directly affect the following study of RBCs. A good RBCs extraction method should at least results in low over-segmentation and under-segmentation. The second research direction about 3D RBCs is the quantitative analysis of RBCs stored in different periods. These results would reveal the relationship between the RBC characteristic properties and their aging. This analysis will also be beneficial to the understanding of the features of RBCs with different storage periods and evaluation of any modifications in the 3D cell morphology and hemoglobin content induced by the length of storage time. The third research direction about 3D RBCs is the automated counting of morphologically normal RBCs. This will be helpful to measure the percentage of typical normal shapes of RBCs in a reconstructed RBC phase image that consists of multiple RBCs for disease diagnosis and drug

testing.

Cardiomyocytes or myocardial cells [38], which are the main contractile elements of the heart muscle, generate human heart beating and control blood flow through the blood vessels of the circulatory system. Like many other types of biological cells, cardiomyocytes are mostly transparent.The optical imaging systems used to capture cardiomyocytes images previously reproted include fluorescence microscopy, atomic force microscopy, phase contrast and differential interference contrast microscopy [39-42]. For fluorescence microscopy, biological molecules can be fluorescently stained and the location of a protein can be traced. However, the fluorescence is not permanent and easily fades. In addition, fluorescence labeling can induce adverse effect on the measured molecule or interfere with the parameter assessed. Similarly atomic force microscopy provides a 3D surface profile of the samples. However, this technique is limited by its scanning speed. On the contrary, DHM as described previously is a label-free quantitative imaging technique, able to non-invasively capture the entire complex field distribution including the amplitude and phase information of cardiomyocytes. Consequently, much richer information on the cardiomyocyte structure can be obtained by using DHM. During the lengthy drug discovery process it is crucial to improve the predictability of compound toxicity through safety profiling assays in order that potentially toxic compounds are detected early in the process before significant time and important financial investments are made. Between 1994 and 2006 from the new drugs approved by the US Food and Drug Administration (FDA), 38 were later withdrawn from the market because of safety concerns, the majority being cardiotoxic or hepatotoxic. Safety assements are therefore performed in preclinical drug development for revealing the possible drug side effects in particular those that may affect the electrical conduction and beating of the heart [43-47]. Therefore, researchers and pharmaceutical companies have to ensure that the effect to lead candidate compounds on cardiac function strictly satisfy criteria. Consequently, it is critical to establish more informative in vitro cardiotoxicity screens and data

analysis algorithms at the early phases of drug development for preventing late stage failure [48-50]. In the present work, the dynamic phase profile of beating cardiomyocytes, which are proportional to the optical path delay profile of the cell, are reconstructed from holograms that are captured through DHM. The beating activities of cardiomyocytes, and contraction and relaxation profiles are derived from the reconstructed phase image. In addition, other characteristic parameters used to categorize phenotypes such as rising time, falling time, peak width, and frequency are analyzed. These parameters are valuable for the analysis of drug candidates' effects on cardiomyocytes. More precisely, the dynamic beating profile of cardiomyocytes are obtained with two proposed methods, either by monitoring the average or the variance information of imaged cardiomyocytes. On the other hand, the contraction and relaxation movement of cardiomyocytes are quantified by analysis the difference between two successively acquired DHM phase images. The automated procedure for multiple parameters recording on cardiomyocytes dynamics for application in drug toxicity screens is proposed.

This dissertation is organized as follows. In section 2, the digital holographic microscopy is described. In section 3, the automated analysis of RBCs phase images obtained by DHM with experimental results is given. In section 4, the automated analysis about multiple parameters of dynamic cardiomyocytes images resulted from DHM is presented along with experimental results. Then, this dissertation is concluded in section 5.

2. Digital holographic microscopy

Digital holographic microscopy (DHM) has been studied for application in the field of cell biology, including automated cell counts, recognition, classification, three-dimensional tracking, and discrimination between physiological and pathophysiological states [27-32, 51-55]. Briefly, DHM is a label-free interferometric microscopy technique which provides a quantitative measurement of the optical path length. It is a two-step process where a hologram consisting of an interference pattern is first recorded on a digital CCD camera and the quantitative phase images are reconstructed numerically using a specific algorithm [56-57]. With current computer power, the reconstruction process can be achieved on-the-fly at a speed of 100Hz. The quantitative phase images are related to the optical path difference (OPD),expressed in terms of physical properties as:

$$OPD(x,y) = d(x,y) \times [n_c(x,y) - n_m], \quad (1)$$

where d(x,y) is the cell thickness, $n_c(x,y)$ is the mean intracellular refractive index integrated along the optical axis at the (x,y) position and $n_m$is the refractive index of the surrounding culture medium. Simply, Equation 1 means that the OPD signal is proportional to both the cell thickness and the intracellular refractive index, a property linked to the protein and water content of the cells [54-55]. DHM systems generally use a low intensity laser as a light source for specimen illumination and a digital camera to record the hologram. Here, the 684 nm laser source delivers roughly 200 $\mu w/cm^2$ at the specimen plane - that is some six orders of magnitude less than intensities typically associated with confocal fluorescence microscopy. With that amount of light, the exposure time is only 400 μs. An extensive quality control of DHM can be found in [55]. The schematic of the off-axis digital holographic microscopy is shown in Figure 1.The experimental setup in Figure 1 is a modified MachZehnder configuration with a laser diode source (λ= 684 nm). The

laser beam is divided into a reference wave and an object wave. The object wave is diffracted by the biological samples, magnified by a 40×/0.75NA microscope objective and interferes, in the off-axis geometry, with the reference wave to produce the hologram recorded by the CCD camera. The reconstruction and aberration compensation of the microorganism wavefront is obtained by using the numerical algorithm described in [56-57].

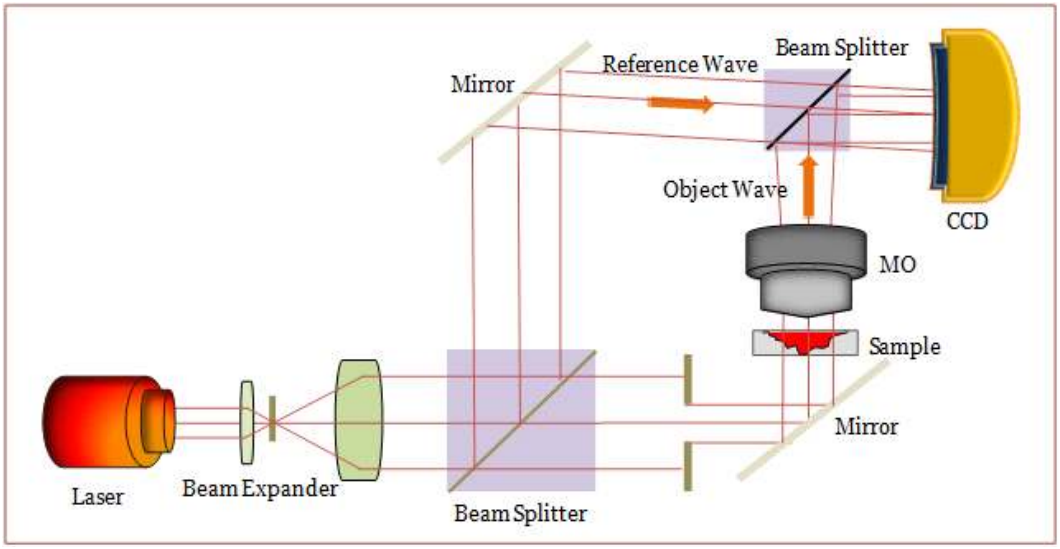

Fig. 1 Schematic of the off-axis digital holographic microscopy.

3. Automated Analysis of Three-dimensional Red Blood Cells

The holograms of RBCs are recorded on CCD camera with DHM technique. Then, the RBCs phase images are numerically reconstructed from these RBC holograms. In this section, the RBC phase images have to be firstly segmented and then the segmented RBCs are used to do following analysis such as quantitative analysis of RBCs stored in different periods and automated counting of morphological normal RBCs.

3.1 Segmentation of Red Blood Cell Phase Images

Image segmentation is defined as partitioning an image into different regions which have similar texture, intensity values, or color. Image segmentation as a preprocessing step is imperative for the analysis of object in a higher level such as image classification, recognition, and tracking [58]. Because of the unnecessary background noise in the computational holographic RBC image, it is also necessary to perform holographic image segmentation algorithm to extract the RBC target which would be used for assessing hematological functions and the presence of disease of RBC. A brief review of segmentation approach is viewed and the segmentation results of RBCs phase images are presented.

3.1.1 Review of Image Segmentation Algorithms

Image segmentation algorithms are useful in the area of medical image analysis, computer vision, object recognition, tracking, and motion analysis [59-60]. Till now, a lot of image segmentation approaches have been proposed

but no one of them can satisfy with the segmentation requirement for all kinds of images. Here, the image segmentation methods are classified into five groups. They are region-based, edge-based, clustering-based, deformable contour model-based, and graph-based segmentation schemes. The most typical and used segmentation algorithms for each category are introduced.

3.1.1.1 Region-based Segmentation

The conventional region-based segmentation methods consists of thresholding, region growing, region splitting and merging.

Thresholding is the simplest and fast algorithm in image segmentation. The grouping of each pixel point belonging to object or background is based on the comparison between pixel intensity value and the given threshold. For instance, f(x,y) is the pixel point value at location of (x,y) in image. It is classified as object if f(x,y)>T while it is viewed as background if f(x,y)≤T where T is the threshold value. This process can be described as following equation:

$$g(x,y) = \begin{cases} 1 & \text{if } f(x,y) > T \\ 0 & \text{if } f(x,y) \leq T \end{cases} \tag{2}$$

where g(x,y) is the segmented image, f(x,y) is the intensity value at (x,y) in the original image, and T is a given threshold. If more threshold values are used, Equation (2) can be extended into multiple thresholding segmentation. For threshold-based method, the choice of threshold is very important. The threshold value can be manually selected or automatically acquired from the analysis of histogram or intensity values of image, such as Otsu's method that can automatically find a threshold maximizing the variance of inter-regions [59].

For region growing segmentation method [59], some seeds representing extracted targets should be selected in advance. Starting from these seed points, neighboring pixel points can be recruited if they are similar with them (similar means similar intensity value). Otherwise, the neighboring pixel is viewed as new seed and used to recruit it's around pixel points. Consequently, the region

connected to the seed points can be grown. The segmentation results of this method are sensitive to the definition of similarity between seed points and their neighboring ones. Also, this method will make the segmentation boundary unsmooth.

For region splitting and merging [59], the original image is first subdivided into some arbitrary, disjointed areas. Then, these small areas are merged or splitted so as to satisfy with the prerequisite conditions. That is, the pixel points belonging to the same region should have similar properties. The traditional region splitting and merging method is described as following steps:

step 1: split the image into four disjoint parts.

step 2: merge any adjacent regions that reach the requirement to be one region.

step 3: iteratively split the sub-region and merge neighboring regions until no further merging or splitting is possible.

The region splitting and merging segmentation approach is sensitive to the splitting and merging condition, and the segmented edge of target will be also unsmooth as region growing segmentation algorithm.

3.1.1.2 Edge-based Segmentation

Edge detection method can find discontinuities in image with first or second-order derivative and the discontinuities always correspond to object edge. Edge detection methods include Sobel, Prewitt, Roberts, Laplacian of a Gaussian, and Canny [59]. Since image usually includes many fault edges, direct edge detection method cannot get good segmentation results. Usually, segmentation method based on edge detection is combined with other methods such as morphology operation [61]. Here, one of the most famous edge detection methods-Canny edge detector and one segmentation method-watershed transform algorithm which can be classified as edge-based segmentation approach are introduced.

Canny edge detection is known as optimal edge detector. This method can reduce the error rate, localize the edge well and response only to single edge. The process of Canny edge detection can be described as following steps:

step 1: smooth the original image with Gaussian filter so as to reduce noise in the image.

step 2: obtain the edge strength with any one of the gradient operators such as Sobel, Roberts, and Rprewitt.

step 3: suppress non-maxima pixels. It is implemented by checking whether the point gradient is greater than its two neighbors along the gradient direction. If so, it means this point may be the edge point and thus the corresponding value is kept. Otherwise, the value is set to be zero.

step 4: using two thresholds ($T_1 < T_2$) to threshold the previous result. The bigger threshold value can reserve apparent edges while the smaller one can keep the week edges.

step 5: connect edge segments in thresholded image obtained with threshold value of T_2 with edge segments that result from segmented image by using threshold value of T_1. When the edge segments result from threshold value T_1 can link the edge segments obtained from threshold value T_2, then these edge segments from T_1 are used to form the final edge by combining with the edge segments from threshold value of T_2.

Watershed transform segmentation is from the flooding simulation [59]. The gray scale image is regarded as topological surface and the regional minimal values are taken as valleys while regional maximal values are viewed as peaks. When water emits from the valleys, dams are built so as to prevent water in valleys from merging together. That is, the watershed transform can find peak value between two neighboring valleys. The flooding simulation of watershed transform algorithm is illustrated in Figure 2 with one dimension. Usually, watershed transform is applied to gradient image since the edge having high gradient corresponds to the peaks. The implementation of watershed transform

can be found in [62]. Since there are many regional minimum and maximum values in original image, it is easy to produce over-segmentation problem when the watershed transform is applied to image directly. In order to solve this problem, marker-controlled watershed transform algorithm is proposed. In this algorithm, the regional minimum values only happen at the locations that are marked. These makers consist of internal and external makers. Internal makers usually denote the extracted targets while the external markers represent the connected background.

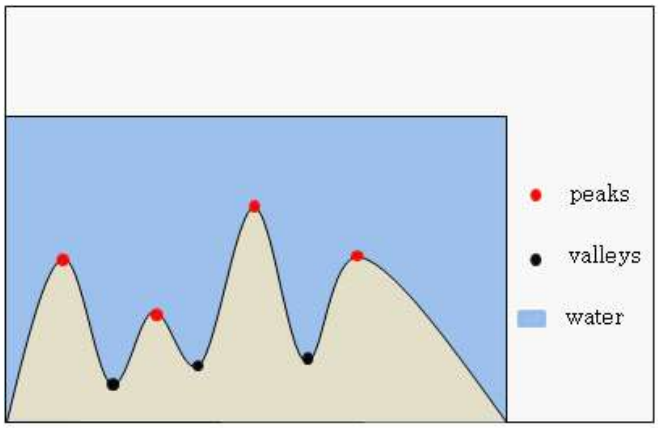

Fig. 2 Illustration of watershed transform algorithm

3.1.1.3 Clustering-based Segmentation

Clustering-based segmentation algorithms assume that the same object would have similar intensity values. Supervised and unsupervised clustering methods [63] which include hierarchical clustering, partitional clustering, k-means clustering, and fuzzy clustering methods can be used for image segmentation. Here, the k-means clustering and mean shift segmentation method which is also regarded as partitional clustering approach are briefly introduced.

For k-means clustering method, the number of cluster has to be defined before applying it to image. K-means method tries to minimize a within-cluster

sum of squares. Namely, attempt to minimize the following term [64]:

$$\arg\min_{s} \sum_{i=1}^{k} \sum_{x_j \in S_i} D^2(x_j, \mu_i) \tag{3}$$

where k is the cluster number, S_i is the set of the ith cluster and μ_i is the mean value of the ith cluster, $D^2(x_j, \mu_i)$ is the distance between a pixel point value and the mean value μ_i of the ith cluster. The procedure for minimizing formula 3 is described as following procedures:

step 1: define the number of cluster k.

step 2: randomly choose k points from the observations/pixel points as centroid points.

step 3: group each point to one of the k clusters by comparing the similarity between the point and the k centroid points. The comparing point is classified into the group with the most similarity. This step will be conducted to all of the observation points.

step 4: update the centroid points with the previous result and then do step 3. The last two steps will be repeated until the centroid points are converged.

When the k-means clustering method is applied to image segmentation, the number of object should be known and the values of pixel point within each object should be similar.

Mean shift [65-67] is a kind of gradient ascent segmentation method. Firstly, the image data should be transformed into probability density by using kernel density estimation [66-67].The density obtained by kernel estimation is much smoother than that from histogram. Then, mean shift algorithm is applied to each point on the density where the mean shift vector will point to the gradient. Consequently, each point will converge to the closest mode where the mode is considered as a cluster center. Thus, the points that share the same mode are regards as the same cluster belonging to the same object. The segmentation procedure of mean shift algorithm is given as following steps.

step 1: estimate density of image with kernel density estimator as following equation:

$$\tilde{f}(x) = \frac{1}{nh^d} \sum_{i=1}^{n} K\left(\frac{x - x_i}{h}\right) \tag{4}$$

when the spatial (image lattice) and range (graph level or color of spectral information) domains are considered, K(x) can be expressed as follows.

$$K(x) = ([x^s \ y^r]) = \frac{c}{h_s^d \, h_r^p} k\left(\left\| \frac{x^s}{h_s} \right\|^s \right) k\left(\left\| \frac{y^r}{h_r} \right\|^2 \right) \tag{5}$$

where k(x) is epanechnikov kernel function, h is the size of moving window, d and p are dimension number while c is used to normalize the function of K(x).

step 2: for each image pixel x_i , initialize $y_{i,1} = x_i$ and then apply mean shift algorithm to it until convergence. The new point resulting from x_i by using mean shift algorithm is derived as following iteration equation.

$$y_{i,j+1} = \sum_{i=1}^{n} x_i g\left(\left\| \frac{y_{i,j} - x_i}{h} \right\|^2 \right) / \sum_{i=1}^{n} g\left(\left\| \frac{y_{i,j} - x_i}{h} \right\|^2 \right) \tag{6}$$

where g(x)=k′(x), n is the number of samples (pixel points) within the moving window.

step 3: update the pixel value of x_i as $z_i = (x_i^s, y_{i_{con}}^y)$. That is, the value of pixel point at location x_i^s is assigned with the converged feature point $y_{i_{con}}^y$ which is the mode in the probability density. As a result, pixel points with the same mode are viewed as the same cluster and belong to the same object.

The above three steps are the fundamental procedures for image segmentation with mean shift algorithm. However, it is also easy produce over-segmentation problem. For better segmentation performance, more procedures such as merging smaller regions should be included.

3.1.1.4 Deformable Contour Model-based Segmentation

There are two kinds of deformable contour model-based segmentation method [68-69]. They are parametric model and geometric deformable mode. The former is usually referred to as snake and the latter one as level set. The contour in a

parametric model is propagated directly on the image which means the points on the curve is parameterized and evolved explicitly while the evolution of contour on the level set is independent to any parameterization and the curve is propagated implicitly by evolving a surface in a high dimension. The basic concept about snake and level set are described as follows.

The curve in snake model is defined as $v(s)=[x(s),y(s)]$ where x(s) and y(s) are x and y coordinates in image and $s\in[0,1]$ are points on the snake. The segmentation is achieved by minimizing an energy function on the snake which is expressed as follows [69-70]:

$$E_{snake}=\int_0^1 E_{snake}(v(s))ds \tag{7}$$

$$=\int_0^1 (E_{cur}(v(s))+E_{img}(v(s))+E_{con}(v(s)))$$

where E_{cur} is the internal energy due to bending of curve, E_{img} is energy from image force and E_{con} is energy from external constraint forces defined by user. The internal and image energy can be simpled expressed as following equations for image segmentation.

$$E_{cur}=\alpha(s)\left|\frac{dv}{ds}\right|^2+\beta(s)\left|\frac{d^2v}{ds^2}\right|^2 \tag{8}$$

$$E_{img}=-|\nabla f(x,y)| \tag{9}$$

where $\alpha(s)$ and $\beta(s)$ specify the elasticity and stiffness of the snake, $\nabla f(x,y)$ is the image gradient. When calculus of variation [] is applied to the functional in equation 7, the Euler-Lagrange condition can be derived as follows.

$$\nabla E_{ext}(v)-\frac{d}{ds}\alpha\frac{dv}{ds}+\frac{d^2}{ds^2}\beta\frac{d^2v}{ds^2}=0 \tag{10}$$

where $E_{ext}=E_{img}+E_{con}$. Then, the evolution equation can be formed as equation 11.

$$v(s,t+1)= \left(\frac{d}{ds}\alpha\frac{dv(s,t)}{ds}-\frac{d^2}{ds^2}\beta\frac{d^2v(s,t)}{ds^2}-\nabla E_{ext}(v(s,t))\right)\times\Delta t+v(s,t) \tag{11}$$

However, the implementation is easy to suffer from numerical instability and

numerous parameters have to be designed. Many kinds of varied snakes can be found in [71-73].

The snakes cannot properly deal with split and merge problem during image segmentation while level set can solve those disadvantages. As level set [74-75], the curve X(s,t) is embedded into a level set function $\Phi(x,y,t)$ and the curve is obtained by determining zero level set in the level set function. Consequently, the curve can be obtained by evolving the level set function and be chosen as the zero level set instead of evolving the curve explicitly. The embedded curve in level set can be described as following equation [68].

$$\Phi(X(s,t),t)=0 \tag{12}$$

use chain rule and do differential to Equation 12 with respect to t, the following equation can be achieved:

$$\frac{\partial \Phi}{\partial t}+\nabla \Phi \frac{\partial X}{\partial t}=0 \tag{13}$$

when the speed of the curve $\partial X/\partial t = V(c)N$ and the inward unit normal of level set curve $N=-\nabla\Phi/|\nabla\Phi|$ is inserted into Equation 13, the curve evolution using the level set method can be described as follows:

$$\frac{\partial \Phi}{\partial t}= V(c)|\nabla \Phi| \tag{14}$$

where V(c) is the speed function. The basic speed function from image can be written as $1/(1+|\nabla(G_\sigma * I)|)$ where $\nabla(G_\sigma * I)$ denotes the gradient of smoothed image with Gaussian filter. As implementation, an initial level set function that the curve has zero level set should be defined. Since Equation 14 is defined only for zero-level set, other level sets also need to be defined for implementation. A large number of varied level set methods can be found in [76-81].

3.1.1.5 Graph-based Segmentation

The snake and level set segmentation method can be also classified as

energy-based segmentation algorithm. These methods cannot reach global minimum energy during function minimization. Here, only the graph cut segmentation approach [82-85] which try to minimize an energy function with graph cut and can achieve global minimum value is focused.

A graph denoted as G=<V,E> includes node and weight. The cut is the total weight of edges that have been removed between two groups resulted from a cut in the graph. Image segmentation based on graph cut is to find the minimum cut which can reach minimum energy. The energy for graph cut segmentation is defined as following equation [82-83].

$$E(A) = \lambda R(A) + B(A) \tag{15}$$

where R(A) and B(A) are defined as:

$$R(A) = \sum_{p \in P} R_p(A_p) \tag{16}$$

$$B(A) = \sum_{p \in P} \sum_{p,q \in N} B_{p,q} \delta(A_p, A_q) \tag{17}$$

$$where \;\; \delta(A_p, A_q) = \begin{matrix} 1 & A_p \neq A_q \\ 0 & A_p = A_q \end{matrix}$$

where R(A) is called as regional term and defines the penalties for assigning A_p (pixel point p on image) to object or background which can be denoted as $R_p('obj')$ and $R_p('bkg')$, B(A) is the boundary term which describes the boundary properties of the segmentation, λ is the relative importance factor between regional and boundary term. The energy function in Equation 15 can be minimized by the graph cut theory while the cut is the segmentation boundary. To get segmentation result, the graph should be established first by using the original image. Then, the minimum cut of the graph can be obtained by max-flow algorithm [59] which can achieve the minimum cut. When the result is not good, the refinement/interactive process can be used. For graph construction, two extra terminal nodes (other nodes that are not from image pixel points) which represent object and background are applied and this kind of graph is called as s-t graph. After the nodes are defined, next step is to give weight to the corresponding edges. The weight can be given as criterion

shown in Table.1 [82-83].

Table. 1 Graph Construction

Edge	Weight	Condition
n-link {p,q}	$B_{\{p,q\}}$	$p,q \in N$
t-link {p,s}	$\lambda R_p('bkg')$	$p \in P,\ p \in O \cup B$
	K	$p \in O$
	0	$p \in B$
t-link {p,t}	$\lambda R_p('obj')$	$p \in P,\ p \in O \cup B$
	0	$p \in O$
		$p \in B$

where n-link is the edge between nodes in image, t-link is the edge between nodes in image and two terminal nodes (s and t nodes), $B_{\{p,q\}}, R_p('bkg')$, K, and $R_p('obj')$ are defined as follows:

$$B_{\{p,q\}} \propto \exp\left(-\frac{(I_p - I_q)^2}{2\sigma^2}\right) \tag{18}$$

$$K = 1 + \max_{p \in P}\left(\sum_{q:\ \{p,q\} \in N} B_{(p,q)}\right) \tag{19}$$

$$R_p('obj') = -\ln \Pr(I_p|O) \tag{20}$$

$$R_p('bkg') = -\ln \Pr(I_p|B) \tag{21}$$

where {p,q} denotes two neighboring nodes in image, $\Pr(I_p|O)$ and $\Pr(I_p|B)$ denote the intensity distribution of object and background which are usually estimated from the seed points that are manually selected or automatically detected. When the weight in graph is assigned as the method showed in Table.1, the min-cut can be achieved by max-flow method and the minimum energy in Equation 15 is achieved while the cut edge is corresponding to the segmentation results. The graph cut segmentation is widely used in interactive segmentation approach.

3.1.2 Segmentation Results of Red Blood Cell Phase Images

Red blood cells of healthy laboratory personnel were obtained from the Laboratoire Suisse d'Analyse Du Dopage, CHUV. The RBCs were stored at $4^{\circ}C$ and DHM measurements were conducted on several days after the blood were drawn from the laboratory personel. 100-150μl of RBC stock solution were suspended in HEPA buffer at 0.2% hematocrit. 4μl of the erythrocyte suspension were diluted to 150μl of HEPA buffer and introduced into the experimental chamber, consisting of two cover slips separated by spacers 1.2 mm thick. Cells were incubated for 30 min at a temperature of $37^{\circ}C$ before mounting the chamber on the DHM stage. All experiments were conducted at room temperature ($22^{\circ}C$).

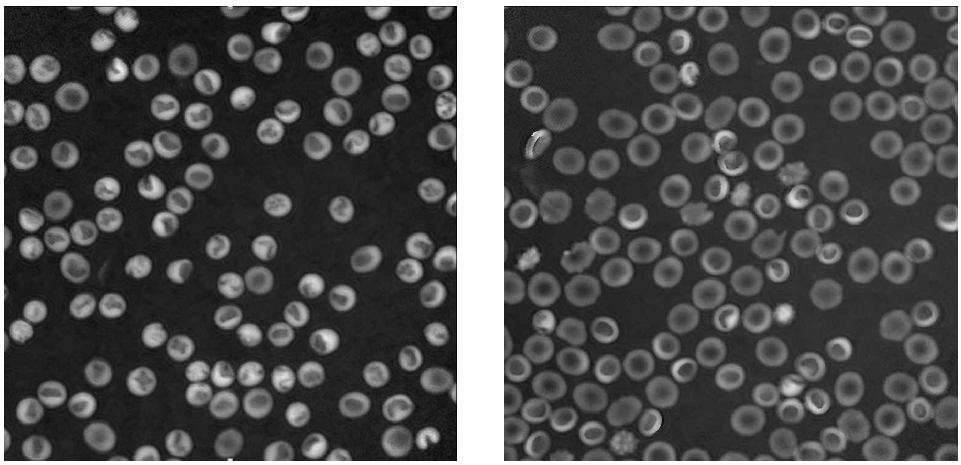

(a) (b)

Fig. 3 Reconstructed RBCs phase images. (a) The RBCs with predominantly stomatocyte shape. (b) The RBCs with predominantly discocyte shape

The RBC phase images are numerically reconstructed from the RBC holograms that are recorded with DHM. Two of the reconstructed RBC phase

images are shown in Figure 3. The Figure 3(a) are reconstructed RBCs phase image with RBCs of predominantly stomatocyte shape and Figure 3(b) are reconstructed RBCs phase image with RBCs of predominantly discocyte shape. By analyzing a series of segmentation methods, the marker-controlled watershed transform segmentation method combined with morphological operation is applied to remove the unnecessary background existed in RBCs phase image due to its advantage in terms of getting isolated target. The detail procedures for segmenting RBCs phase images with marker-controlled watershed transform can be found in [37]. Consequently, each RBC can be separately extracted and the corresponding features can be measured for the further analysis. Two of the segmented RBCs phase images are given in Figure 4.

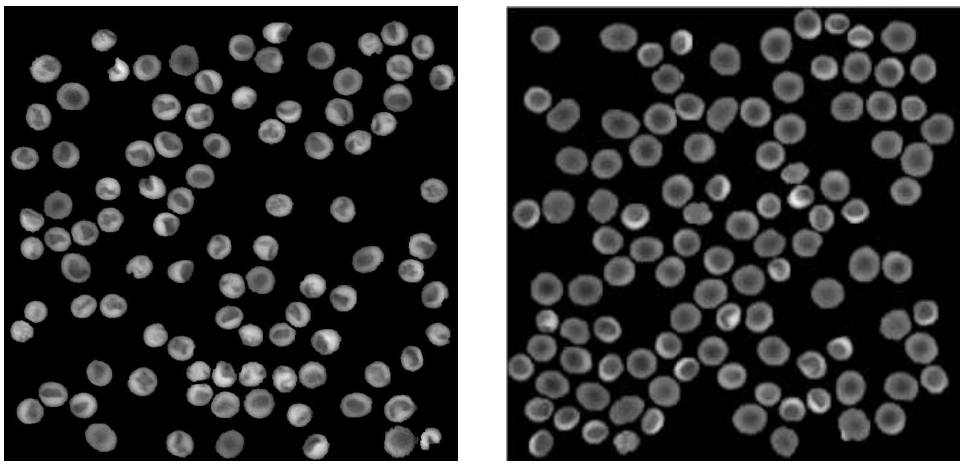

(a) (b)

Fig. 4 The segmented RBCs phase image. (a) The segmented RBCs of Fig.3(a) (b) The segmented RBCs of Fig.3(b).

Moreover, the inside part of RBCs are also helpful for the analysis of RBC-related disease. It is meaningful to extract the inner part of RBCs as well. The marker-controlled watershed transform method can also be used to segment the inside area of RBCs based on the segmented RBCs phase images shown in Figure 4. Consequently, it is easy to derive the outer part of RBCs

once the inner parts are obtained. The segmentation results of inner and outer part of RBCs are given in Figure 5 [37].

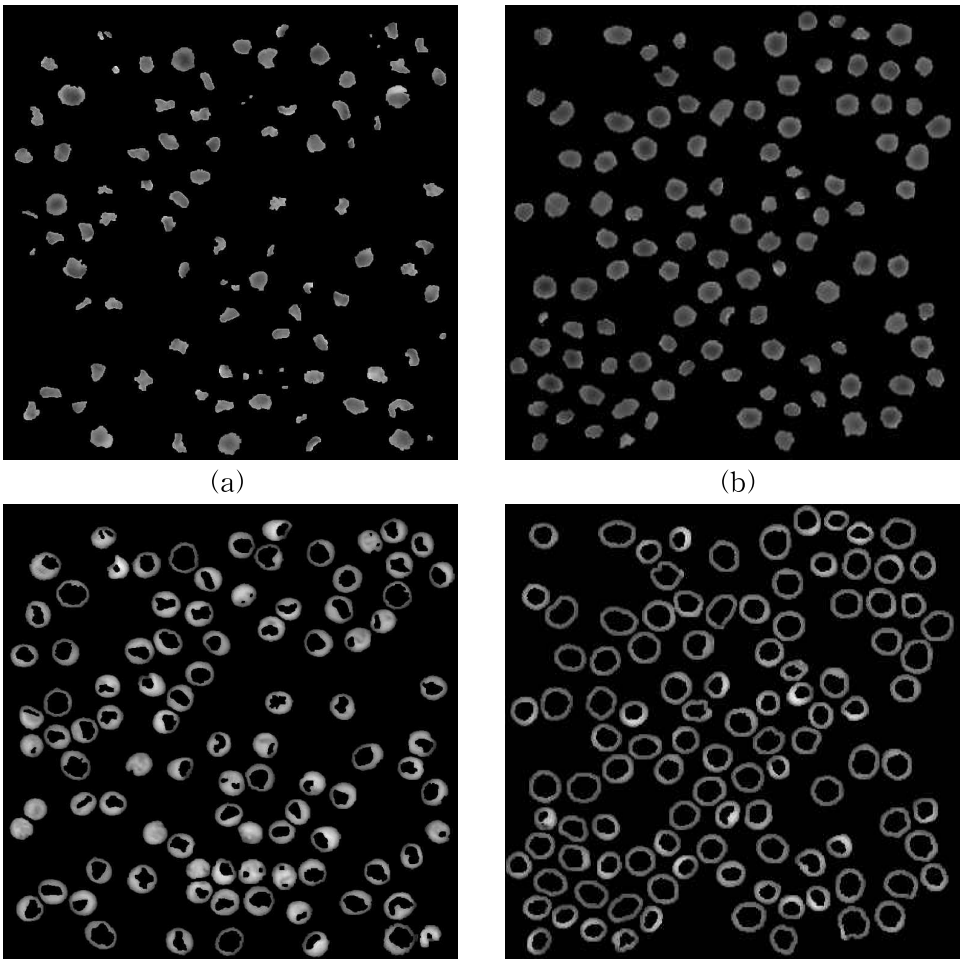

Fig. 5 Segmentation results of the inner and outer parts of the RBC phase images. (a) and (b) are the inner part of RBCs in Fig. 4(a) and (b). (c) and (d) are the outer part of the RBCs in Fig. 4(a) and (b).

It is noted from Figure 4 and Figure 5 that the marker-controlled watershed transform segmentation method combined with morphological operation can segment the RBCs phase image properly, not only robust to the whole RBCs

but also to the inner and outer part of the RBCs. This segmentation method can be used to segment the RBCs phase images and do the further analysis about RBCs.

3.1.3 Performance Comparison and Evaluation

The segmentation results about RBCs with predominantly stomatocyte and discocyte shape are compared and evaluated. These RBCs segmented with conventional marker-controlled watershed algorithm in [59] are given in Figure 6. It is noted from Figure 4 and Figure 6 that our method can get much better segmentation results in terms of over-segmentation and under-segmentation.

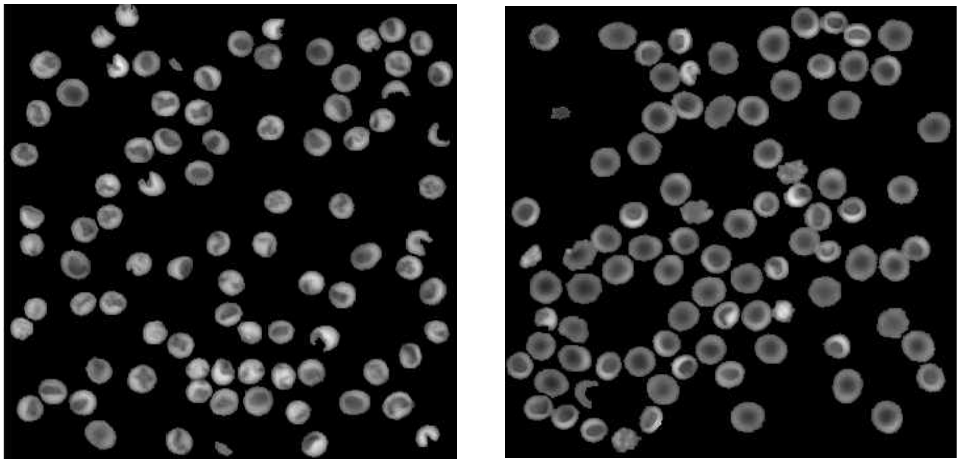

(a) (b)

Fig. 6. The segmented RBCs with marker-controlled watershed method in [59]. (a) The segmented RBCs of Fig. 3(a) (b) The segmented RBCs of Fig. 3(b).

Moreover, a scientific tool developed by F. Sadjadi [103], which is based on the experimental design methodology and independent of the systems output has been applied for performance evaluation. The performance comparison of two algorithms with biased results is mainly dependent on the varied parameters in

segmentation. The procedure of the performance evaluation approach can be briefly described as steps of data characterization, data sampling, primary parameter selection, parameter sampling, performance metrics definition, performance model calculation and statistical analysis. The quantitative phases of RBCs in this study are given to two categories namely stomatocyte and discocyte shape RBCs. The primary parameter which largely affects the segmentation result in our procedure is the value of threshold obtained by Otsu's method while the main parameter for the marker-controlled watershed in [59] is also a threshold which is used to find the regional minimum values. The assessment of segmentation results for RBC inner and outer parts are not conducted because they heavily rely on the previous segmentation results. For the performance metrics, the segmentation accuracy is adopted and it is simply defined as the absolute value of correlation between segmented RBCs image and reference image which is manually obtained. The closer the segmented image is to the reference image, the closer the segmentation accuracy will tend to approach 1.

The homologous performance models between segmentation accuracy and threshold for RBCs with stomatocyte and discocyte shape are presented in Figure 7. For curve fitting, the least square error estimation technique was employed and the polynomials were examined with degrees up to 6. Then, statistical analysis of Chi-squared test was performed for checking of the similarity between the obtained results (the measured data with the segmentation method and that in the fitted polynomial) [103]. Consequently, the p-values for the null hypothesis that the predictive performance models approximately satisfy with the measured response curve were achieved to be 0.7578, 0.3571, 0.9135 and 0.1213 for Figure 7(a), (b), (c) and (d) respectively. Therefore, the null hypothesis that the fitting curve is similar with the measured one should be accepted at the 0.05 level of significance. It is also noted that the maximum segmentation accuracy in our method outperforms that presented in [59].

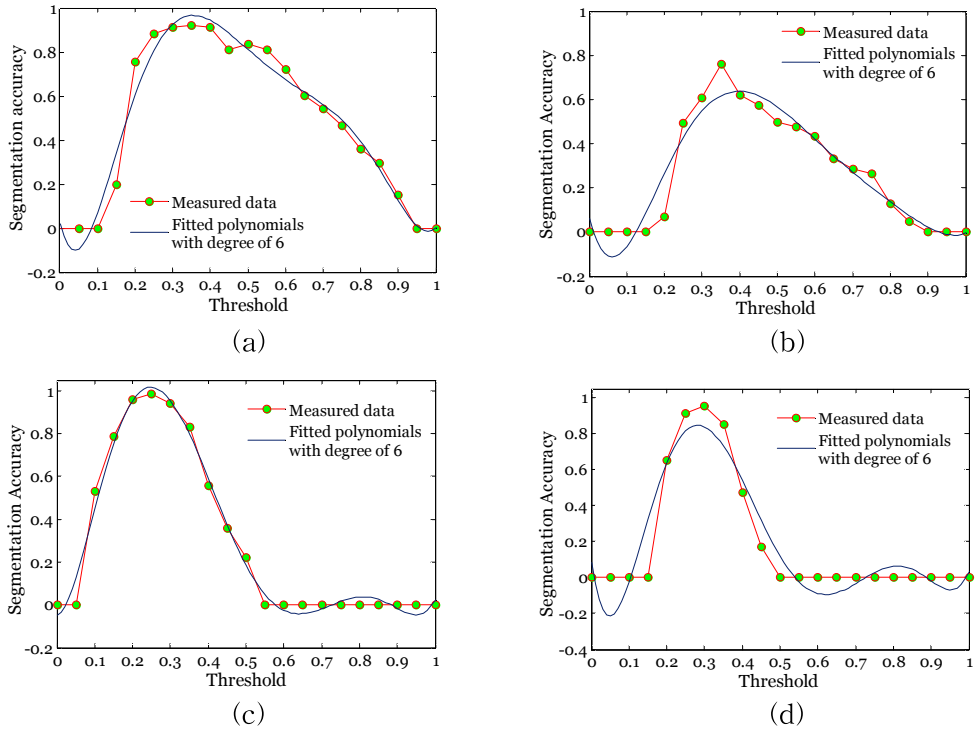

Fig. 7 Performance models. (a) and (b) are performance models for RBCs with stomatocyte and discocyte shape in the method of [59]. (c) and (d) are performance models for RBCs with stomatocyte and discocyte shape in our proposed procedure.

3.1.4 Subsection Summaries

In summary, all of the segmentation methods can work well for image that the target is very different from the background and the intensity values of the pixel points of the same region are very similar. Among these segmentation approaches, thershold-based method has the advantage of fast computation time. However, it is difficult to choose an appropriate threshold. Region growing, region splitting and merging method can get better segmentation results when the property of target is very similar. This kind of method suffers from unsmooth boundary and is not easy to define the stop criterion. In addition, this

method is not good for segmented targets with weak boundary. As edge-based segmentation algorithms, the most used methods such as Sobel, Prewitt, Roberts, Laplacian of a Gaussian and Canny will work well when they are combined with other post-processing techniques such as morphology operation. It is also easy for these methods to produce false edges due to image noise. For watershed transform segmentation algorithm, it has the advantage to get isolated object and disadvantage of producing over-segmentation. However, when the object can be approximately detected, the marker-controlled watershed algorithm will work well and can reduce the over-segmentation problem. Usually, the segmentation results are not good when the edge-based method is used solely. For clustering-based segmentation, assumption that each region should have similar property is required. This kind of method is also robust to color image. After clustering the pixel point, post processing such as merging small region is necessary. Snakes and level set segmentation method can be applied to medical image with heavy noise and weak edge in object. Compared with snakes, level set algorithm can solve the split and merge problem during the curve evolution. These kinds of methods are widely used in biomedical images. For the graph cut segmentation method, the regional and boundary information on image are combined. The graph cut can work well when different targets are existed in image. The graph cut method can get appropriate segmentation results to all kinds of image when the user's intervention is introduced. All kinds of segmentation methods have many improved version which can reach an acceptant execution time. For the segmentation of RBCs phase images, the RBCs phase images are segmented by using marker-controlled watershed transform algorithm due to its advantages of achieving isolated object while the internal and external markers are identified with morphological operation and thresholding technique. Moreover, the execution time of watershed transform algorithm is acceptable compared with active contour and graph-based segmentation approaches.

3.2 Quantitative Analysis of Human Red Blood Cells Stored in Different Periods

In this section, the modifications of the 3D morphology and mean hemoglobin (MCH) in RBCs induced by the length of storage time for the purpose of 3D classification of RBCs having different storage periods by using an off-axis DHM is studied. To analyze the morphological changes in RBCs induced by the length of storage time, datasets from blood samples stored for 8, 13, 16, 23, 27, 30, 34, 37, 40, 47, and 57 days are used, respectively. The datasets are divided into eleven classes of RBCs stored in eleven different periods. The eleven classes have more than 3,300 blood cells, with averagely more than 300 blood cells per class. The classes indicate the storage period of RBCs and are listed in chronological order. Using the RBCs donated by healthy persons, off-axis digital holographic microscopy reconstructs several RBC quantitative phase images from each class of blood sample. In order to automatically calculate the characteristic properties such as projected surface area, averaged phase value, corpuscular volume, hemoglobin content and hemoglobin surface density of RBCs, the image segmentation method [37] based on marker-controlled watershed algorithm [59] is applied to remove the unnecessary background in the RBC quantitative phase image. All the RBCs that exist in the quantitative phase image are extracted to measure the characteristic properties of RBCs. Averagely, more than 300 RBCs are extracted from the segmented quantitative phase images for each class of blood sample. The sample size is large enough to allow us to obtain statistical distributions of the characteristic properties of RBCs at a specific storage time. Our main focus is to quantitatively analyze the relationship between the RBC characteristic properties and their aging. This analysis will be beneficial to the understanding of the features of RBCs with different storage periods and evaluation of any modifications in the 3D cell morphology and hemoglobin content induced by the length of storage time.

3.2.1 Sample Preparation

The original RBC's were donated by healthy people and stored in a transfusion bag which were obtained from the Service Régional Vaudois de Transfusion Sanguine in Switzerland and stored at 4°C during the storage period. The erythrocyte concentrate was extracted from the blood transfusion bag and diluted in HEPA buffer (15 mM HEPES pH 7.4, 130 mM NaCl, 5.4 mM KCl, 10 mM glucose, 1 mM CaCl2, 0.5 mM MgCl2 and 1 mg/ml bovine serum albumin) at a concentration of ~ 0.15 % Vol. 0.2 ml of the erythrocyte suspension was then introduced into the experimental chamber, consisting of two coverslips separated by spacers 1.2 mm thick. In order to allow for sedimentation of the cells on the bottom coverslip, cells were incubated for 30 min at a temperature of 37°C before mounting the chamber on the DHM stage. All experiments were conducted at room temperature.

3.2.2 Three-dimensional Sensing and Segmentation of Red Blood Cells

To analyze morphological changes in RBCs induced by the length of storage time, eleven classes of blood samples stored for 8, 13, 16, 23, 27, 30, 34, 37, 40, 47, and 57 days were prepared. The off-axis DHM reconstructed several RBC quantitative phase images for each class of blood samples, where holograms of RBC preparations were acquired in an out-of-focus plane. In-focus phase images of RBCs were obtained through a numerical reconstruction of the object wavefront and subsequent digital propagation of the reconstructed field to the focus plane. Most of the contained RBCs are discocyte RBCs which have a discoid-shape. Some of the reconstructed RBCs phase images are given in Figure 6 [86].

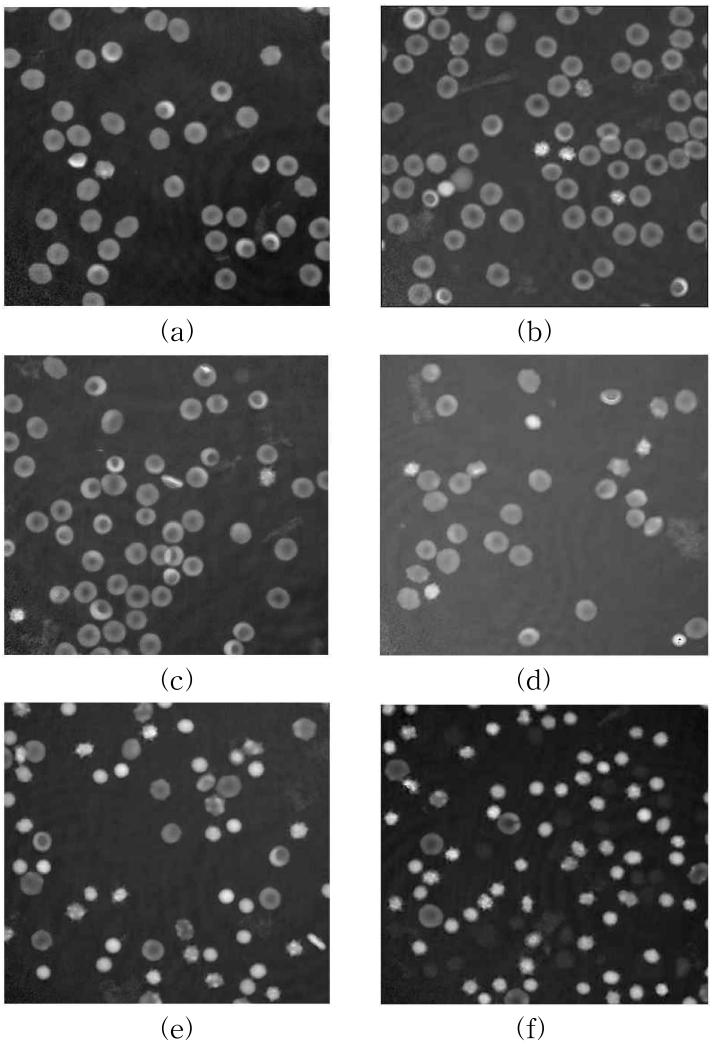

Fig. 8 Reconstructed RBCs images at different storage days. (a)-(f) are RBCs with 8, 16, 30, 34, 47 and 57 days of storage, respectively.

For automated investigation of the characteristic properties of RBCs, individual RBC must be extracted from the quantitative phase image. The segmentation method based on marker-controlled watershed algorithm as described in section 3.1 is applied to remove the background from the quantitative phase images. For the purpose of comparing the RBC quantitative phase images with different storage times, the phase value of the background of

the RBC quantitative phase image is set to 0°. The corresponding segmentation results for RBCs phase images shown in Figure 8 are given in Figure 9.

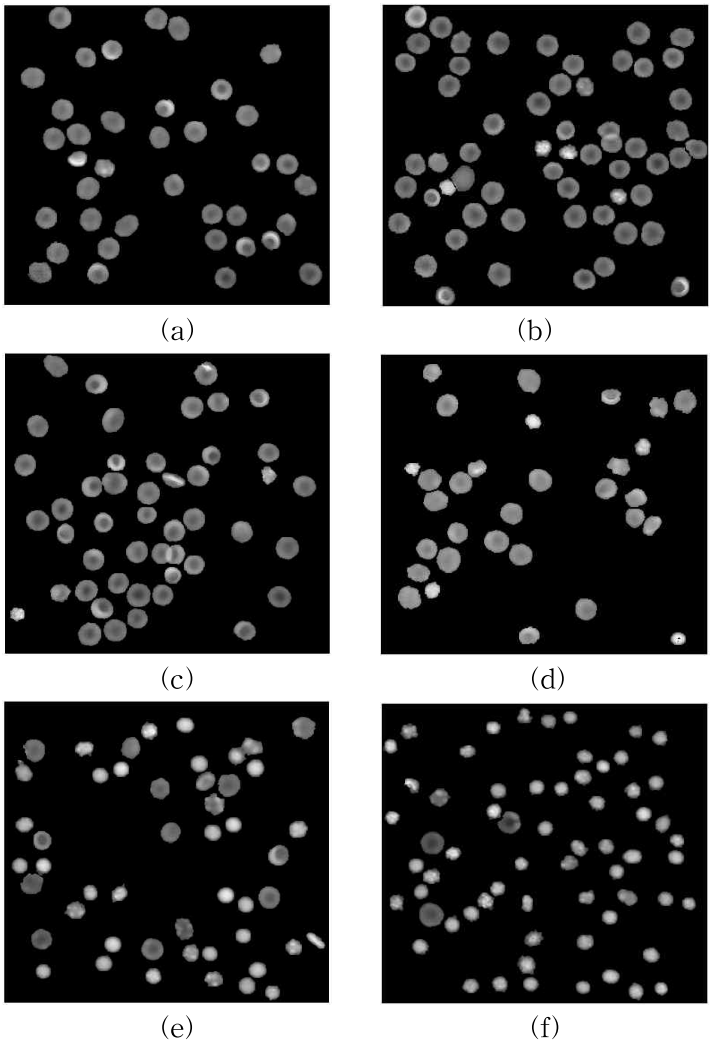

Fig. 9 Segmentation results of Reconstructed RBCs images at different storage days. (a)-(f) are the corresponding segmented RBCs images shown in Fig.6 (a)-(f) with 8, 16, 30, 34, 47 and 57 days of storage, respectively.

3.2.3 Measurement of Red Blood Cells Features

The characteristic properties used to analyze the 3D morphological changes in RBCs induced by the length of storage time are the projected surface area, the mean phase value allowing to calculate mean corpuscular volume (MCV), hemoglobin (MCH) – the average volume and mass of hemoglobin per red blood cell in a sample of blood – and MCH surface density (MCHSD), defined as the ratio of MCH to the projected surface, three highly relevant parameters, altered in various pathological states.

The average phase value Φ induced by the whole RBC which is related to the dry mass [87] and the projected surface area S which may influence the functionality of RBCs are defined as follows:

$$\Phi = \frac{1}{N}\sum_{i=1}^{N}\varphi_i \tag{22}$$

$$S = Np^2 \tag{23}$$

where N is the total number of pixels within a RBC, p denotes the pixel size in the quantitative phase image, and φ_i is the phase value of each pixel within the RBC. RBC volume or the size of RBC is a good indicator of the functionality of RBCs. A RBC with a larger volume means a larger surface area and thus can transform more oxygen [88]. It is also beneficial to the diagnosis of polycythemia vera [89]. According to [87], the volume of a single RBC, or the corpuscular volume is denoted as:

$$V \cong \frac{p^2\lambda\sum_{i}^{N}\varphi_i}{2\pi(n_{rbc}-n_m)}, \tag{24}$$

where p is the pixel size in quantitative phase image, φ_i is the phase value of each pixel within the RBC, and λ is the wavelength of the light source. Coherently, when a population of RBCs is considered, Equation. (24) allows us to derive the mean corpuscular volume (MCV) [90]. The refractive index of RBCs, nrbc, has been measured with a dual-wavelength digital holographic

microscope as described in [91]. Here, nrbc, is 1.396 with no significant difference between groups of different ages. The index of refraction of the HEPA medium, nm, is 1.3334. Another important characteristic property is the dry mass which measures the weight of the cell after dehydration. The dry mass is a reliable biomass, which is widely used to compare cells since it is free from the disturbance of water existing in living beings [87]. According to [87, 92], the dry mass of a cell is related to the phase value and can be defined as follows:

$$Dry\ Mass(DM) = \frac{10\lambda}{2\pi\alpha}\int_s \varphi ds = \frac{10\lambda}{2\pi\alpha}\Phi S, \tag{25}$$

where λ is the wavelength of the light source, Φ is the average phase value induced by the whole cell, α is a constant known as the specific refraction increment (in m3/kgordl/g) related mainly to the protein concentration [29]. As far as RBCs are concerned, $\alpha = \alpha_{Hb} = 0.00196$dl/g is the hemoglobin refraction increment between 663nm and 682nm [90]. When a RBC population is considered Equation. (25) provides the mean corpuscular hemoglobin (MCH) according to [92]. The MCH is used as an important parameter for the investigation of change in the hemoglobin content in the RBCs.

The last property used to evaluate the morphological changes in RBC induced by the length of storage time is the MCH surface density (MCHSD), which can show the hemoglobin concentration. It is defined as the ratio between MCH and projected surface area S as follows:

$$MCHSD = \frac{MCH}{S} \tag{26}$$

All the properties defined as in the above equations can be appropriately calculated and compared by using the segmented RBCs phase images stored at different periods.

3.2.4 Experimental Results and Discussion

After segmentation and extraction of RBCs from the quantitative phase images, the characteristic properties including the mean projected surface area $\overline{S}$, the mean average phase value $\overline{\Phi}$, MCV, MCH and MCHSD as well as their standard deviation were calculated for each class of blood sample with method of moments [34]. In the same way, the mean and standard deviation of the projected surface area for RBCs with different storage periods can be calculated. The other properties of RBCs including corpuscular volume (CV) hemoglobin (CH) and hemoglobin surface density (CHSD) can also be obtained by the method of moments. Table 2 shows the calculated mean and standard deviation for all of the characteristic properties of RBCs with different storage times [86].

Table. 2 Characteristic properties of RBCs with different storage days

storage time[days]		8	13	16	23	27	30	34	37	40	47	57
projected area	mean	45	46	47	45	47	42	43	41	39	34	26
	std	5	6	7	7	10	8	9	8	9	9	6
Mean phase value	mean	74	74	81	76	77	76	78	87	96	112	136
	std	12	15	16	16	15	24	21	26	27	28	28
CV	mean	91	92	102	94	98	88	86	93	98	98	94
	std	9	12	14	14	15	20	12	11	12	13	11
CH	mean	32.2	32.3	35.7	32.8	34.8	29.2	30.9	32.7	33.6	34.6	32.5
	std	5.0	5.5	7.7	7.3	8.6	7.6	6.1	5.7	5.0	6.8	5.1
CH surface density	mean	0.70	0.70	0.76	0.71	0.72	0.71	0.73	0.82	0.90	1.05	1.28
	std	0.11	0.13	0.14	0.15	0.14	0.23	0.20	0.24	0.25	0.26	0.26

All of the property values are measured automatically once the RBC phase images are successfully segmented. It can be seen from Table.2 that the mean phase value and CH surface density have similar variation tendency that tend to increase as the increase of storage time. For CV and CH, they don't change quickly as the extension of storage time and seem to fluctuate around their

respective mean value. In contrast, the RBC projected area is obviously decreased as the increase of storage days. On the other hand, the standard deviations for all of these properties achieve significant value when the RBCs storage time is around 30 days (27-34days). Around 30 days' storage, the standard deviations of projected area, CV and CH achieve big value. As RBCs mean phase value and CH surface density, the standard deviations are inclined to increase at the time with 30 storage days. These phenomena may be explained that the RBCs are suffering from drastic variation when the stored days are around 30 days.

In order to view the trend of the modification of the 3D morphology of RBCs as a function of storage time, the mean and standard deviation are plotted against storage time.

Figure 10 presents the relationship between the mean projected surface area, mean average phase value and the varied storage time of RBC samples. It was discovered that the variation trends of RBC projected surface area and the average phase value are almost opposite as the increase of storage days.

Figure 10(a) shows the relationship between the mean projected surface area $\overline{S}$ and storage time. Roughly, the trend of $\overline{S}$ of RBCs decreases with increasing storage time. As shown in Figure 10(a), it is noted that when the storage time of RBCs is less than 27 days, $\overline{S}$ remains quite constant. Furthermore, the decrease rate of $\overline{S}$ for RBCs with storage time less than 34 days is much smaller than that for those with storage time longer than 34 days. When the storage time is longer than 34 days, $\overline{S}$ experiences a substantial decrease. On the other hand, Figure 10(b) shows the relationship between the mean average phase value $\overline{\Phi}$ [see Equation.(22)]and storage time. $\overline{\Phi}$ and its standard deviation are obtained from 300 individual RBCs in each class of blood sample. From Figure 10(b), it can be observed that does not experience a significant change when the storage time is less than around 34 days. In contrast, when the storage time is longer than 34 days, $\overline{\Phi}$ apparently increases. As can be seen

from Figure 10(a) and Figure 10(b), both $\overline{S}$ and $\overline{\Phi}$ remain constant when the storage time is less than around 34 days. However, $\overline{S}$ and $\overline{\Phi}$ change in the opposite directions when the storage time of RBCs is longer than 34 days. Decrease in $\overline{S}$ results in the increasing occurrence of echinocytes in the RBC preparations. RBCs that have aged significantly begin decomposition and have a serrated margin and burr appearance. The RBCs with this morphologic abnormality are called echinocytes.

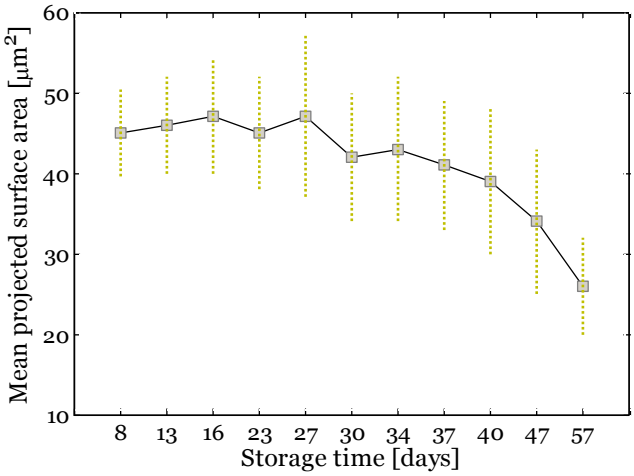

(a)

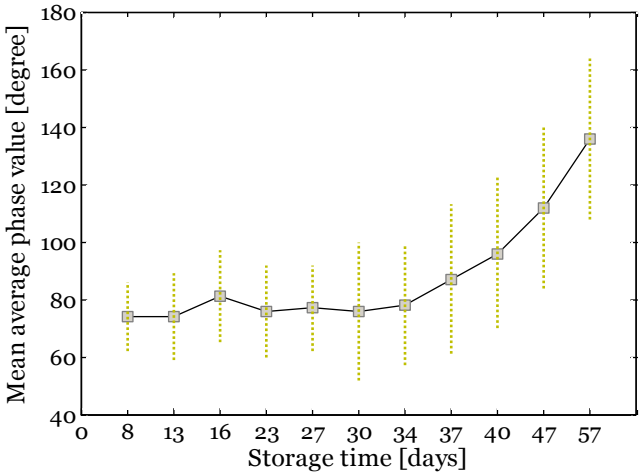

(b)

Fig. 10 Relationship between the mean projected surface areas, mean average phase value and the different storage times. (a) Relationship between S and storage time. (b) Relationship between $\overline{\Phi}$ and storage time. Square and bar are the mean and standard deviation of $\overline{\Phi}$ and S.

Figure 11 illustrates the relationship between RBCs MCV, MCH and the different storage time of RBC samples. The results reveal that the trends for RBCs MCV and MCH with increase storage time are almost the same. In addition, both MCV and MCH values seem to swing around their respective mean value.

Figure 11(a) shows the relationship between the mean corpuscular volume MCV and the storage time. It is noted that the MCV fluctuates around a value of 94 μm^3 even if the storage time of RBCs is increased. Therefore, one conclusion that may be derived is that the MCV is not significantly affected by the storage time. In contrast, Figure 11(b) shows the relationship between the mean corpuscular hemoglobin MCH and RBC storage time. As shown in Figure 11(b), although the MCH fluctuates around a value of 32pg, the MCH is almost stable even if the storage time is increased. Therefore, it may conclude that the hemoglobin content within RBCs does not change as a function of storage time.

Since MCV and nrbc do not vary over storage time, this is an expected result.

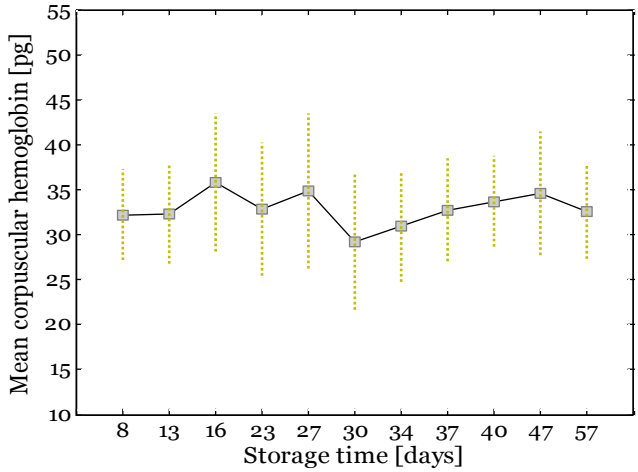

(a)

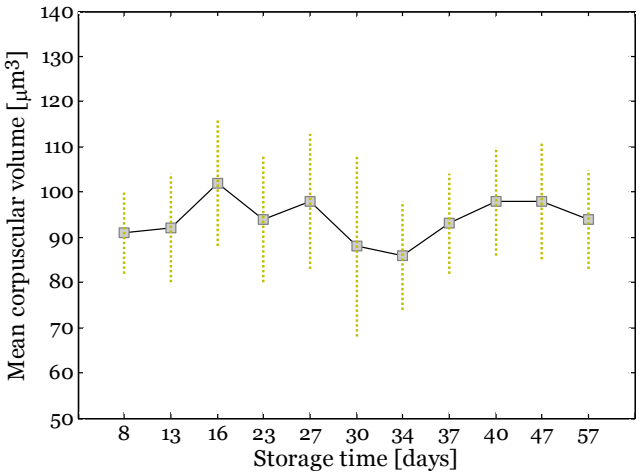

(b)

Fig. 11 Relationship between MCV, MCH of RBCs and varied storage time. (a) Relationship between MCV and storage time. Square is the mean and bar is the standard deviation of corpuscular volume. (b) Relationship between MCH of RBCs and storage time. Square represents the mean and bar represents the standard deviation of the corpuscular hemoglobin content.

Figure 12 shows the relationship between the mean corpuscular hemoglobin surface density MCHSD and storage time. Even though the MCH in Figure

11(b) shows little fluctuations over the storage period, the MCHSD tends to increase as shown in Figure 12. This can be explained by the fact that the MCH remains constant while the mean projected surface area of RBCs tends to decrease with increased storage time. It can also be noted that the MCHSD is almost constant when the storage time of RBCs is less than 34 days. When the storage time is longer than 34 days, the increase in MCHSD is noticeable and the 3D morphological modification of RBC is drastic.

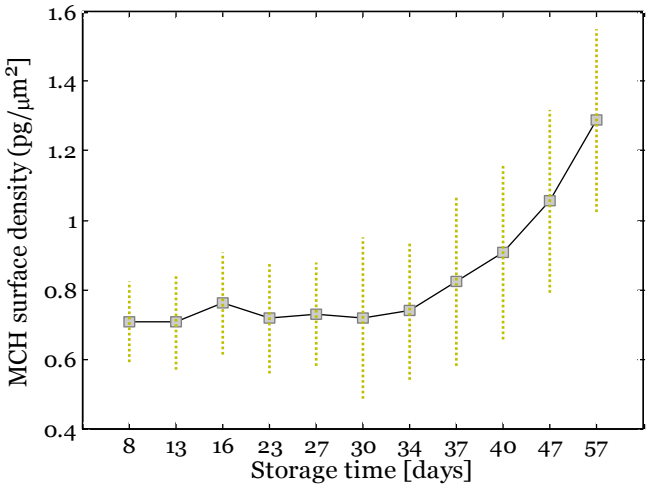

Fig. 12 Relationship between MCHSD of RBCs and varied storage time. Square represents the mean and bar represents the standard deviation of the dry mass surface density.

From the relationship between 3D morphological modifications of RBCs and the storage time, it is found that the MCH of RBCs with different storage times remains constant while the other properties such as $\overline{S}$, $\overline{\Phi}$ and MCHSD change more substantially. When the storage time is less than 34 days, there is no change in the 3D morphology of RBCs. However, when the storage time is longer than 34 days, the morphological change of RBCs is drastic such that the functionality of RBCs can be altered. From these experimental results, it can be seen that the modifications of the 3D morphology and the MCHSD of RBCs are

induced by the length of storage time and that the shelf-life of RBC's may be about 35 days when the blood is stored at refrigerator temperatures [93, 94].

3.2.5 Subsection Summaries

In this section, the 3D morphology and MCH of RBCs with different storage periods are investigated. First, RBC quantitative phase images have been obtained by off-axis digital holographic microscopy and numerical reconstruction method. Then, many single RBCs have been extracted from the RBC quantitative phase images by using the segmentation method based on marker-controlled watershed algorithm. Finally, the characteristic properties of RBCs including projected surface area, average phase value, volume, hemoglobin content and surface density measured at a single cell level have been evaluated over samples of several hundred RBCs using an automated analysis of the quantitative phase images. A statistical analysis indicates that 3D morphological changes in RBCs are induced by the length of storage time, while the hemoglobin content within RBCs is not changed substantially. In addition, it is concluded that 34 days of storage may be a threshold across which the morphology of RBCs starts to change substantially and hence possibly alter their functionality. Automated analysis of the relationship between the characteristic properties of RBCs and storage time may be helpful for drug tests.

3.3 Automated Method for Counting of Morphological Normal Red Blood Cells

The counting morphologically normal cells in human red blood cells (RBCs) is extremely beneficial in the health care field. In this paper, a three-dimensional

(3D) classification method of automatically determining the morphologically normal RBCs in the phase image of multiple human RBCs that are obtained by off-axis digital holographic microscopy (DHM) is proposed. The RBC holograms are first recorded by DHM, and then the phase images of multiple RBCs are reconstructed by a computational numerical algorithm [56-57]. To design the classifier, the three typical RBC shapes, which are stomatocyte, discocyte, and echinocyte, are used for training and testing. Non-main or abnormal RBC shapes different from the three normal shapes are defined as the fourth category. Ten features, including projected surface area, average phase value, mean corpuscular hemoglobin (MCH), perimeter, MCH surface density (MCHSD), circularity, mean phase of center part, sphericity coefficient, elongation, and pallor, are extracted from each RBC after segmenting the reconstructed phase images by using watershed transform algorithm [4]. Moreover, four additional properties, such as projected surface area, perimeter, average phase value, and elongation, are measured from the inner part of each cell that can give significant information beyond the previous ten features for the separation of the RBC groups; these are verified in the experiment by the statistical method of Hotelling's T-square test [96]. The principal component analysis (PCA) algorithm [97] is also applied to reduce the dimension number of variables and establish the Gaussian mixture densities using the projected data with the first eight principal components. Consequently, the Gaussian mixtures are used to design the discriminant functions based on Bayesian decision theory [98]. To improve the performance of Bayes classifier and the accuracy of estimation of its error rate, the leaving-one-out technique is applied [98]. Experimental results show that the proposed method can yield good results for calculating the percentage of each typical normal RBC shape in a reconstructed phase image of multiple RBCs that will be favorable to the analysis of RBC-related diseases. In addition, it shows that the discrimination performance for counting of normal shapes of RBCs can be improved by using 3D features of a RBC.

3.3.1 Bayesian Decision Algorithm

Bayesian decision algorithm is a kind of statistical decision making approach for the problem of pattern classification. The probability of a pattern belonging to a specific class is the combination of prior probability and a likelihood probability which can be expressed as following equation with one feature and n classes [3, 59].

$$P(C_i|x) = \frac{p(x|C_i)p(C_i)}{p(x)}, \tag{27}$$

where $p(x) = p(x|C_1)p(C_1) + p(x|C_2)p(C_2) + \ldots + p(x|C_n)p(C_n)$ is viewed as scale factor so as to make the summation of posterior probabilities $p(C_i|x)$ equal to 1 or just be taken as constant, $p(C_i)$ is the priori probability which represent the probability of class i appeared among all of the populations while conditional probability $p(x|C_i)$ is called as likelihood which denotes the probability of feature x occurring in a given class C_i, n is the number of classes. Consequently, the posterior probabilities $p(C_i|x)$ which means the probability for a given feature x that is classified into a specific class i can be derived by basic Bayes theorem in equation 27. Most of the time, a single feature is not enough to discriminate the classes. Multiple features are a better choice to distinguish the classes in a high dimension. The Bayes theorem for multiple features can be expressed as equation 28 which is similar as equation 27 but replacing single feature x with a feature vector x including multiple features and the likelihood $p(C_i|x)$ is a joint conditional probability (for discrete case).

$$P(C_i|X) = \frac{p(X|C_i)p(C_i)}{p(X) = \sum_{j=1}^{n} p(X|C_j)p(C_j)} \tag{28}$$

For the pattern classifiers based on Bayesian decision theory, discriminant functions, which are represented as $g_i(x)$ while i=1,...,n denoting the ith class, are widely used. For a sample with multiple features X, when $g_i(X) > g_j(X)$

and $i \neq j$,the sample is classified into class C_i that is corresponding to the class with the highest posterior probability in the Bayes theorem. Thus, the discriminant functions can be achieved by the following equation.

$$g_i(X) = P(C_i|X) = \frac{p(X|C_i)p(C_i)}{p(X) = \sum_{j=1}^{n} p(X|C_j)p(C_j)} \tag{29}$$

Since $p(X)$will not affect the decision and can be viewed as constant, the denominator in Equation (29) can be eliminated. In order to simplify and make the discriminant function much easier to understand, the discriminant function can be written in a simpler form as follows by taking natural logarithm to the numerator in Equation (29):

$$g_i(X) = \ln p(X|C_i) + \ln p(C_i). \tag{30}$$

As a result, the discriminant function based on bayesian decision theory is decided by the conditional probabilities (likelihood) $p(X|C_i)$ and priori probabilities $p(C_i)$.In particular, when the multiple features satisfy with the multivariate normal distribution, the conditional probabilities can be described by multivariate normal density as follows[3].

$$p(X|C_i) = \frac{1}{(2\pi)^{d/2}\left|\sum i\right|^{1/2}} \exp\left[-\frac{1}{2}(X-\mu_i)^t\left(\sum\right)^{-1}(X-\mu_i)\right] \tag{31}$$

where X is a d-dimensional feature column vector, μ_i is the d-dimensional mean vector of the ith class, $\sum i$ is the d-by-d dimensional covariance matrix of the ith class, $\left|\sum i\right|$ and $\left(\sum\right)^{-1}$ are the determinant and inverse of covariance matrix respectively. Consequently, the discriminant fuction in Equation (30) can be easily evaluated as Equation (32) if the conditional probabilities are mixture gaussian distribution (replace $p(X|C_i)$ in Equation (30) with Equation (31)).

$$g_i(X) = -\frac{1}{2}(X-\mu_i)^t\left(\sum i\right)^{-1} - \frac{d}{2}ln\,2\pi - \frac{1}{2}ln\left|\sum i\right| + \ln p(C_i) \tag{32}$$

Thus, the features are classified into the class that can achieve the biggest discriminant value. The discriminant function derived from bayesian decision

theory is proven that can achieve minimum-error-rate among all of the classifiers [3, 59].

3.3.2 Leaving-One-Out Technique

It is evident that a classifier designed with as much training and testing sets as possible will be much more robust in terms of improving the performance of classifier and the accuracy for estimating its error rate. However, due to the restriction of available sample data, the accuracy for both training and testing in a classifier design will be limited. Leaving-one-out method is such kinds of technique that can avoid the previous drawback to a large extent since this approach can nearly double the effective size of the sample data [3]. The procedure of leaving-one-out technique is described as follows. Suppose n samples are given in the data set, the classifier obtained by leaving-one-out is not designed and investigated by simply dividing the samples into training and testing sets at one time but n times. In this process, one sample from the data set is withdraw for testing set and the other n-1 samples is used to design the classifier. Thus, this withheld sample can be tested by the designed classifier with n-1 samples. It makes sense because the classifier is designed without this sample. The previous step can be repeatedly processed with n times so that each time one different testing sample will be left out and totally n samples can be conducted as testing set. For each round, a new classifier will be established with n-1 samples and tested by the one sample that is not used in the design of classifier. Consequently, the expected probability of error can be deduced as k/n on an average classifier which is trained on the n-1 samples and k is the number of errors in the testing phase. Since the samples in this technique is avoided to be both training and testing for a given classifier, the estimate of error rate can be regarded as unbiased and it will be as accurate as possible since all of the samples are used for testing [98-99]. Finally, the

classifier is designed by using the total n samples as training and its expected error rate will be at least as low as k/n since this classifier is created with n samples but not n-1 samples which is used in the leaving-one-out step. This process is illustrated in Figure 13. Step 1 in Figure 13 is conducted n times until no new sample can be used as test. The classifier gi(x) is designed based on Bayesian decision algorithm. After the table showed in step 2 of Figure 13 is achieved, the misclassification rate can be measured. Finally, all of the samples are applied to design the classifier which will be used to predict the sample with unknown class.

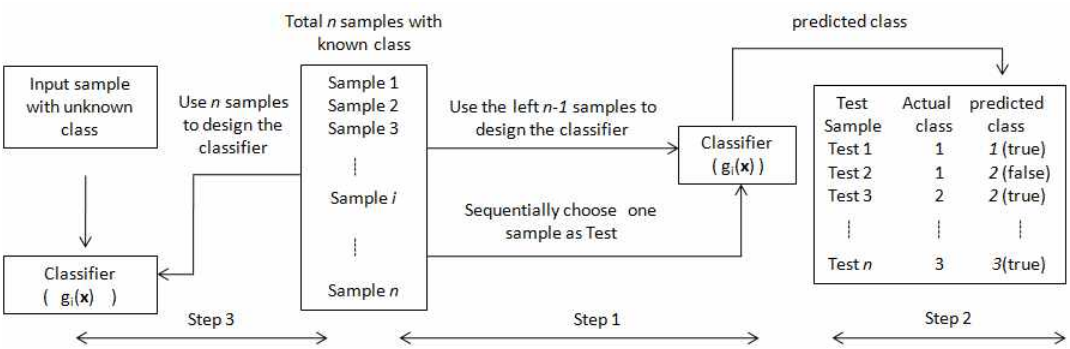

Fig. 13 Flowchart of leaving-one-out technique

3.3.3 Procedures of the Classifier Design

When the RBCs phase images are reconstructed by using computational numerical algorithm from the holograms obtained by off-axis digital holographic microscopy, each RBC is extracted with the background removed by marker-controlled watershed transform segmentation approach [37]. Then, ten features showed in table 3 are calculated from each whole segmented RBC. In addition, in order to increase the performance for separating the RBC groups, four more features including projected surface area, perimeter, average phase value and elongation are measured from the inside part of segmented RBCs which is also presented in Table 3. The whole segmented and inside part of

RBC is illustrated in Figure 14.

Table. 3 Description of Total Fourteen Features

The whole segmented RBC	
Feature	Description
F1: projected surface area	Number of pixels within single RBC×one pixel area
F2: perimeter	The length of cell boundary
F3: circularity	(Perimeter×perimeter)/area
F4: average phase value	Average phase value for pixels with in single RBC
F5: mch	mean corpuscular hemoglobin
F6:mchsd	mch surface density
F7: phase of center pixel	phase value of center pixel (average 5×5 pixels)
F8: sphericity coefficient	Center part phase value/maximal phase value
F9:elongation	Orientation of chain code in the cell boundary
F10: D-value	Center pixel phase value minus maximal pixel phase value
Inside part of the segmented RBC	
F11: projected surface area	Number of pixels within inside part of RBC×one pixel area
F12: perimeter	The length of boundary in the inside part of cell
F13: average phase value	Average phase value for pixels with in inside part of RBC
F14:elongation	Orientation of chain code in the boundary of inside part of cell

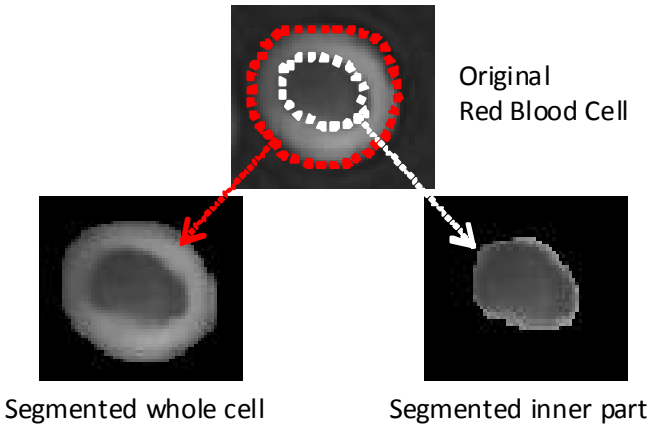

Fig. 14 Illustration of segmented whole and inside part of the cell.

The projected surface area, average phase value, mean corpuscular hemoglobin (MCH) and MCH surface density (MCHSD) are calculated from each whole segmented RBC as following equations respectively.

$$S = N\frac{p^2}{M^2} \tag{33}$$

$$\overline{\varphi} = \frac{1}{N}\sum_{i=1}^{N}\varphi_i \tag{34}$$

$$MCH = \frac{10\lambda}{2\pi\alpha}S\overline{\varphi} \tag{35}$$

$$MCHSD = \frac{MCH}{S} \tag{36}$$

where N is the number of pixels within a single RBC, p is the pixel size, M is the magnification of the digital holography microscopy, φ_i is the phase value at ith pixel within a single RBC, λ is the wavelength of the light source and α known as the specific refraction increment is a constant. When the boundary of each cell is marked by an 8-directional Freeman chain code [100], the features of perimeter, circularity and elongation can be achieved by equations as follows [100].

$$perimeter = N_e \times 1 + N_0 \times \sqrt{2}, \tag{37}$$

$$cirularity = perimeter^2 / S \tag{38}$$

$$elongation = \max(|N_{0,4} - N_{2,6}|, |N_{1,5} - N_{3,7}|), \tag{39}$$
$$where\ N_{j,k} = \sum_{\substack{i=1 \\ a_{i=j} \text{ or } a_{i=k}}}^{n} 1,$$

where N_e is the number of even valued elements while N_o is the number of odd element in the chain code of boundary in single RBC, n (=N_e+N_o)is total number of element in the Freeman chain code for each RBC. Also, the phase value of center pixel (pcp) is defined as the average phase value of the center 5×5 pixel, sphericity coefficient (sc) is the division between phase value of center pixel and maximal phase value within each whole segmented RBC and the D-value (dValue) is the difference between phase value in center pixel and maximal phase value. These features are defined as following equations.

$$pcp = \frac{1}{25} \sum_{-2 \le i \le 2} \sum_{-2 \le j \le 2} \varphi^{ij}, \tag{40}$$

$$sc = \frac{pcp}{\varphi_{\max}} \tag{41}$$

$$dValue = pcp - \varphi_{\max} \tag{42}$$

where φ^{ij} is the phase value at location (i,j) within a 5×5 window while (0,0) is the central location of the single RBC or inner part of RBC, $\varphi_{\max}$ is the maximal phase value within the analyzed single RBC or inner part of RBC.

For the measurement of four features in the inside part of RBC, the previous equations can be repeatedly used while only need to determine these features in the inside part instead of the whole segmented cell.

Here, the statistically method of Hotelling's T-square test [95] is applied to evaluate that the features calculated from the inside part of cell can indeed provide additional separation between each pair of RBC groups beyond the separation already achieved by the ten features obtained from the whole segmented cell. Let y denote the p×1 vector where p=10 here which include ten variables for measuring the features in the segmented cell and x denote the q×1 vector where q=4 that express the four variables for calculating the properties in the segmented inside part of cell. It is assumed that each pair of samples is

from multivariate normal populations and x1, x2 are two q×1 vectors while y1,, y2 are two p×1 vectors from two different groups. Then, the null hypothesis [H_0: x1 and x2 are redundant for separating the two classes beyond y1, and y2]can be represented as follows [95,97-98]:

$$T^2(x|y) = (v-p)\frac{T_{p+q}^2 - T_p^2}{v + T_p^2}, \tag{43}$$

which is distributed as $T_{q,v-p}^2$ where v=n_1+n_2-2 while n1,n2 are the number of samples in two groups respectively. When, $T^2(x|y) \geq T_{\alpha,q,v-p}^2$ the null hypothes is that x is redundancy would be rejected at significance level of α where the critical value of $T_{\alpha,q,v-p}^2$ can be achieved from the T^2-table with q and v-p degree of freedom. In Equation (43), T_{p+q}^2 and T_p^2 are expressed as following equations respectively [95].

$$T_{p+1}^2 = \frac{n_1 n_2}{n_1+n_2}\left[\begin{pmatrix}\overline{y_1}\\ \overline{x_1}\end{pmatrix} - \begin{pmatrix}\overline{y_2}\\ \overline{x_2}\end{pmatrix}\right]^T \begin{pmatrix}S_{yy} & S_{yx}\\ S_{xy} & S_{xx}\end{pmatrix}^{-1}\left[\begin{pmatrix}\overline{y_1}\\ \overline{x_1}\end{pmatrix} - \begin{pmatrix}\overline{y_2}\\ \overline{x_2}\end{pmatrix}\right], \tag{44}$$

$$T_p^2 = \frac{n_1 n_2}{n_1+n_2}(\overline{y_1} - \overline{y_2})^T S_{yy}^{-1}(\overline{y_1} - \overline{y_2}), \tag{45}$$

where $\overline{y_1}$ and $\overline{y_2}$ are the sample mean vectors, S_{yy},S_{yx} and S_{xx} are the covariance matrixes. In the experimental section, the T^2statistic test results among each pair of RBC groups are presented.

In order to demonstrate that 3D features of a RBC extracted from DHM imaging technique are beneficial to distinguish different kinds of RBCs, the RBC's features are divided into two categories that are given in Table. 4. One is defined as 2D features which can be acquired from 2D imaging system and the other is defined as 3D features which are obtained from DHM technique. Then, the Hotelling's T-square test as previous description for inner part feature analysis is conducted to check whether the 3D features can provide additional separation among RBCs classes beyond the partition already achieved by the 2D features. In this case, x in Equation (43) denotes the seven features from 2D features category and y represents the other seven features from 3D

features group.

Table. 4 Division of RBC features

2D Features	F1, F2, F3, F9, F11, F12, F14
3D Features	F4, F5, F6, F7, F8, F10, F13

Table. 5 Samples for training the classifier

RBCs with stomatocyte shape (Total samples: 87)	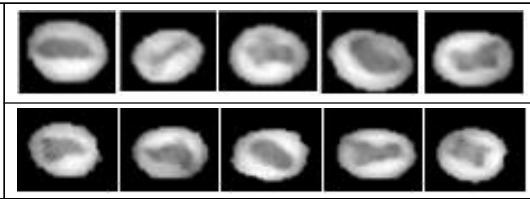
RBCs with discocyte shape (Total samples: 103)	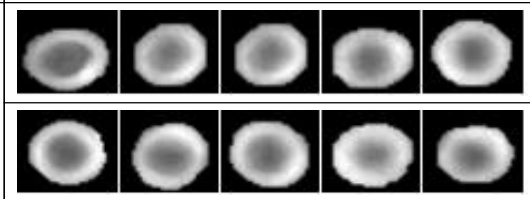
RBCs with echynocyte shape (Total samples: 106)	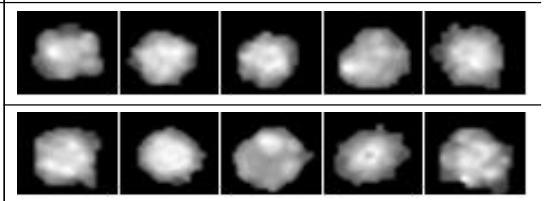

In our experiment, 87 RBCs labeled with stomatocyte shape, 103 RBCs labeled with discocyte shape and 106 RBCs labeled with echinocyte shape are extracted as samples. Also, the total fourteen features denoted by feature vector as $[X_1, X_2, \cdots, X_{14}]$ in each single RBC are calculated. What calls for special attention is that when there are no inside part for some RBCs, a random value from standard normal distribution will be assigned to the features from F11 to F14 in Table 3. Samples with known class which will be used to design the classifier are showed in Table 5.

After all of the fourteen properties are determined from the samples, the PCA algorithm is applied to these features so as to reduce the variables dimension

and the 60% principal components that is 8 components are retained for the classifier design in the next step. Consequently, the original data can be projected onto an eight dimension space by using the 8 principal components. Here, it is assumed that the all of the obtained data satisfy with the multivariate normal distribution. Accordingly, the joint density (conditional probability in Equation (28)) of the multiple features for each type of RBCs can be represented by mixture Gaussian density as expressed in Equation (31) with features after being projected from the eight principle components. Furthermore, It can assume that the priori probabilities ($p(C_i)$ in Equation (32)) for each class are equal so that this term can be removed from the discriminant function as well as the constant term $0.5d\ln 2\pi$ since they do not affect the pattern classification in this case. Therefore, the discriminant function in Equation (32) based on Bayesian decision theory can be further simplified as follows:

$$g_i(x) = -\frac{1}{2}(x-\mu_i)^T\left(\sum i\right)^{-1}(x-\mu_i) - \frac{1}{2}ln\left|\sum i\right|,\ 1 \le i \le 3 \tag{46}$$

where μ_i and $\sum i$ are estimated from respective sample data by using unbiased estimator [97]. As a consequence, one type of RBCs is corresponding to one discriminant function and three dicriminant functions are needed for the classification of three classes of RBCs (Class 1: stomatocyte shape RBCs, Class 2: discocyte shape RBCs, Class 3: echinocyte shape RBCs). The testing pattern will be categorized into the class which can achieve the biggest value by the corresponding discriminant function. Considering the situation that there are other types of RBCs excepting the three typical kinds of RBCs, the fourth class, which includes all types of RBCs excluding these three classical classes, is defined. When the probability of one sample belonging to any one of the three typical types of RBCs is low, it will be grouped into the fourth class. This can be achieved by Equation. (31) since the discriminant function in Equation. (29) is proportional to the value of likelihood (Equation.(31)) when the priori probability is assumed to be the same for all types of RBCs. In this paper, when the density in the likelihood (Equation. (31)) for the extracted

features from a RBC is less than 0.001 among all of the three typical types of RBCs, the corresponding RBC will be classified into the fourth class. The flowchart for our classifier design and RBCs classification is presented in Figure 15.

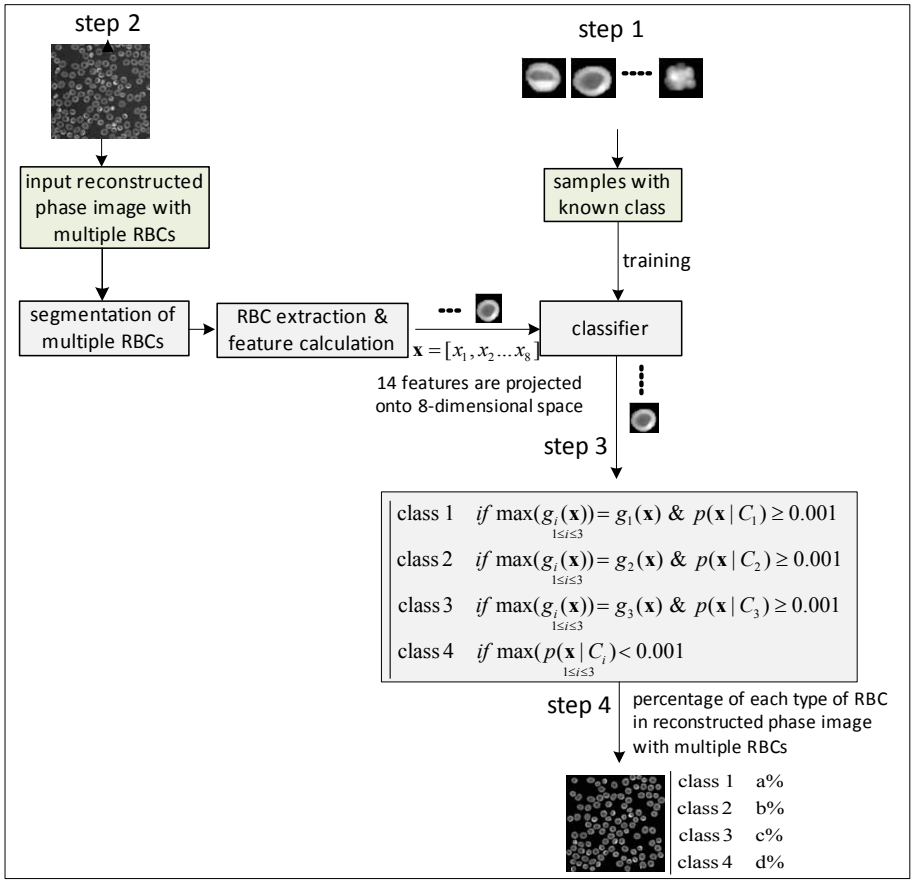

Fig. 15 Flowchart of RBCs classification.

Firstly, the classifier will be designed based on the Bayesian design theory by the leaving-one-out technique with the samples of known class (step 1 in Figure 15). Then, the obtained classifier is used to classify the RBCs in a reconstructed phase image with multiple RBCs (step 2 in Figure 15). In this step, the original RBCs phase image and the inside part of the RBC has to be segmented so as to extract all of the RBC and calculate the corresponding

features.

After that, all of the RBCs in the reconstructed RBCs phase image are grouped into one of the four types of RBCs as described in Figure 15. Finally, the percentage of different kinds of RBCs in the RBCs phase image can be calculated and analyzed (step 4 in Figure 15). Especially, when the occupation ratio of the fourth class achieves a highest value in a reconstructed RBCs phase image, this image should be examined carefully in further since this situation is not normal for a normal person. The leaving-one-out technique for improving the design of classifier and estimating the error rate is implemented by the pseudo-code showed in Figure 16 (based on Matlab). For the final design of classifiers (Class 1 denoted as $g_1(x)$, Class 2 denoted as $g_2(x)$ and Class 3 denoted as $g_2(x)$),all of the sample data are used as training set.

Step 1:	samples preparation (87 RBCs with stomatocyte shape, 103 RBCs with discocyte shape, 106 RBCs with echinocyte shape)
Step 2:	feature calculation (measure features from F1 to F14 for each RBC)
Step 3:	conduct principle component analysis (PCA) and derive new data with the main eight components.
Step 4:	design the classifier with the discriminant function based on Bayesian decision theory by using leaving-one-out technique
Step 5:	measure the misclassification rate
Step 6:	design the classifier without leaving one out (using all of the samples)

Fig. 16 Pseudo-code for the leaving-one-out test.

3.3.4 Experimental Results

The RBCs of healthy laboratory personnel were obtained through the Laboratoire Suisse d' Analyse Du Dopage--CHUV and stored at 4 °C during the storage period. The DHM measurements were performed several days after the blood was collected from the laboratory personnel. A total of 100-150 μl of

RBC stock solution were suspended in a HEPA buffer (15 mM HEPES pH 7.4, 130 mM NaCl, 5.4 mM KCl, 10 mM glucose, 1 mM Cacl2, 0.5 mM MgCl2, and 1 mg/ml bovine serum albumin) at 0.2% hematocrit for predominantly stomatocyte and discocyte shape RBCs while at a concentration of ~0.15% for predominantly echinocyte shape RBCs. A total of 4 μl of the erythrocyte suspension were diluted to 150 μl of the HEPA buffer and introduced into the experimental chamber, including two cover slips separated by spacers 1.2 mm thick. The cells were incubated for 30 min at a temperature of 37 °C before mounting the chamber on the DHM stage. All experiments were performed at room temperature (22 °C).

The simulation and measurement in this section are all executed on a 32-bit Windows 7 computer with a 3.30 GHz Intel Core i5-2500 CPU,4GB RAM, and 4 cores. The RBC phase images are reconstructed using the computational numerical algorithm from the holograms obtained by the off-axis DHM; then, the phase images are segmented by the watershed transform algorithm. Some of the reconstructed phase images, segmented RBCs, and the segmented inner part of the RBCs are shown in Figure 17 with the three typical types of RBC. After segmentation, all the 14 features are measured. Table 6 lists the quantitative validation for the extracted 14 features.

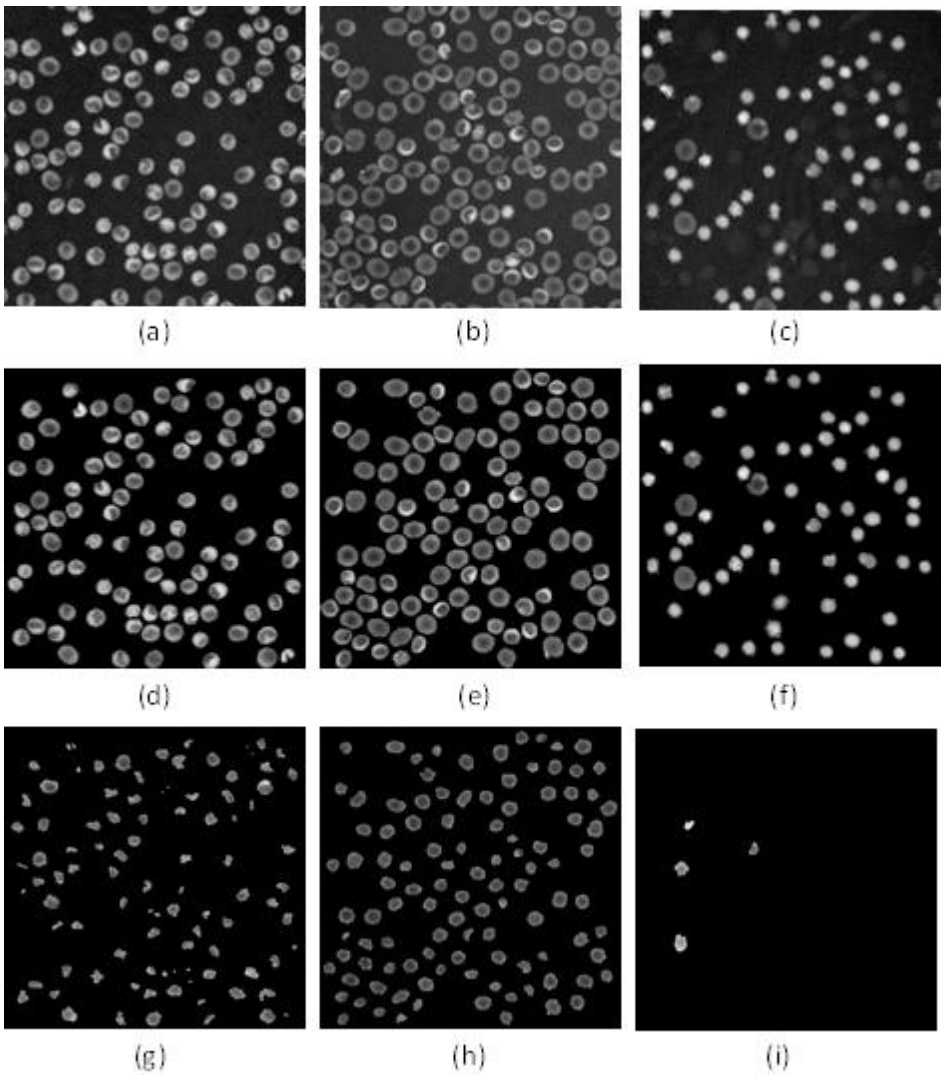

Fig. 17 Reconstructed RBC phase images and their segmented phase images. (a), (b), and (c) are reconstructed phase images for predominantly stomatocyte, discocyte, and echinocyte shape RBCs, respectively.(d),(e),and (f) are the corresponding segmented phase images from (a),(b),and (c). (g),(h),and (i) are the segmented inner part of the RBCs in (a),(b),and (c).

Table. 6 Quantitative validation of calculated 14 features from samples

Features	RBCs with stomatocyte shape (87 samples)		RBCs with discocyte shape (103 samples)		RBCs with echinocyte shape (106 samples)	
	Mean	Std	Mean	Std	Mean	Std
F1	34.31	3.83	47.28	5.40	25.76	3.96
F2	21.96	1.30	25.36	1.58	18.83	1.73
F3	14.13	0.44	13.67	0.37	13.84	0.93
F4	97.75	12.58	67.55	10.13	136.86	16.77
F5	31.60	4.12	30.10	5.01	33.04	4.29
F6	0.92	0.11	0.65	0.08	1.29	0.15
F7	84.35	28.21	26.84	14.41	207.70	37.73
F8	0.50	0.11	0.24	0.12	0.91	0.10
F9	7.73	5.32	8.38	5.73	6.12	4.75
F10	81.88	24.07	88.70	25.60	23.21	20.41
F11	9.83	3.36	20.50	4.43	0.01	0.93
F12	12.61	2.43	17.03	1.94	0.08	0.83
F13	81.50	11.65	56.72	7.72	0.10	0.97
F14	12.13	6.25	7.30	5.69	0.06	1.03

In this experiment, it has demonstrated that the features from the inner part of the RBCs are not redundant, but can contribute information to the separation of the RBC groups by Hotelling's T-square test. The calculated $T^2(x|y)$ value and critical value of $T^2_{\alpha,q,v-p}$ (see Section 3.3.3 for details) searched from the T^2- table are shown in Figure 18. It is noted that all the $T^2(x|y)$ values among each pair of RBC groups are larger than their corresponding critical value. Consequently, the null hypothesis H_0 when the features from the inner part of the RBCs are not significant in separating the RBC groups at the 0.05 level of significance is rejected. In other words, the features from the inner part of the RBCs can be helpful to classify the RBCs. Similarly, Statistical analysis results shown in Figure 19 reveal that 3D features of a RBC extracted from DHM imaging system can contribute to separate the RBCs classes. Therefore,

the discrimination performance for counting normal shapes of RBCs can be improved by adding to the 3D features of a RBC to the 2D ones.

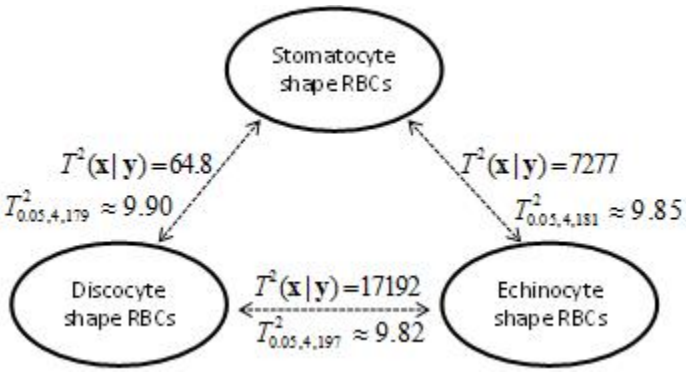

Fig. 18 Redundance analysis results for inner part features of RBCs with Hotelling's T-square test

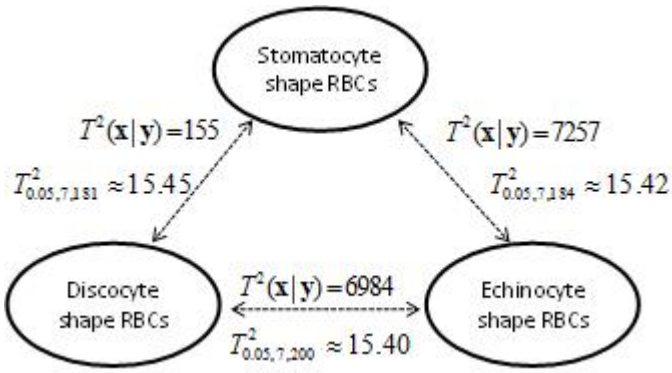

Fig. 19 Redundance analysis results for 3D features [see Table.4] of RBCs with Hotelling's T-square test

Next, the PCA algorithm is applied to the 14 features, and the 60% principal components (that is eight principal components) are retained to design the Bayesian-based classifier. Because it assumes that the multiple variables satisfy the multivariate Gaussian distribution, the mixture Gaussian density of each

group can be established by the features obtained from the multiplication of the original sample features with the extracted eight principal components. Therefore, the corresponding discriminant function can be realized with the created mixture Gaussian density for each RBC population as Equation (46). As the design presented in Figure 16, the leave-one-out experiment results show that the misclassification rate for the RBCs with stomatocyte shape is 3 / 87 = 3.45%, the misclassification rate for the RBCs with discocyte shape is 4 / 103 = 3.88%, and the misclassification rate for the RBCs with echinocyte shape is 3 / 106 = 2.83%. On the contrary, the misclassification rates for RBCs with stomatocyte, discocyte and echinocyte shape by only using 2D features (see Table.4) are measured to be 11/87=12.64%, 13/103=12.62 and 6/106=5.66% respectively. It is noted that the classifier based on the Bayesian decision algorithm with both 2D and 3D features achieved a very good result for the classification of RBCs with three different shapes. These classification results and misclassification rate for the three types of RBC by using 2D and 3D features are shown in Table. 7. It demonstrates that the discrimination performance for classification of different types of RBCs can be enhanced by using 3D features of a RBC. Moreover, the throughput which is defined as the processed data per second in our method is measured to be 27.64Mb/s and the total computational time for training and testing process is calculated to be 0.0024 second by averaging simulation result of 20 times.

The results of analyzing the percentage of morphologically normal RBCs in the reconstructed phase images with multiple RBCs are also shown in Figure 20. Figures 18(a), (b), and (c) are the measured percentages of the typical normal shapes of RBCs in the reconstructed RBC phase images. It is visually found that the majority of RBCs in each RBCs phase image are consistent with the highest percentage rate for the corresponding image in Figure 20. These percentages are automatically derived from the classifier that is obtained by our classifier algorithm whose misclassification rates are demonstrated to be low. It is believed that the proposed classifier can be adopted to count automatically

the morphologically normal cells in multiple human RBCs. In addition, the classifier can be helpful for the analysis of RBC-related diseases because the occupation ratio of the different types of RBC is associated with certain types of diseases.

Table. 7 Classification Results of the three types of RBCs

Using Both 2D and 3D Features for RBC Classification					
Actual Group	Number of Observations	Predicted Group			Misclassification rate
		Stomatocyte RBC	Discocyte RBC	Echinocyte RBC	
Stomatocyte RBC	87	84	3	0	3.45%
Discocyte RBC	103	3	99	1	3.88%
Echinocyte RBC	106	3	0	103	2.83%
Using only 2D Features for RBC Classification					
Stomatocyte RBC	87	66	9	2	12.64%
Discocyte RBC	103	11	90	2	12.62%
Echinocyte RBC	106	5	1	100	5.66%

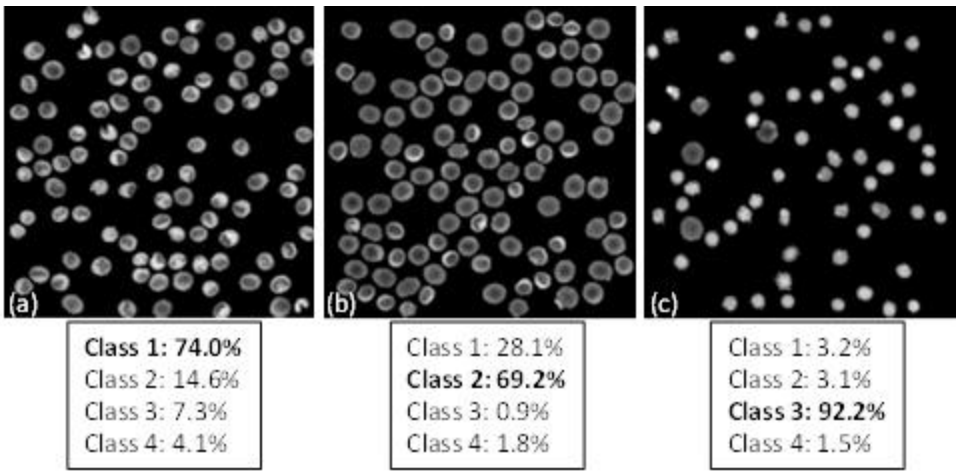

Fig. 20 Analysis of reconstructed phase image with multiple RBCs. (a), (b), and (c) are segmented images with percentages of each type of RBC labeled by our designed classifier method. (Class 1: RBCs with stomatocyte shape, Class 2: RBCs with discocyte shape, Class 3: RBCs with echinocyte shape, Class 4: other types of RBC).

3.3.5 Subsection Summaries

In this section, a classifier using DHM and Bayesian decision theory for automatic counting of the morphologically normal RBCs of stomatocyte, discocyte, and echinocyte shapes which allows us to quantitatively determine the percentage of normal cell shapes in multiple human RBCs is designed. The hologram patterns of the RBCs were first captured by the off-axis DHM, and the RBC phase images were reconstructed through the computational numerical algorithm. Ten patterns were calculated from each RBC that was extracted from the RBC phase images through the watershed transform segmentation method, and four more features were collected from the inner part of the RBC. Hotelling's T-square test showed that the features from the inner part of the RBC can significantly improve the separation of different RBC groups. In order

to reduce the dimension space of the variables, the PCA algorithm was adopted, and the first eight principal components were retained to retrieve new projected features to establish the mixture Gaussian densities for each type of RBC. Subsequently, the discriminant function based on Bayesian decision theory was used to design the classifiers. Finally, in order to improve the accuracy for estimating the error rate of the classifier, the leaving-one-out technique was used and tested. Experimental results demonstrated that our classifier can give a good performance for the classification of RBCs with stomatocyte, discocyte, and echinocyte shape. Their misclassification rates were at least as low as 3.45%, 3.88% and 2.83%, respectively. In addition, we demonstrate that the discrimination performance for RBCs classification can be improved by using both 2D and 3D features of a RBC. Furthermore, the designed classifier was able to group an RBC into a fourth class when the 2D and 3D features of the RBC are extremely different from the three typical types of RBC. This automatic RBC classification method can be extremely helpful for drug testing and for analyzing certain RBC-related diseases because the percentage of normal cell shapes in multiple human RBCs varies from disease to disease.

4. Automated Analysis of Three-dimensional Cardiomyocytes

Compounds tested during drug development may have adverse effects on the heart; therefore all new chemical entities have to undergo extensive preclinical assessment for cardiac liability. Conventional intensity-based imaging techniques are not robust enough to provide detailed information for cell structure and the captured images result in low-contrast, especially to cell with semi-transparent or transparent feature, which would affect the cell analysis. In this dissertation it is shown, for the first time, that digital holographic microscopy (DHM) integrated with information processing algorithms automatically provide dynamic quantitative phase profiles of beating cardiomyocytes. It is experimentally demonstrated that relevant parameters of cardiomyocytes can be obtained by our automated algorithm based on DHM phase signal analysis and used to characterize the physiological state of resting cardiomyocytes. Our study opens the possibility of automated quantitative analysis of cardiomyocyte dynamics suitable for further drug safety testing and compounds selection as a new paradigm in drug toxicity screens.

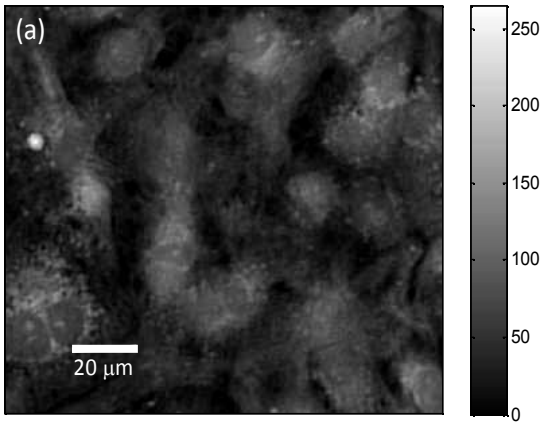

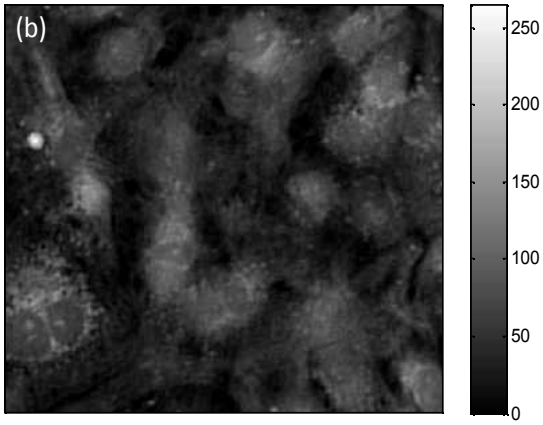

Fig. 21 Two optical path difference (OPD)[nm] images of cardiomyocytes captured at different time.(a) Frame #101 (b) Frame #102 (total 540 frames).

In the present work, the dynamic beating profile of cardiomyocytes obtained by DHM is analyzed using two proposed methods, either by monitoring the average or the variance information of imaged cells. The contraction and relaxation movement are also quantified by analyzing the difference between two successively acquired DHM quantitative phase images. From these experimental results, automated procedures are proposed for multiple parameters recording on cardiomyocytes dynamics imaged by DHM for a new methodology in drug toxicity screens. For the quantitative analysis of cardiomyocyte dynamics, the beating activity are calculated using two alternative methods, averaged optical path difference (OPD) images and variance of OPD images. The contraction and relaxation feature of cardiomyocyte were also measured using the proposed automated procedure. Figure 21 shows two OPD images of cardiomyocytes reconstructed from holograms.

4.1 Cell Culture and Imaging

iCell cardiomyocytes (human induced pluripotent stem (iPS) cell-derived cardiomyocytes) obtained for Cellular Dynamics Int. (Madison, WI) were culture according to the manufacturer's indication and grown for 14 days before recording. Measurements were achieved in a Chamlide WP incubator system for 96-well plate (LCI, South Korea) set at 37°/5% C02 with high humidity.

DHM images were acquired in an off-axis configuration on a commercially available DHM T-1001 from LynceeTec SA (Lausanne, Switzerland) equipped with a motorized xy stage (Märzhäuser Wetzlar GmbH & Co. KG, Wetzlar, Germany, ref. S429). Images were recorded using a Leica 20×/0.4 NA objective (Leica Microsystems GmbH, Wetzlar, Germany, ref. 11566049). Time-lapse images were acquired at 10 Hz for 1 minute.

4.2 Cardiomyocytes Beating Profile Measurement using Averaged OPD Images

The beating profile of cardiomyocytes was briefly calculated by thresholding the cardiomyocyte OPD images [see Figure 21] with a threshold value of 10% of the maximum OPD signal and then the thresholded images were averaged. 10% is an empirical value and is used to restrain the effect of noise. This process is described by the following equation:

$$\overline{opd}^{(i)} = average(opd\_thresh(x,y)^{(i)}), \tag{47}$$

$$with\ opd\_thresh(x,y)^{(i)} = \begin{matrix} opd(x,y)^{(i)} & \text{if } opd(x,y)^{(i)} \geq \max(opd(x,y)^{(i)} \times 0.10 \\ 0 & \text{if } opd(x,y)^{(i)} < \max(opd(x,y)^{(i)} \times 0.10 \end{matrix}$$

where $\overline{opd}^{(i)}$ is the average value of ith OPD image after thresholding, opd_ $opd\_thresh(x,y)^{(i)}$ is the OPD value at location of (x,y) on the ith threshodled

cardiomyocyte image, opd(x,y) is the OPD value at location of (x,y) for the ith cardiomyocyte image in optical path difference while 1≦x≦M, 1≦y≦N (M and N are the size of cardiomyocyte OPD image), $\max(opd(x,y))^{(i)}$ means the maximum value of ith cardiomyocyte image. One of the thresholded cardiomyocyte images obtained with this method is given in Figure 22. In addition, the beating profile with the capture time of cardiomyocytes resulted from this method is showed in Figure 23 including a small inset with a zoom on a single beating pattern. It is noted that the beating activity of cardiomyocytes is obvious (short peaks of high amplitude).

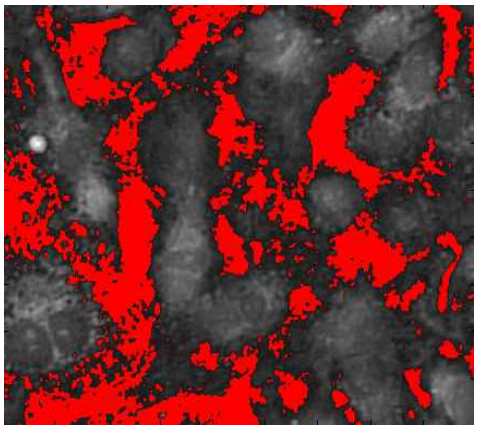

Fig. 22 Threshold cardiomyocyte image (red color denotes background after thresholding).

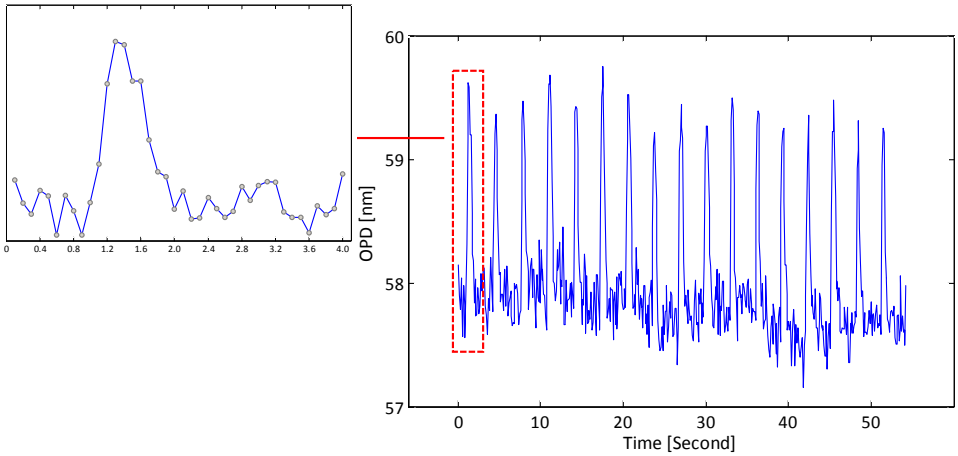

Fig. 23 Beating activity of cardiomyocyte (Inset shows a single beat).

After the segmentation, every single RBC can be extracted. Then, the RBC's properties such as Mean phase value, Area, Dry Mass and sphericity coefficient can be obtained. The following subsections are the definition of these properties used for RBCs analysis. Then, multiple parameters including amplitude, rising time, falling time, IBD50, IBD10, rising/falling slope, beating rate and beating period based on beating profile in Figure 23 were derived. These parameters are defined in Table 8 [101]:

In order to measure the above-defined parameters, peaks are detected by applying the first derivative technique to the original data curve in Figure 23 and finding locations where the first derivative values are zeros. The detected peaks based on cardiomyocytes beating profile are given in Figure 24(a).

Table. 8 Characteristic Parameters of Cardiomyocyte

Parameter	Definition
Amplitude	Value difference from each positive peak to the following negative peak (Amplitude=Ampmax - Ampmin)[see Fig. 25]
Rising time	The time elapsed from Amp20toAmp80(=T3-T1)[see Fig. 25]
Falling time	The time elapsed from Amp80toAmp20(=T6-T4)[see Fig. 25]
IBD50	The time elapsed for two points compose one Amp50(=T5-T2)[see Fig. 25]
IBD10	The time elapsed for two points compose on Amp10(=T7-T0)[see Fig. 25]
Rising/ Falling slope	The change of increased/decreased amplitude over the time course between Amp80andAmp20(=Amp80 - Amp20)[see Fig. 25]
Beating rate	The total number of positive/negative peaks in 1 minute (= total number of positive peaks/total time)
Beating period	The time between two adjacent positive and/or negative peaks (= the time of ith positive peak-the time of (i-1)th positive peak)
Frequency	The number of beating period per second (= total number of beating period/total time)

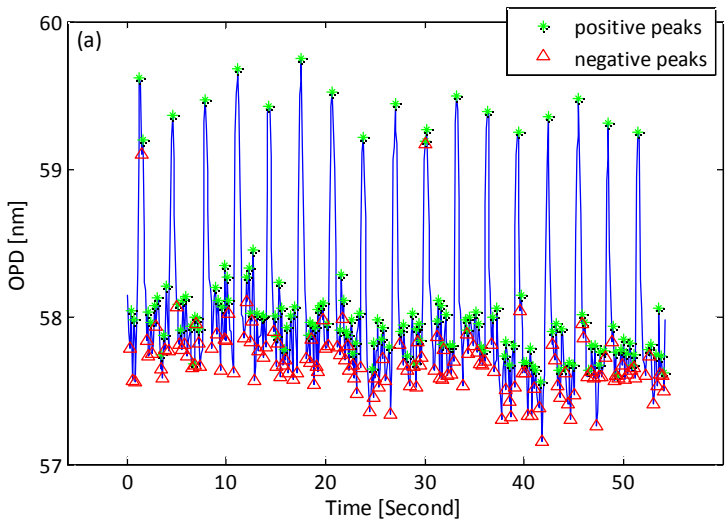

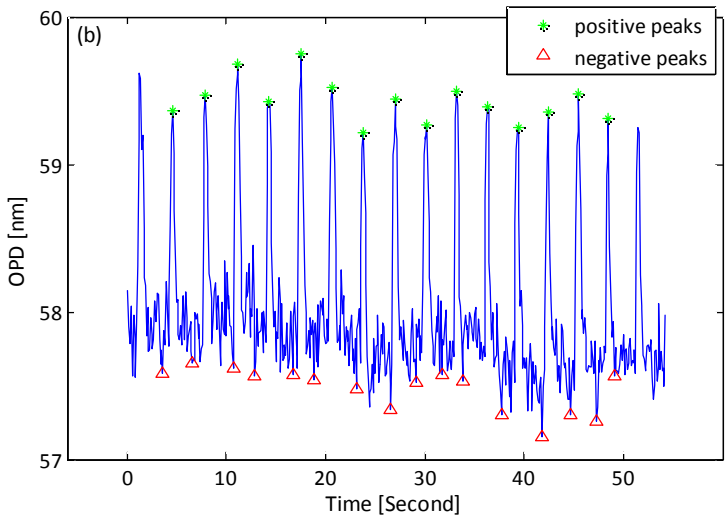

Fig. 24 Detected peaks in beating profile of cardiomyocytes. (a) Detected peaks on raw data. (b) Filtered peaks based on results of (a).

It can be noted from Figure 24(a) that many peaks including false peaks are detected. As a sorting process, positive peaks with values below a threshold and the negative peaks with values above a threshold are removed. This threshold can be automatically determined with Otsu's method [59] by using all of the positive peaks detected in Figure 24(a). In addition, the minimum negative peak between two neighbor positive peaks is extracted and then the maximum positive peak between two neighboring negative peaks is selected. This process reduces some inappropriate peaks and results in appropriate peaks for each beating period as shown in Figure 24(b).

Consequently, the beating profile between two adjacent negative peaks considered as one beating period is extracted [see Figure 25]. It is noted that the beating periods calculated between two negative peaks is approximately equal to that between two positive peaks. At the same time, the extracted beating profile for each beating period can be fitted with polynomials of degree 9 in a least-square criterion. The degree of 9 is reached by examining polynomials of up to degree 9 (up to degree 9 because data samples among

some beating profiles are around 10) for fitting the data based on the final fitting errors. The fitted polynomial with degree of 9 is described with the following equation:

$$f(x) = \sum_{i=1}^{10} a_i x^{10-i}, \tag{48}$$

where x represents the sample point on each beating period and ai which is the coefficient of polynomial are obtained with least-square criterion based on sample points. The average absolute error for each sample point (absolute error between actual and fitted point) is measured to be 0.1900. One of the fitting polynomial curves and the measured parameters are given in Figure 25.

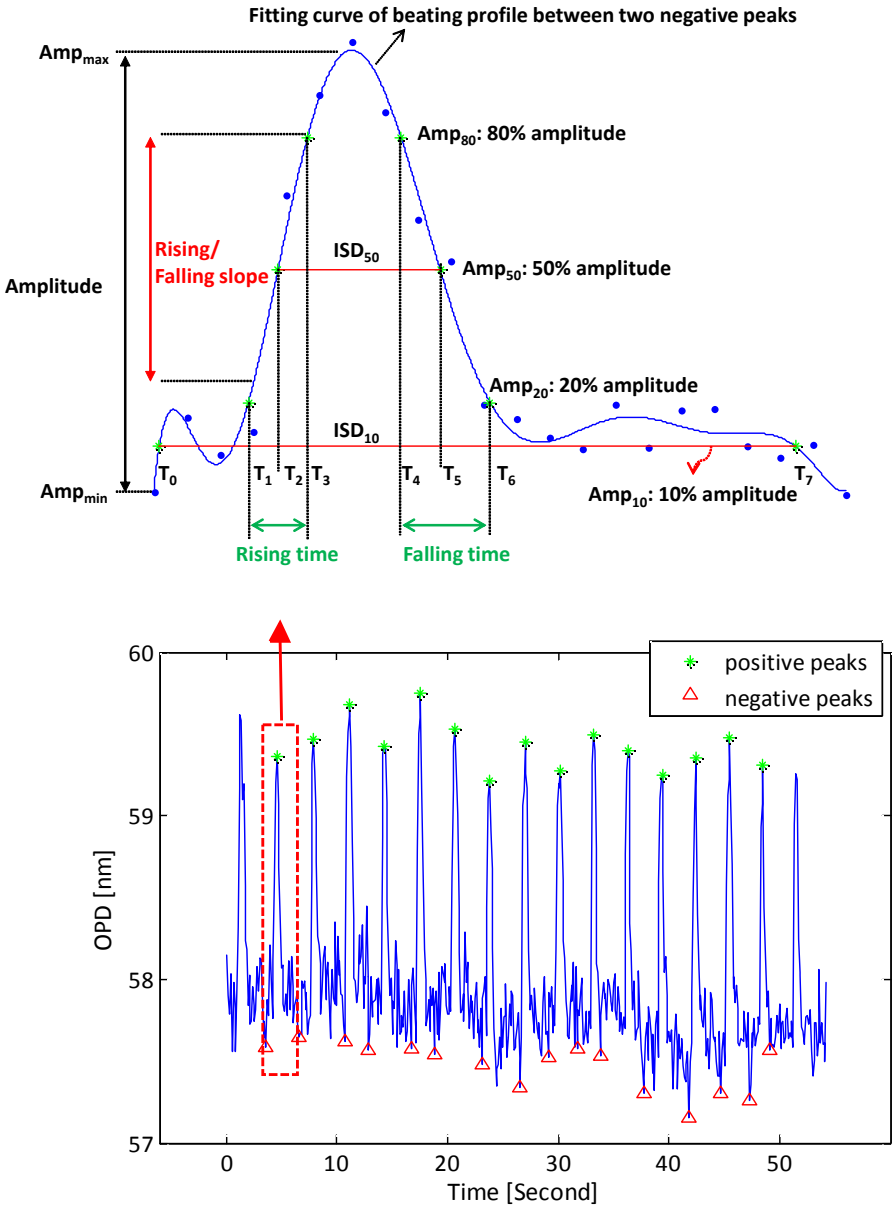

Fig. 25 Illustration of the fitted curves with parameters within one beating period on cardiomyocytes beating profile.

With the fitted polynomials curves, the amplitude value defined in Table 8 can be calculated as the maximum value minus the minimum value on the

fitted curve. Thus, the corresponding time [unit is second] in x axis for Amp10, Amp20, Amp50, Amp80 [see Figure 25] can be also be computed by solving the fitted polynomial equation. Then, all of the above mentioned parameters are measured for each individual beating period and a population average with coefficient of variation, (cv=standard deviation/average value, a parameter often used in high-throughput screening) is computed as shown in Table 9.

Table. 9 Measured Values of Multiple Parameters on Cardiomyocytes Beating Profile

Multi-parameter	Values (mean/cv)
1: Amplitude:	2.05/0.30
2: Rising time:	0.58/1.05 (seconds)
3: Falling time:	0.86/0.69 (seconds)
4: IBD50:	0.79/0.33 (seconds)
5: IBD10:	2.94/0.19 (seconds)
6: Rising/Falling slope:	1.19/0.30
7: Beating rate:	21.86/0
8: Beating period:	2.94/(sd=0.10 seconds)
9: Frequency	0.34/0

4.3 Cardiomyocytes Beating Profile Measurement using Variance of OPD Images

An alternative way to derive the beating profile of cardiomyocytes which is less sensitive to noise (originating from shot noise, speckle and contribution of out-of-focus structures), but requires more computer resources is to measure the variance of each OPD image after the temporal mean of the image stack is subtracted. This method is illustrated by Equation 49:

$$\delta_{opd}^{(i)} = variance\left[opd(x,y)^{(i)} - \overline{opd}_{temp}\right], \tag{49}$$

where opd(x,y)(i) is the ith OPD image, while 1≦x≦M and 1≦x,y≦N (M and N are the size of cardiomyocyte OPD image), $\delta_{opd}^{(i)}$ represents the variance of the ith cardiomyocyte image after temporal mean subtracted and $\overline{opd}_{temp}$ is the temporal mean which is calculated as the mean value of the image stack in the temporal dimension. The beating profile measured with this method is showed in Figure 26. Compared to the previous analysis method (Figure 24), this approach is more stable and less sensitive to noise (changes in the absolute value of the OPD signal).

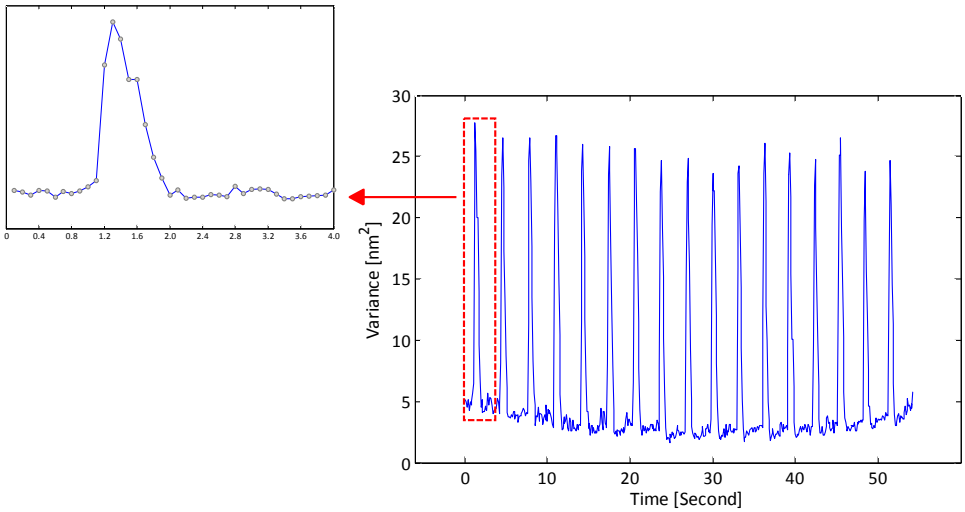

Fig. 26 Measured beating profile with variance information (inset shows a single beat)

Similar with the previous method, the peaks in Figure 26 can be detected using the first derivative property [see Figure 27(a)]. In addition, the positive and negative peaks are screened with a threshold value obtained by Otsu's method [30]. Consequently, the minimum negative peak between two neighboring positive peaks and the maximum positive peak between two neighboring negative peaks are selected [see Figure 27(b)].

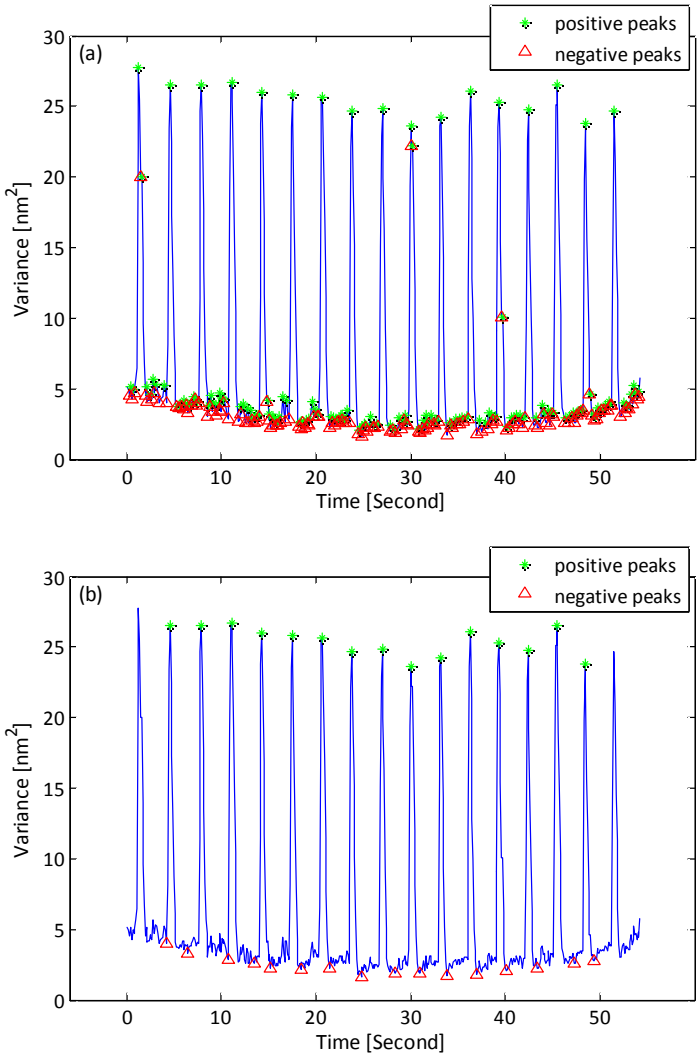

Fig. 27 Detected peaks on cardiomyocyte beating profile. (a) Detected multiple peaks. (b) Detected multiple peaks with some false peaks removed.

The beating profile within one beating period (between two negative peaks) can be individually extracted and is fitted with polynomial equation of degree 9 in a least-square error sense as that in Figure 25. The average absolute error for each sample point is measured to be 2.0359. Consequently, the same parameters as in the previous method can be measured and the corresponding

mean and coefficient of variation (cv) are given in Table 10. The measured parameters are in excellent agreement with the literature [102].

Table. 10 Measured Multiple Parameters on Cardiomyocytes Beating Profile

Multi-parameter	Values (mean/cv)
1: Amplitude:	23.06/0.17
2: Rising time:	0.45/0.98 (seconds)
3: Falling time:	0.26/1.04 (seconds)
4: IBD50:	0.66/0.23 (seconds)
5: IBD10:	2.30/0.25(seconds)
6: Rising/Falling slope:	13.83/0.17
7: Beating rate:	21.91/0
8: Beating period:	2.93/(sd=0.10)
9: Frequency	0.34/0

4.4 Cardiomyocytes Contraction and Relaxation Measurement

In order to observe the contraction and relaxation feature of cardiomyocyte, each captured image in the temporal stack is subtracted from the following one and then the spatial variance of the OPD is measured thus quantifying the amount of spatial displacement between successive frames (the cells used here are the same as those showed in Figure 21). The resulting image contains cardiomyocytes contraction and relaxation information (both indicated by an increase in the temporal variance signal). Two of the subtracted images are shown in Figure 28 where Figure 28(a) and 26(b) are different images at the minimum and maximum of a beat, respectively. The beating profile with contraction and relaxation information of cardiomyocyte is given in Figure 29(a), where one higher peak is for contraction and the neighboring lower peak is for relaxation. Then, the peaks can be detected with the first derivative criterion

(locations where the first derivative values are zeros). Similarly, positive peaks for contraction can be properly extracted with Otsu's thresholding algorithm by using all of the detected positive peaks. Next, a maximum peak between two neighboring contraction peaks is chosen as a positive peak for relaxation. Consequently, the inappropriate peaks can be removed. The resulted curves from Figure 29(a) with peaks indicated are given in Figure 29(b).

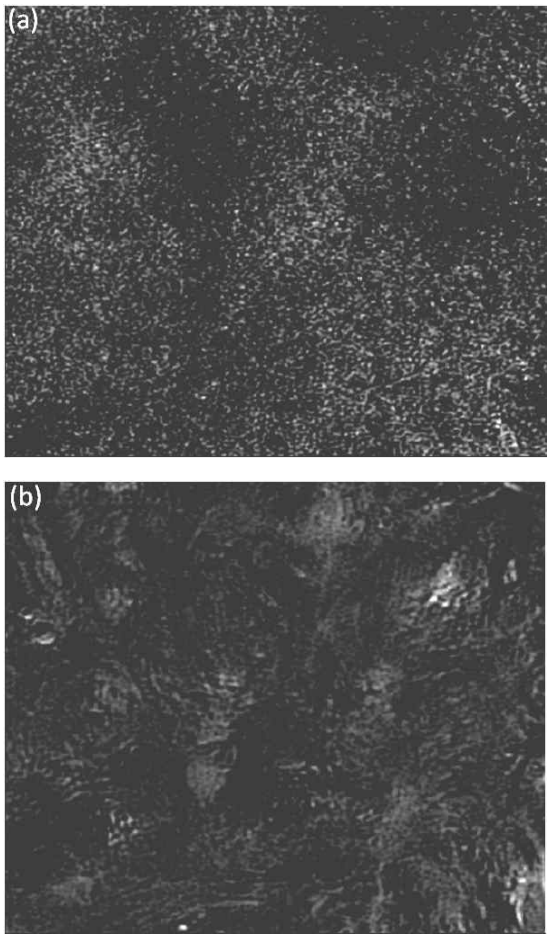

Fig. 28 Illustration of the difference images. (a) different image at the minimum of a beat (b) different image at the maximum of a beat.

Finally, the beating rate, beating period and frequency for cardiomyocytes

contraction and relaxation can be measured based on the detected positive peaks that include contraction and relaxation peaks. In addition, the time between the cardiomyocytes contraction and the following relaxation can be also calculated with the detected peaks in Fig. 27(b). These measured data are given in Table 11.

Table. 11 Measured Multiple Parameters on Cardiomyocyte Contraction and Relaxation Curve

Multi-parameters		Values (mean/cv)
Contraction	Beating rate:	23.14/0
	Beating period:	2.94/0.03
	Frequency	0.36/0
Relaxation	Beating rate:	23.14/0
	Beating period:	3.06/0.16
	Frequency	0.36/0
Time between contraction and the following relaxation		0.41/0.14

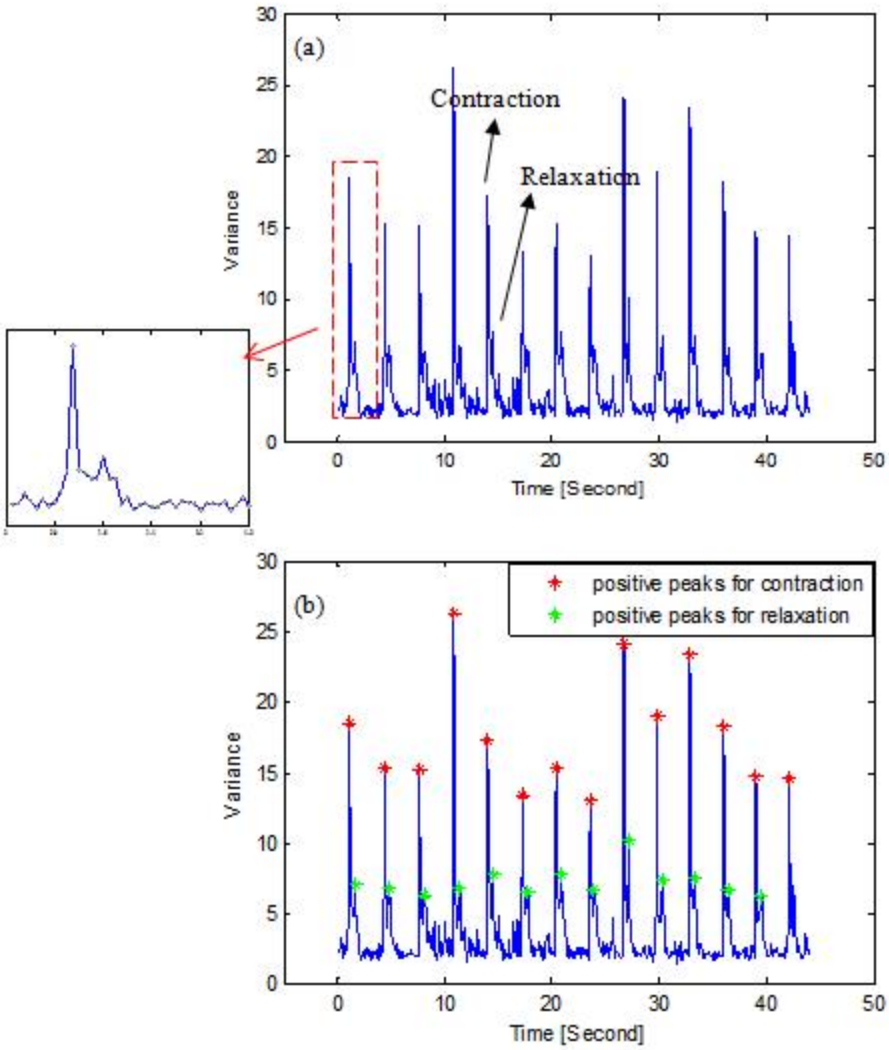

Fig. 29 Cardiomyocytes beating profile with contraction and relaxation information. (a) raw data of cardiomyocytes beating profile. (b) cardiomyocytes beating profile with contraction and relaxation peaks indicated. (inset shows a single beat with contraction and relaxation peaks)

4.5 Discussions and Section Summaries

In this paper, for the first time, human cardiac muscle cells' dynamics and

their spontaneous beating rates are quantitatively explored through the fusion of digital holography microscopy and information processing algorithms.

Experimental demonstrations have been provided for this new concept on multiple parameters recording on cardiomyocytes dynamics. From the experiments in the cardiomyocytes beating profile measurement using averaged OPD images and variance of OPD Images reported in Figure 25, Figure 27, Table 9 and Table 10, it is assured that interesting parameters of cardiomyocytes dynamics can be automatically measured. In addition, statistical parameters such as mean and coefficient of variation on the cardiomyocyte characteristics can be estimated. Four more cardiomyocyte image sequences were analyzed in order to show the generality of the proposed methods.

Among these image sequences, one of them is acquired with difficult conditions which mean having severe disturbance (a few out-of-focus debris are flowing through the field of view during the acquisition) while the other sequences are comparable inquality to the one presented previously.Four image sequences with peaks detected using the first (Section 4.2),second (Section 4.3) and third (Section 4.4) methods are given in Figure 30, Figure 31 and Figure 32 respectively where Figure 30 (a), Figure 31 (a) and Figure 32 (a) are from image sequences under tough/difficult conditions. It should be noted from these figures that our proposed method can detect all of the peaks, even in image sequences with debris interference. However, we found that the first method generated many noisy peaks in difficult conditions (1st image sequence) which makes the parameter measurement not accurate. On the other hand, the second and third methods are more stable to analyze these image sequences even those obtained under difficult conditions. Consequently, all of the needed multi-parameters can be measured based on these images, therefore proving the robustness of the analysis algorithm.

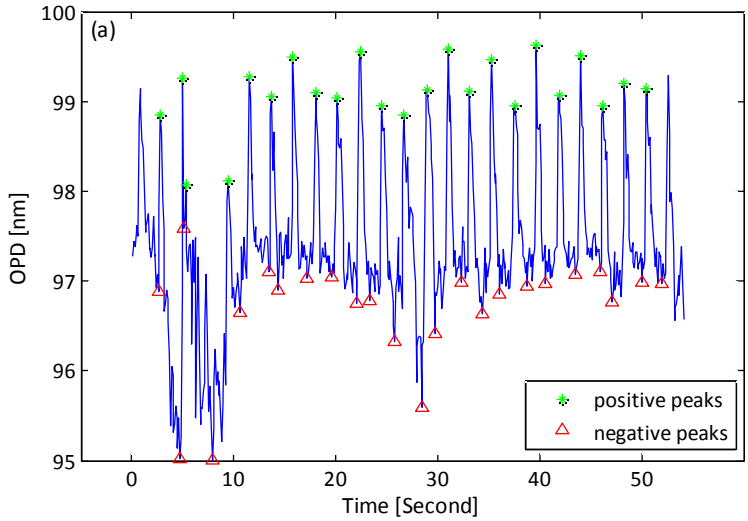

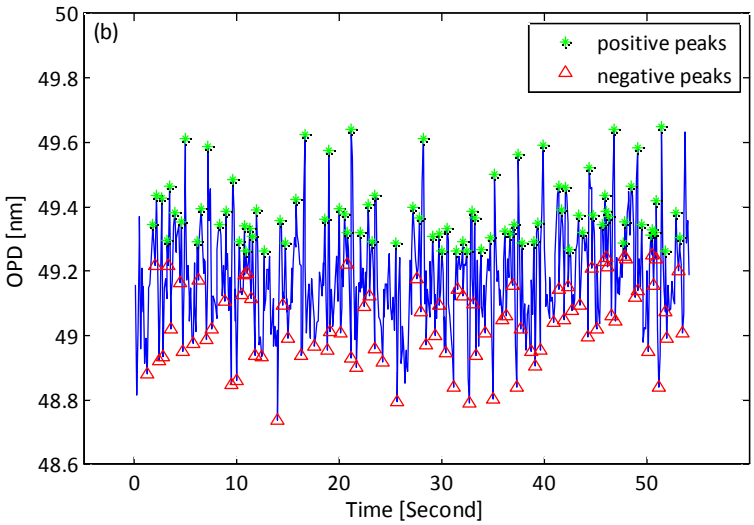

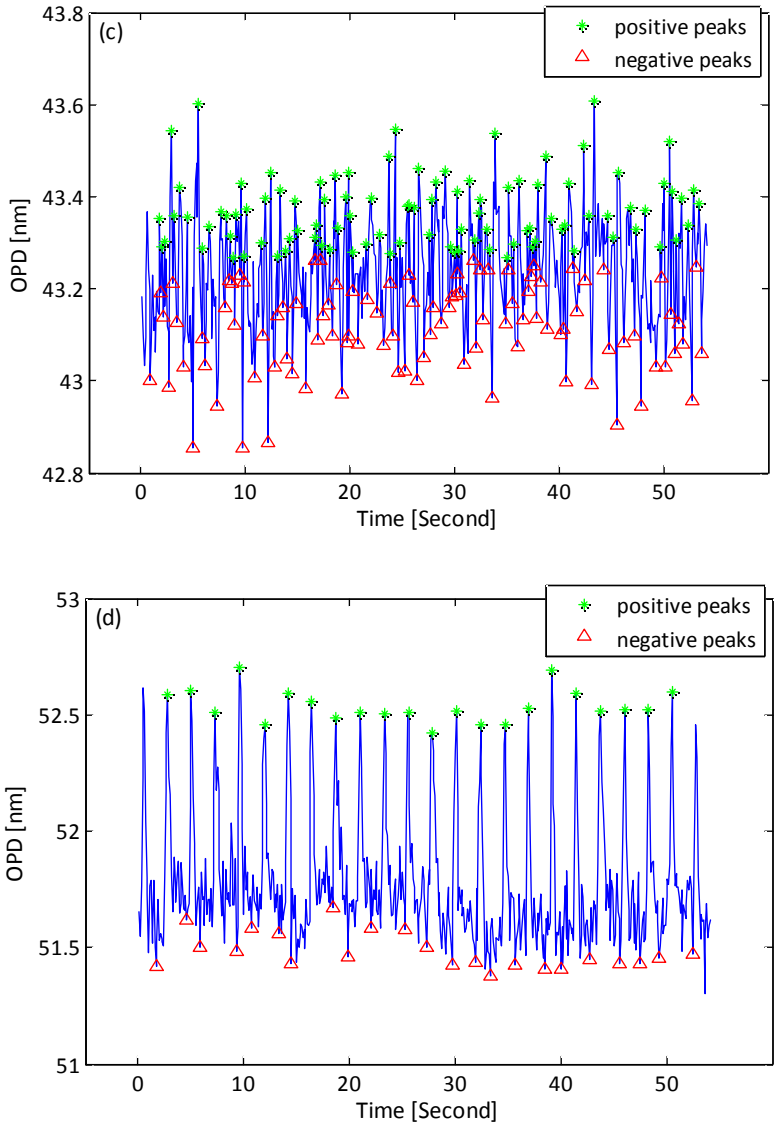

Fig. 30 Detected peaks based on four more cardiomyocyte sequences with the method in the Section 4.2. (a) cardiomyocyte image sequences acquired with difficult conditions. (b), (c), and (d) "noise-free" recordings (i.e. no debris interfering with the measurement) similar to the previous recording.

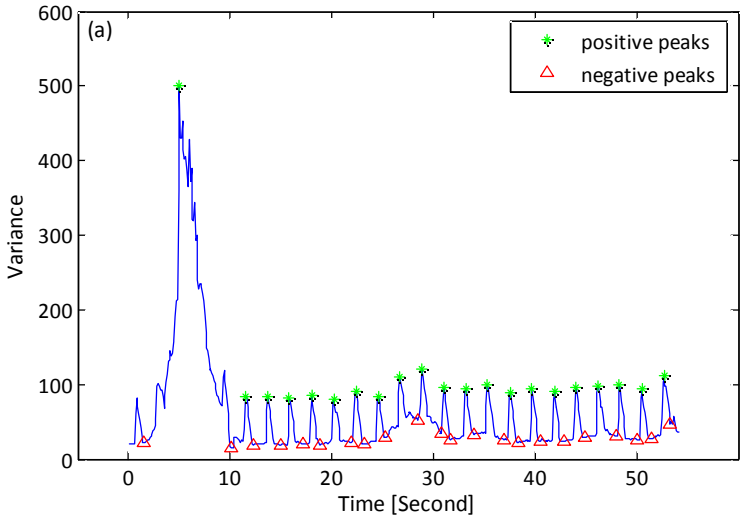

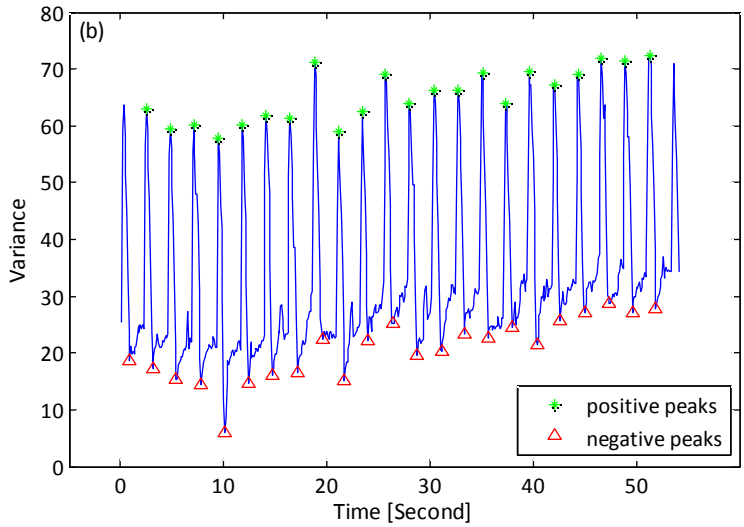

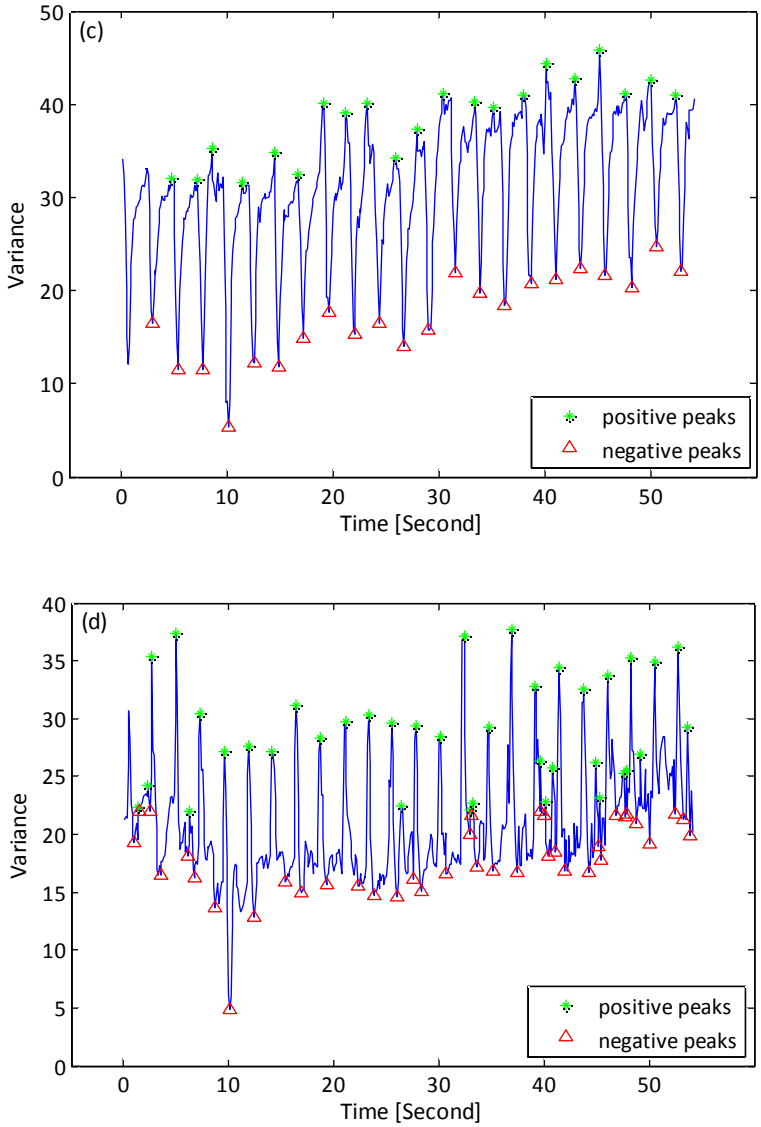

Fig. 31 Detected peaks based on four more cardiomyocyte sequences with the method in the Section 4.3. (a) cardiomyocyte image sequences acquired with difficult conditions. (b), (c), and (d) "noise-free" recordings (i.e. no debris interfering with the measurement) similar to the previous recording.

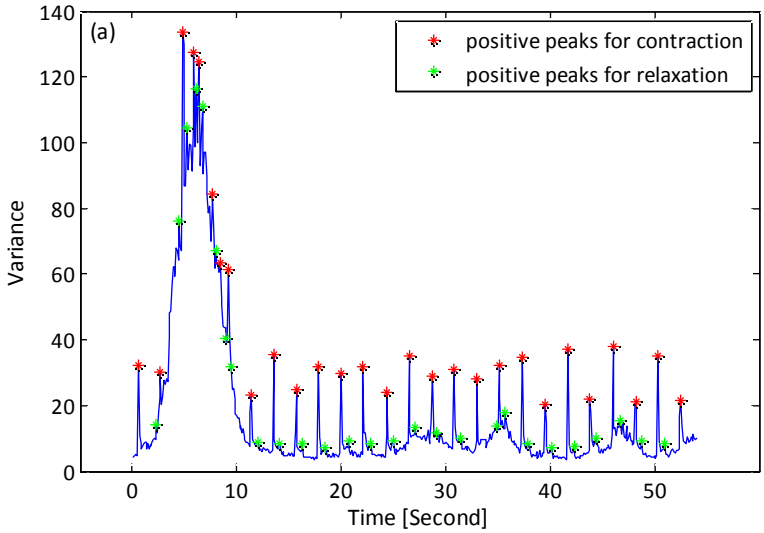

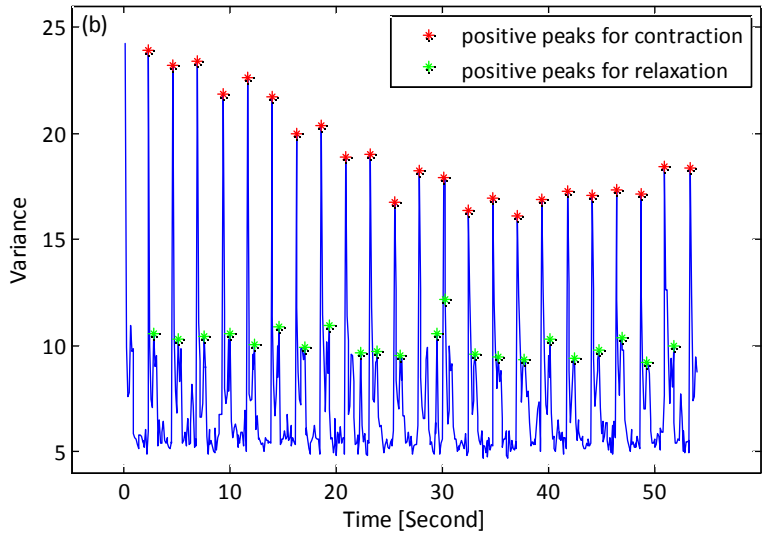

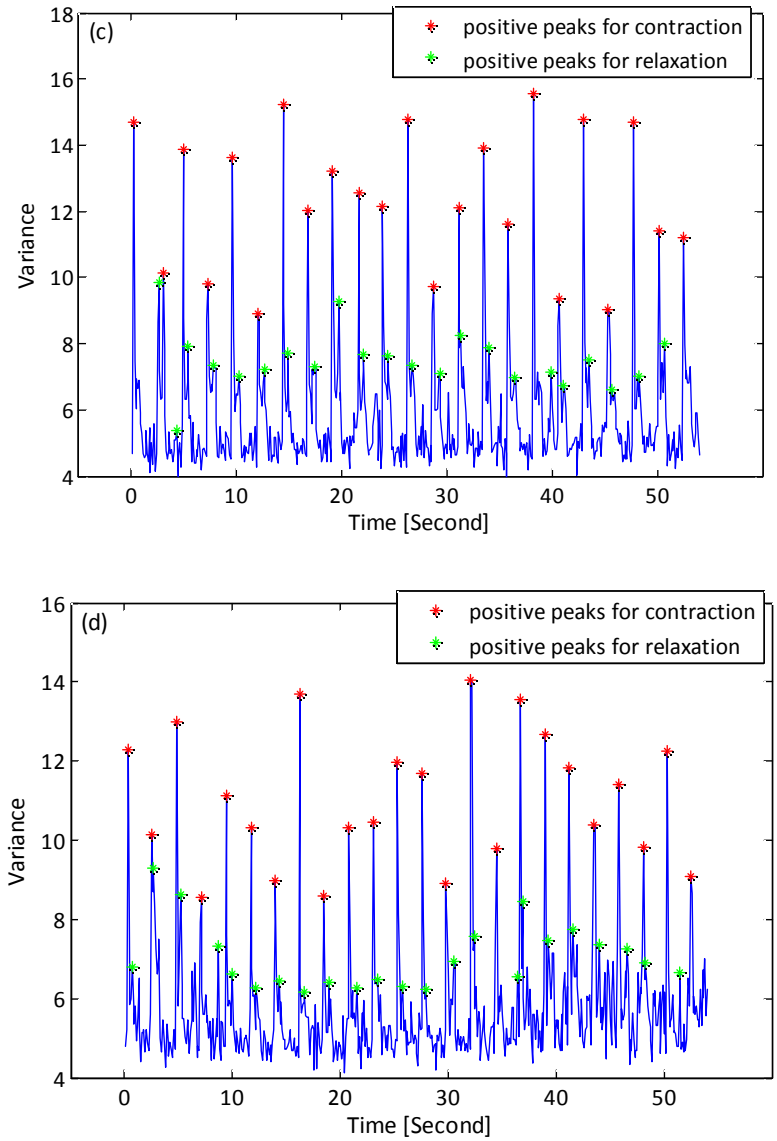

Fig. 32 Detected peaks based on four more cardiomyocyte sequences with the method in the Section 4.4. (a) cardiomyocyte image sequences acquired with difficult conditions. (b), (c), and (d) "noise-free" recordings (i.e. no debris interfering with the measurement) similar to the previous recording

Finally, the mean value of each of the parameter described in the first

(Section 4. 2), second (Section 4. 3) and third (Section 4. 4) methods is measured based on all the five sequences used previously. The measured mean values for the three methods are given in Table 12, Table 13, and Table 14, respectively.

Table. 12 Measured Multiple Parameters on Cardiomyocytes Beating Profile on Five Sequences with the First Method

Multi-parameter	Values (mean/cv)
1: Amplitude:	0.85/1.50
2: Rising time:	0.62/1.37 (seconds)
3: Falling time:	0.85/0.99 (seconds)
4: IBD50:	0.44/0.50 (seconds)
5: IBD10:	2.44/0.45 (seconds)
6: Rising/Falling slope:	0.51/1.52
7: Beating rate:	71.14/0.81
8: Beating period:	0.95/ (sd=0.84 seconds)
9: Frequency	1.16/0.83

Table. 13 Measured Multiple Parameters on Cardiomyocytes Beating Profile on Five Sequences with the Second Method

Multi-parameter	Values (mean/cv)
1: Amplitude:	40.01/1.21
2: Rising time:	0.57/0.86 (seconds)
3: Falling time:	0.43/1.13 (seconds)
4: IBD50:	0.79/0.65 (seconds)
5: IBD10:	2.35/0.38(seconds)
6: Rising/Falling slope:	24.00/1.21
7: Beating rate:	34.48/0.36
8: Beating period:	1.98/(sd=0.83)
9: Frequency	0.55/0.37

Table. 14 Measured Multiple Parameters on Cardiomyocytes Contraction and Relaxation Curve on Five Sequences

Multi-parameters		Values (mean/cv)
Contraction	Beating rate:	31.31/0.17
	Beating period:	2.20/0.19
	Frequency	0.49/0.17
Relaxation	Beating rate:	31.31/0.17
	Beating period:	2.23/0.31
	Frequency	0.49/0.17
Time between contraction and the following relaxation		0.59/0.62

The combined measurements show the robustness of the proposed algorithm and how they allows quantify important cardiomyocyte dynamic parameters that can be used to screen compounds cytotoxic effects. The beating profile contains more information than that is obtained by electrophysiology or fluorescence imaging as it integrates the effect of all the ion-channel involved and thus offer a signature that can be used to predict the effect of specific compounds. For instance inhibitors of hERG channel (the main class of channels assessed in cardio safety, which are involved in repolarization current) all results in a similar profile.In addition, due to the non-invasive aspect of the measurements, both short-term and long-term effects of the monitored compounds can be assessed with DHM.

The suitability of DHM is demonstrated for monitoring and quantifying the beating function of cardiomyocytes and automatically measuring multiple parameters of cardiomyocytes based on the quantitative phase profiles acquired with DHM. The proposed method can be rapid, noninvasive and effective and allows for automated analysis between normal cardiomyocyte dynamics and all other abnormal activities. It is believed that our automated non-invasive measurement procedures can open new perspectives for cardiotoxicological screening or profiling of candidate molecules in preclinical drug discovery and safety testing programs.

5. Conclusions

In this dissertation, a three dimensional imaging technique which is digital holographic microscopy has been applied to visualize human red blood cells and cardiomyocytes. The digital holographic microscopy has advantages of low cost, easy configuration, non-destruction, and fast imaging. Compared with conventional two dimensional imaging approaches, digital holographic microscopy is robust to sense semitransparent or transparent microorganism. The reconstructed image from holograms obtained by digital holographic microscopy with numerical reconstruction algorithm can provide rich three dimensional information such as the optical thickness of biological cells in live and dynamic conditions, which are helpful for the quantitative analysis of three-dimensional cells. Two kinds of transparent cells which are red blood cells and cardiomyocytes are imaged with digital holographic microscopy and the reconstructed images are automatically analyzed. For the analysis of three-dimensional red blood cells, the reconstructed phase images are segmented with marker-controlled watershed transform algorithm and the corresponding red blood cells features are measured. The modifications of three-dimensional morphology and mean hemoglobin of red blood cells induced by the length of storage time are also studied. This analysis is beneficial to the understanding of the features of RBCs with different storage periods and evaluation of any modifications in the 3D cell morphology and hemoglobin content. Moreover, a classifier using Bayesian decision theory for automatic counting of the morphologically normal RBCs of stomatocyte, discocyte, and echinocyte shapes which allows us to quantitatively determine the percentage of normal cell shapes in multiple RBCs has been designed. This proposed method is favorable to the analysis of RBC-related diseases. In addition, it is shown that the discrimination performance for counting of normal shapes of RBCs can be improved by using 3D features of a RBC. For the analysis of 3D

cardiomyocytes, the dynamic beating profile of cardiomyocytes obtained by digital holographic microscopy is investigated using two proposed methods, either by monitoring the average or the variance information of imaged cells. The contraction and relaxation movement are also quantified by analyzing the difference between two successively acquired digital holographic microscopy quantitative phase images. From the experimental results, automated procedures for multiple parameters recording on cardiomyocytes dynamics imaged by digital holographic microscopy for a new methodology in drug toxicity screens is proposed. It is shown, for the first time, that digital holographic microscopy integrated with information processing algorithms can automatically provide dynamic quantitative phase profiles of beating cardiomyocytes. Our study opens the possibility of automated quantitative analysis of red blood cells and cardiomyocyte dynamics suitable for further drug safety testing and compounds selection as a new paradigm in drug toxicity screens.

REFERENCES

[1] K. Onda and F. Arai, "Robotic approach to multi-beam optical tweezers with computer generated hologram," in IEEE Conf. ICRA, 1825-1830, 2011.

[2] I. Moon, M. Daneshpanah, B. Javidi, A. Stern, "Automated three-dimensional identification and tracking of micro/nanobiological organisms by computational holographic microscopy," Proc. IEEE 97(6), 990-1010, 2009.

[3] F. Yi, I. Moon, Y. H. Lee, "Extraction of target specimens from bioholographic images using interactive graph cuts," Journal of biomedical optics, 18(12), 126015-126015,2013.

[4] F. Yi, I. Moon, Y. H. Lee, "Three-dimensional counting of morphologically normal human red blood cells via digital holographic microscopy," Journal of biomedical optics, 20(1), 016005-016005, 2015.

[5] C. Curl, C. J. Bellair, P. J. Harris, B. E. Allman, A. Roberts, K. A. Nugent, L. Delbridge, "Quantitative phase microscopy-a new tool for investigating the structure and function of unstained live cells," Proc. Aust. Physiol. Pharmacol. Soc. 34(12), 896-901, 2004.

[6] D. Fu et al., "Quantitative DIC microscopy using an off-axis self-interference approach," Opt. Lett. 35(14), 2370-2372, 2010.

[7] T. Tishko, Holographic Microscopy of Phase Microscopic Objects: Theory and Practice, World Scientific, Maryland, 2011.

[8] B. Javidi, F. Okano, and J. Sun, 3D Imaging, Visualization, and Display Technologies, Springer, New York, 2008.

[9] W. Osten, T. Baumbach, and W. Juptner, "Comparative digital holography," Opt. Lett. 27, 1764-1766, 2002.

[10] B. Rappaz, E. Cano, T. Colomb, J. Kuhn, C. Depeursinge, V. Simanis, P. J. Magistretti, and P. Marquet, "Noninvasive characterization of the fission yeast cell cycle by monitoring dry mass with digital holographic microscopy," J.

Biomed. Opt. 14(3), 034049-034049, 2009.

[11] Y. Frauel, T. Naughton, O. Matoba, E. Tahajuerce, and B. Javidi, “Three dimensional imaging and display using computational holographic imaging,” Proc. of IEEE 94, 636-654, 2006.

[12] I. Moon et al., “Automated three dimensional identification and tracking of micro/nano biological organisms by computational holographic microscopy,” Proc. IEEE 97, 990-1010, 2009.

[13] B. Javidi, I. Moon, and S. Yeom, “Real-time 3D sensing and identification of microorganisms,” Opt. Photon. News Mag. 17, 16-21, 2006.

[14] J. Goodman and R. Lawrence, “Digital image formation from electronically detected holograms,” Appl. Phys. Lett. 11(3), 77-79 ,1967.

[15] L. Onural and P. Scott, “Digital decoding of in-line holograms,” Opt. Eng. 26(11), 1124-1132, 1987.

[16] U. Schnars, “Direct phase determination in hologram interferometry with use of digitally recorded holograms,” J. Opt. Soc. Am. A 11(7), 2011-2015, 1994.

[17] D. Carl, B. Kemper, G. Wernicke, and G. von Bally, “Parameter-optimized digital holographic microscope for high-resolution living-cell analysis,” Appl. Opt. 43(36), 6536-6544, 2004.

[18] C. Wagner, W. Osten, and S. Seebacher, “Direct shape measurement by digital wavefront reconstruction and multi-wavelength contouring,” Opt. Eng. 39(1), 79-85, 2000.

[19] Y. Zhang, G. Pedrini, W. Osten, and H. J. Tiziani, “Reconstruction of in-line digital holograms from two intensity measurements,” Opt. Lett. 29(15), 1787-1789, 2004.

[20] M. Paturzo, F. Merola, S. Grilli, S. De Nicola, A. Finizio, and P. Ferraro, “Super-resolution in digital holography by a two-dimensional dynamic phase grating,” Opt. Express 16(21), 17107-17118, 2008.

[21] P. Langehanenberg et al., “Autofocusing in digital holographic phase contrast microscopy on pure phase objects for live cell imaging,” Appl. Opt. 47, D176-D182, 2008.

[22] J. Sheng, E. Malkiel, and J. Katz, “Digital holographic microscopy for measuring three-dimensional particle distributions and motions,” Appl. Opt. 45, 3893-3901, 2006.

[23] I. Moon and B. Javidi, “Shape tolerant three-dimensional recognition of biological microorganisms using digital holography,” Opt. Exp. 13, 9612-9622, 2005.

[24] F. Dubois, L. Joannes, and J. C. Legros, “Improved three-dimensional imaging with a digital holography microscope with a source of partial spatial coherence,” Appl. Opt. 38(34), 7085-7094, 1999.

[25] W. Xu, M. H. Jericho, I. A. Meinertzhagen, and H. J. Kreuzer, “Digital in-line holography for biological applications,” Proc. Natl. Acad. Sci. U. S. A. 98(20), 11301-11305, 2001.

[26] E. Cuche, F. Bevilacqua, and C. Depeursinge, “Digital holography for quantitative phase-contrast imaging,” Opt. Lett. 24(5), 291-293, 1999.

[27] E. Cuche, P. Marquet, and C. Depeursinge, “Simultaneous amplitude and quantitative phase contrast microscopy by numerical reconstruction of Fresnel off-axis holograms,” Appl. Opt. 38(34), 6994-7001, 1999.

[28] T. Colomb, E. Cuche, F. Charriere, J. Kuhn, N. Aspert, F. Montfort, P. Marquet, and C. Depeursinge, “Automatic procedure for aberration compensation in digital holographic microscopy and applications to specimen shape compensation,” Appl. Opt. 45(5), 851-863, 2006.

[29] E. Tajahuerce, O. Matoba, and B. Javidi, “Shift-invariant three dimensional object recognition by means of digital holography,” Appl. Opt. 40, 3877-3886, 2001.

[30] D. Abdelsalam, B. Baek, and D. Kim, “Precise test sieves calibration method

based on off-axis digital holography," J. Opt. Soc. Korea 15, 146-151, 2011.

[31] D. Boss et al., "Exploring red blood cell membrane dynamics with digital holographic microscopy," SPIE Photonics Europe, 77153I-77153I, 2010.

[32] E. Cuche, F. Bevilacqua, and C. Depeursinge, "Digital holography for quantitative phase-contrast imaging," Opt. Lett. 24(5), 291-293, 1999.

[33] B. Bhaduri et al., "Optical assay of erythrocyte function in banked blood," Sci. Rep. 4, 6211-6211, 2014.

[34] R. Liu et al.,"Recognition and classification of red blood cells using digital holographic microscopy and data clustering with discriminant analysis," J. Opt. Soc. Am. A 28(6), 1204-1210, 2011.

[35] I. Moon, B. Javidi, F. Yi, D. Boss, P. Marquet, "Automated statistical quantification of three-dimensional morphology and mean corpuscular hemoglobin of multiple red blood cells," Optics express, 20(9), 10295-10309, 2012.

[36] I. Moon, et al. "Automated quantitative analysis of 3D morphology and mean corpuscular hemoglobin in human red blood cells stored in different periods." Optics express 21(25), 30947-30957,2013.

[37] F. Yi, I. Moon, B. Javidi, D. Boss, P. Marquet, "Automated segmentation of multiple red blood cells with digital holographic microscopy," Journal of biomedical optics, 18(2), 026006-026006, 2013.

[38] N. Shaked, L. Satterwhite, and N. Bursac, "Whole-cell-analysis of live cardiomyocytes using wide-field interferometric phase microscopy," Biomedical optics express 1(2) 706-719, 2010.

[39] V. Salnikov, Y. Lukyanenko, W. Lederer, and V. Lukyanenko, "Distribution of ryanodine receptors in rat ventricular myocytes," J. Muscle Res. Cell Motil. 30(3-4), 161-170, 2009.

[40] D. Hickson-Bick, G. Sparagna, L. Buja, and J. McMillin, "Palmitate-induced apoptosis in neonatal cardiomyocytes is not dependent on the generation of ROS," Am. J. Physiol. Heart Circ. Physiol. 282(2), H656-H664, 2002.

[41] E. Azeloglu and K. Costa, “Cross-bridge cycling gives rise to spatiotemporal heterogeneity of dynamic subcellular mechanics in cardiac myocytes probed with atomic force microscopy,” Am. J. Physiol. Heart Circ. Physiol. 298(3), H853-H860, 2010.

[42] A. Kamgoue, J. Ohayon, Y. Usson, L. Riou, and P. Tracqui, “Quantification of cardiomyocyte contraction based on image correlation analysis,” Cytometry A 75(4), 298-308, 2009.

[43] J. Dykens, Y. Will, “The significance of mitochondrial toxicity testing in drug development,” Drug discovery today 12(17), 777-785, 2007.

[44] B. Xi, T. Wang, and N. Li, “Functional cardiotoxicity profiling and screening using the xCELLigence RTCA Cardio System,” Journal of the Association for Laboratory Automation 16(6), 415-421, 2011.

[45] O. Sirenko, C. Crittenden, and N. Callamaras, “Multiparameter in vitro assessment of compound effects on cardiomyocyte physiology using iPSC cells,” Journal of biomolecular screening 18(1), 39-53, 2013.

[46] S. Braam, L. Tertoolen, and A. Stolpe, “Prediction of drug-induced cardiotoxicity using human embryonic stem cell-derived cardiomyocytes,” Stem cell research, 4(2), 107-116, 2010.

[47] M. Jonsson, Q. Wang, and B. Becker, “Impedance-based detection of beating rhythm and proarrhythmic effects of compounds on stem cell-derived cardiomyocytes,” Assay and drug development technologies 9(6), 589-599, 2011.

[48] Y. Abassi, B. Xi, N. Li, W. Ouyang, A. Seiler, M. Watzele, R. Kettenhofen, H. Bohlen, A. Ehlich, E. Kolossov, X. Wang, and X. Xu, “Dynamic monitoring of beating periodicity of stem cell-derived cardiomyocytes as a predictive tool for preclinical safety assessment,” British journal of pharmacology 165(5), 1424-1441, 2012.

[49] C. Carlson, C. Koonce, N. Aoyama, S. Einhorn, S. Fiene, A. Thompson, B. Swanson, B. Anson, and S. Kattman, “Phenotypic screening with human iPS

Cell-Derived Cardiomyocytes HTS-Compatible Assays for Interrogating Cardiac Hypertrophy," Journal of biomolecular screening 18(10), 1203-1211, 2013.

[50] O. Sirenko, E. F. Cromwell, C. Crittenden, J. Wignall, F. Wright, I. Rusyn, "Assessment of beating parameters in human induced pluripotent stem cells enables quantitative in vitro screening for cardiotoxicity," Toxicology and applied pharmacology 273(3), 500-507, 2013.

[51] P. Marquet, B. Rappaz, P. Magistretti, E. Cuche, Y. Emery, T. Colomb, and C. Depeursinge, "Digital holographic microscopy: a noninvasive contrast imaging technique allowing quantitative visualization of living cells with subwavelength axial accuracy," Optics letters 30(5), 468-470, 2005.

[52] B. Rappaz, B. Breton, E. Shaffer, and G. Turcatti, "Digital holographic microscopy: a quantitative label-free microscopy technique for phenotypic screening," Combinatorial chemistry & high throughput screening 14(1), 80-88, 2014.

[53] B. Rappaz, P. Marquet, E. Cuche, Y. Emery, C. Depeursinge, and P. Magistretti, "Measurement of the integral refractive index and dynamic cell morphometry of living cells with digital holographic microscopy," Optics express 13(23), 9361-9373, 2005.

[54] B. Rappaz, E. Cano, T. Colomb, J. Kühn, C. Depeursinge, V. Simanis, P. Magistretti, and P. Marquet, "Noninvasive characterization of the fission yeast cell cycle by monitoring dry mass with digital holographic microscopy," Journal of biomedical optics, 14(3), 034045-034049, 2009.

[55] B. Rappaz, A. Barbul, Y. Emery, R. Korenstein, C. Depeursinge, P. Magistretti, and P. Marquet, "Comparative study of human erythrocytes by digital holographic microscopy, confocal microscopy, and impedance volume analyzer," Cytometry Part A 73(10), 895-903, 2008.

[56] E. Cuche, P. Marquet, and C. Depeursinge, "Simultaneous amplitude and quantitative phase contrast microscopy by numerical reconstruction of Fresnel off-axis holograms," Appl. Opt. 38(34), 6994-7001, 1999.

[57] T. Colomb et al., “Automatic procedure for aberration compensation in digital holographic microscopy and application to specimen shape compensation,” Appl. Opt. 45(5), 851-863, 2006.

[58] F. Yi, I. Moon, “Image segmentation: A survey of graph-cut methods,” In Systems and Informatics (ICSAI), 2012 International Conference on, 1936-1941, IEEE, 2012.

[59] R. C. Gonzalez, R. E. Woods, Digital Imaging Processing; Prentice Hall, New York, NY, USA, 2002

[60] F. Yi, I. Moon, “Automatic calculation of tree diameter from stereoscopic image pairs using digital image processing,” Applied Optics, 51 (18), 4120-4128, 2012.

[61] P. Soille, Morphological image analysis: principles and application; Springer-Verlag, NewYork, 2003.

[62] F. Meyer, “Topographic distance and watershed lines,” Signal process, 38(1), 113-125, 1994.

[63] S. Saraswathi, A. Allirani, “Survey on image segmentation via clustering,” International conference on information communication and embedded systems, 331-335, 2013.

[64] F. Yi, I. Moon, “Extended K-Means Algorithm,” In 5th International Conference on Intelligent Human-Machine Systems and Cybernetics (IHMSC), 2, 263-266, 2013.

[65] W. Tao, H. Jin, Y. Zhang, “Color image segmentation based on mean shift and normalized cuts,” IEEE Trans on systems, man, and cybernetics-part B: cybernetics, 37(5), 1382-1389, 2007.

[66] D. Comaniciu, P. Meer, “Mean shift: A robust approach toward feature space analysis,” IEEE Trans on pattern analysis and machine intelligence, 24(5), 603-619, 2002.

[67] Y. Cheng, “Mean shift, mode seeking, and clustering,” Pattern Analysis and Machine Intelligence, IEEE Transactions on 17(8), 790-799, 1995.

[68] M. Sonka, V. Hlavac, R. Boyle, Image processing, analysis, and machine vision. Thomson, United States, 2008.

[69] M. Kass, A. Witkin, D. Terzopoulos, “Snakes: active contour models,” International journal of computer vision, 1(4), 321-331, 1988.

[70] C. Xu, J. L. Prince, “snakes, shapes, and gradient vector flow,” IEEE Trans on image processing, 7(3), 359-369, 1998.

[71] I. Dagher, K. EI Tom, “Water Balloons: A hybrid watershed Balloon Snake segmentation,” Image and Vision Computing, 26(7), 905-912, 2008.

[72] J. Malek, et al. “Automated breast cancer diagnosis based on GVF-Snake segmentation, wavelet features extraction and fuzzy classification,” Journal of Signal Processing Systems, 55(1-3), 49-66, 2009.

[73] P. Yu, C. L. Poh, “Region-based snake with edge constraint for segmentation of lymph nodes on CT images,” Computers in biology and medicine, 60, 86-91, 2015.

[74] V. Caselles, R. Kimmel, G. Sapiro, “Geodesic active contours,” International journal of computer vision, 22(1), 61-79, 1997.

[75] S. Osher, J. A. Sethian, “Fronts propagating with curveature dependent speed: algorithms based on Hamilton-jacobi formulations,” Journal of computational physics, 79(1), 12-49, 1988.

[76] C. Li, et al. “A level set method for image segmentation in the presence of intensity inhomogeneities with application to MRI,” IEEE Transactions on Image Processing, 20(7), 2007-2016, 2011.

[77] F. P. Van der Meer, N. Moës, and L. J. Sluys, “A level set model for delamination – Modeling crack growth without cohesive zone or stress singularity,” Engineering Fracture Mechanics 79, 191-212, 2012.

[78] K. Zhang, et al. “Reinitialization-free level set evolution via reaction diffusion,” IEEE Transactions on Image Processing, 22(1), 258-27, 2013.

[79] C. Feng, et al. “Segmentation of the left ventricle using distance regularized two-layer level set approach,” Medical Image Computing and Computer-Assisted Intervention-MICCA, Springer Berlin Heidelberg, 477-484, 2013.

[80] Y. Liu, et al. “A novel level set method for segmentation of left and right ventricles from cardiac MR images,” Engineering in Medicine and Biology Society (EMBC) 36th Annual International Conference of the IEEE. 4719-4722, 2014.

[81] K. Zhang, L. Zhang, and M. H. Yang, “Real-time object tracking via online discriminative feature selection,” IEEE Transactions on Image Processing, 22(12), 4664-4677, 2013.

[82] Y. B. Yuri, G. F. Lea, “Graph cuts and efficient N-D image segmentation,” International journal of computer vision, 70(2), 109-131, 2006.

[83] Y. B. Yuri, M. P. Jolly, “Interactive graph cuts for optimal boundary &region segmentation of objects in N-D image,” International conference on computer vision, I, 105-112, 2001.

[84] Y. Boykov, V. Kolmogorov, “An experimental comparison of min-cut/max-flow algorithm for energy minimization in vision,” IEEE Trans on PAMI, 26(9), 1124-1137, 2004

[85] Y. Hou, B. L. Guo, J. S. Pan, “The application and study of graph cuts in motion segmentation,” International conference on IAS, 265-268, 2009.

[86] I. Moon, et al. “Automated quantitative analysis of 3D morphology and mean corpuscular hemoglobin in human red blood cells stored in different periods,” Optics express 21(25), 30947-30957, 2013.

[87] H. G. Davies, M. H. F. Wilkins, J. Chayen, and L. F. La Cour, “The use of the interference microscope to determine dry mass in living cells and as a quantitative cytochemical method,” Quarterly journal of microscopical science 3(31), 271-304, 1954.

[88] T. Tishko, T. Dmitry, and T. Vladimir, Holographic Microscopy of Phase

Microscopic Objects Theory and Practice, World Scientific, 2011.

[89] V. Fairbanks, G. Klee, G. Wiseman, J. Hoyer, A. Tefferi, R. Petitt, and M. Silverstein, "Measurement of blood volume and red cell mass: Re-examination of 51Cr and 125I methods," Blood Cells Foundation 22(2), 169-186, 1996.

[90] B. Rappaz, A. Barbul, Y. Emery, R. Korenstein, C. Depeursinge, P. J. Magistretti, and P. Marquet, "Comparative study of human erythrocytes by digital Holographic microscopy, confocal microscopy, and impedance volume analyzer," Cytometry 73A(10), 895-903, 2008.

[91] D. Boss, J. Kuhn, P. Jourdain, C. Depeursinge, P. J. Magistretti, and P. Marquet, "Measurement of absolute cell volume, osmotic membrane water permeability, and refractive index of transmembrane water and solute flux by digital holographic microscopy," J. Biomed. Opt. 18(3), 036007-036007, 2013.

[92] R. Barer, "Interference microscopy and mass determination," Nature 169(4296), 366-367, 1952.

[93] W. B. Lockwood, R. W. Hudgens, I. O. Szymanski, R. A. Teno, and A. D. Gray, "Effects of rejuvenation and frozen storage on 42-day-old AS-3 RBCs," Transfusion 43(11), 1527-1532, 2003.

[94] "Transfusion handbook, summary information for red blood cells," National Blood Transfusion Committee.

[95] A. Rencher, Methods of Multivariate Analysis, Wiley-Interscience, New York, 2002.

[96] E. Tajahuerce, O. Matoba, and B. Javidi, "Shift-invariant three dimensional object recognition by means of digital holography," Appl. Opt. 40, 3877-3886, 2001.

[97] E. Gose and R. Johnsonbaugh, Pattern Recognition and Image Analysis, Prentice Hall, New Jersey, 1996.

[98] R. Duda, P. Hart, and D. Stork, Pattern Classification, Wiley-Interscience, New York, 2000.

[99] F. Yi, I. Moon, and Y. H. Lee, “Three-dimensional counting of morphologically normal human red blood cells via digital holographic microscopy,” Journal of biomedical optics 20(1), 016005-016005, 2015.

[100] J. Bacus and J. Weens, “Automated method of differential red blood cell classification with application to the diagnosis of anemia,” J. Histochem. Cytochem. 25, 514-632, 1977.

[101] B. Xi, T. Wang, and N. Li, “Functional cardiotoxicity profiling and screening using the xCELLigence RTCA Cardio System,” Journal of the Association for Laboratory Automation 16(6), 415-421, 2011.

[102] W. Moerner and D. Fromm, “Methods of single-molecule fluorescence spectroscopy and microscopy,” Review of Scientific Instruments, 74(8), 3597-3619, 2003.

[103] F. Sadjadi, “Experimental design methodology: The scientific tool for performance evaluation,” Proceedings of SPIE 1310, 100-107, 1990.

ACKNOWLEDGEMENTS

When I finish typing the last character of my doctoral dissertation in the evening, a lot of things appear in my head. I believe the future is wonderful. There were so many meaningful moments I cannot forget and so many people I have to thank.

I am most grateful to my supervisor, Professor Inkyu Moon, for his patient assistance and constant guidance. Without his consistent and illuminating instruction, this dissertation could not have reached its present form. Prof. Moon not only leads me into the world of scientific research but also helps me a lot in life. I clearly remember that Prof. Moon always treated me to dinner after I joined his research group in the year of 2010. In addition, Prof. Moon often helped me buy the air ticket when I went back to China for Chinese New Year. Most importantly, Prof. Moon trusts me very much, which lets me feel free to do any researches. He is also concerned about my future and supports me to do any programs that are beneficial to my future.

I am greatly indebted to my three key mentors in my life. They are 유영철, Kyusung Chung, and Yonghui Xue. It is the encouragement and praise from them that make me from an inferior person to a confident one. They have set a good example for me regarding how to treat others and achieve the value of life. The characteristics of these three mentors have also been my guiding torch in life.

My deepest gratitude goes to my parents, Xuxin Yi and Huoxiu Zhou, who are the greatest persons in my heart. Their unconditional love and support have always been the invariants of my life. Different from my peers' parents in my homeland who only want their children to make money when they become adults, my parents give me enough support to pursue knowledge in school because they believe that knowledge change destiny. I also give my thanks to my old brother and sister who have shared uncountable hours of laughter and joy with me. It is they that take care of my parents when I am out of China. Special thanks are given to my parents-in-law, sister-in-law, and brother-in-law, for their unmatched support and understanding.

I feel grateful to all the professors at Chosun University who once offered me valuable courses and advice during my study. These professors include Prof. Moon Inkyu, Prof. Lee Sangwoong, Prof. Kang Moonsu, Prof. Chung Ilyong, Prof. Cho Beomjoon, Prof. Kim Choongwon, Prof. Moh Sangman, Prof. Shin Yongsuk, and Prof. Kwon Gurak. Especially, I would like to thank Prof. Chung Ilyong for his help before I came to Chosun University. I also wish to thank my colleagues who made my experience a joyful one. These colleagues consist of 정유선, Tabassum Nasrin, Han Minggu, Inbarasan Muniraj, Rao Saifullah, We Jonggob. Senior colleague 정유선 is a very patient person and helps me a lot in terms of preparation of Korean document and adaption of Korean life.

My gratitude also extends to my friends who I always play together with in Korea, especially, my friends Hongzhuo Qian and Huan Xu. It is they who let me know Korea better and make my spare time rich and colorful. I will never forget the happy time we spent together in Korea. I also want to express my thanks to my other two friends Zeming Zhao and Zuoming Zhou who always let me feel pleased and stress-free. It is indeed my honor to have these wonderful friends.

Last my thanks would go to my beautiful and charming wife Xinfeng Feng who has supported me a lot for every choice I made. If we say there is a great woman behind every man who has got his doctoral degree, this great woman is definitely my wife in my case. It is she who shares with me every happy moment. It is also she who enhances my happiness. She agreed to marry with me at the time when I have nothing. Undoubtedly, I will appreciate my wife forever.

In brief, I deeply appreciate all of the professors, relatives, colleagues, and friends who have helped me a lot. I sincerely wish them all the best in their lives.

致謝

当在寂静的夜晚敲完博士論文的最后一个字符時，我思緒万千。這一路的歷程就如電影般精彩絶倫，我不是導演，但确是主角。太多的事値得回憶，太多的人値得感謝。相信這所經歷的一切都預示了未來的美好。我也确信，未來必定美好。

忘記不了影響我一生，給我指引前進道路的三位老師，兪榮哲，丁奎盛，薛永輝。是他們的教導，鼓勵与贊美讓我樹立起了自信，感触到人生的美好。他們的話使我倍感親切并充滿无窮的力量。非常感謝他們。

感謝在我來韓國之前，是丁教授 (Prof. Chung Ilyong) 提前帮我聯系好了導師和奬學金。沒有丁教授的帮助，我不會認識在碩博階段一直指導着我的文教授（Prof. Moon Inkyu). 文教授不僅在學術上指導我，讓我知道怎么去思考，研究，寫作論文。在生活上，文教授也給与了我极大大的帮助。清楚的記得，当我在第一年還沒适應韓國的飲食習慣時，是文教授經常帶着我去吃我比較喜歡的飲食（主要是不用我買單）。每次回國，文教授都給我路費，讓我倍感溫馨。最重要的是，文教授對我十分的信任，使我能放開的去做研究，去處理身邊的事情。同時，教授也十分關心我的未來，只要對我有益的事，教授都給予全力的支持。在此，把我最誠摯的謝獻給我尊敬的文教授。

我也非常感謝我的爸爸，媽媽。爸爸媽媽是我心中最偉大的人，也是我永遠的榜樣。是他們靠着自己勤勞的双手讓我順利念完大學。不同農村很多其他父母希望孩子們早点出來掙錢，我爸爸媽媽一直非常支持我求學的道路，因爲他們相信，知識能改變命運。即使自己再苦再累，也始終无怨无悔。在讀博的歲月里，爸媽的双鬢也慢慢變白了，作爲儿子，實在感覺亏欠他們太多。然而，爸媽還是一如既往的支持着我一切的選擇。謝謝爸爸媽媽。同時也感謝我的哥哥姐姐。是他們給了我童年的歡樂，是他們在我遠离家鄉時照顧着爸媽，讓我能安心求學。因爲哥哥姐姐，我們的家庭才始終充滿了溫暖。同樣，也感謝我的嫂子和姐夫，家庭的溫馨离不開她們的支持。

其次，衷心的感謝教過我課程的老師們。他們是：Prof. Moon Inkyu, Prof. Lee Sangwoong, Prof. Kang Moonsu，Prof. Chung, Ilyong, Prof. Cho Beomjoon, Prof. Kim Choongwon, Prof. Moh Sangman, Prof. Shin Yongsuk, and Prof. Kwon Gurak. 是他們讓我獲取到更多更全面的知識。也感謝和我一个實驗室的同僚們。他們是정유선，Tabassum Nasrin, Han Minggu, Inbarasan Muniraj, Rao Saifullah, We Jonggob. 是她們讓實驗室充滿有活力，使我有个和諧的辦公环境。特別感謝정유선學姐，每次有材料信息需要處理時，都能得到她熱心的帮忙。對我的帮助，정유선學姐非常有耐心，而且會帮到底。非常感謝有這么一位前輩。

同樣感謝在韓國經常一起玩的小伙伴們。感謝月光的朋友們，特別是錢紅卓和徐歡。是紅卓和徐歡讓我更多的了解韓國，他們讓我的業余生活更加多彩。忘不了我們在韓國一起旅游的日子。也謝謝我倆个叫胖子的好朋友，趙則名和周佐明。有煩惱壓力時，來自他們的哪怕一个扣鼻屎的QQ圖，都能讓我壓力大減。

最后，非常感謝我漂亮的妻子，馮新鳳。從我們相識開始，她就一直支持着我所做出的任何一个選擇。如果說每个完成博士學位的男人背后都有一个支持他的女人的話，那對于我，這个女人就是我的妻子。是她，讓我沒有后顧之憂，是她，讓我有更强的幸福感，也是她陪我度過每个困難的時刻，分享每个歡樂的時光。在我一无所有的時候，她愿意成爲我的妻子，使我万分感動，我將永遠銘記在心。

總之，在博士論文完成之際，謹以此文獻給所有帮助過我的親人，老師，同學和朋友們。也衷心祝福他們，愿他們一生幸福！